Atmospheric properties and dynamics of gaseous exoplanets inferred from high-resolution alkali line transmission spectroscopy

---

Engin Keles

Leibniz-Institut für Astrophysik Potsdam

Univ.-Diss.

Kumulative Dissertation zur Erlangung des akademischen Grades "doctor rerum naturalium" (Dr. rer. nat.) in der Wissenschaftsdisziplin

Physik

eingereicht an der

Mathematisch-Naturwissenschaftlichen Fakultät der

Universität Potsdam

und

Leibniz-Institut für Astrophysik Potsdam (AIP)

Potsdam den 21.01.2021

Hauptbetreuer:	Zweitbetreuer:	Mentor:	Gutachter:
Prof. Dr. Klaus G. Strassmeier	Prof. Dr. Frank Spahn	Dr. Matthias Mallonn	Prof. Dr. Klaus G. Strassmeier Dr. habil. Antonio Garcia Munoz Prof. Dr. Ignasi Ribas

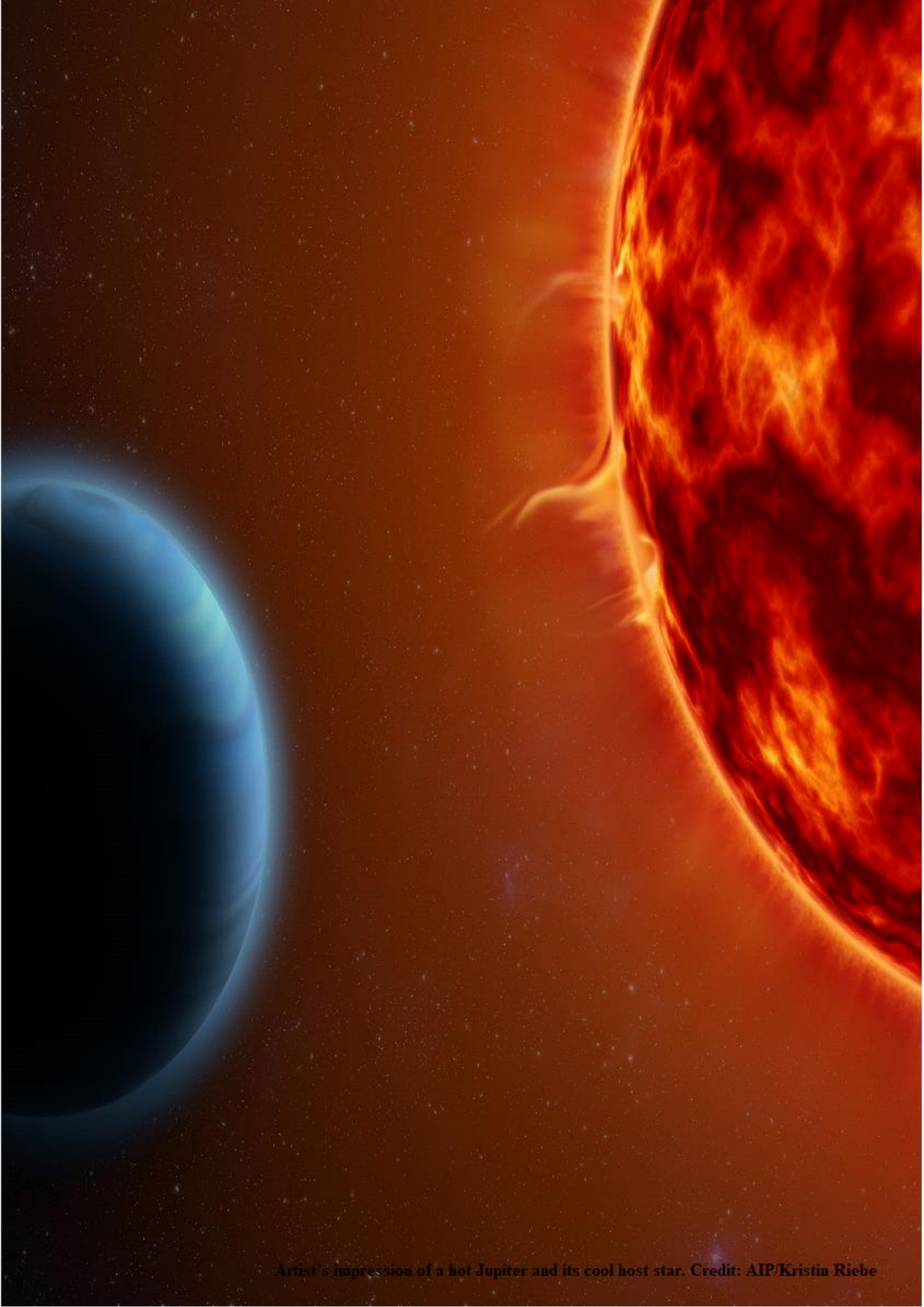

Artist's impression of a hot Jupiter and its cool host star. Credit: AIP/Kristin Riebe

Contents

List of Figures v

List of Tables ix

Zusammenfassung 1

Summary 3

1 Introduction 5
- 1.1 Hot and ultra-hot Jupiter type exoplanets . . . 5
- 1.2 Exoplanet detection and characterization methods . . . 6
  - 1.2.1 Detection of exoplanets: The Transit and RV- method . . . 6
  - 1.2.2 Characterization of exoplanets: Transits, eclipses and phase curves . 7
- 1.3 Fingerprints of exoplanet atmospheres in transmission spectra . . . 8
  - 1.3.1 Atmospheric opacities: Clouds and hazes . . . 8
  - 1.3.2 Atmospheric opacities: Atoms and molecules . . . 10
- 1.4 Revealing exoplanet atmospheres . . . 10
- 1.5 This work: Science question and investigation . . . 11
  - 1.5.1 The Science question . . . 11
  - 1.5.2 The Investigations . . . 11
  - 1.5.3 Bottom line . . . 12

2 Signature in high-resolution exoplanet observations: approaches and caveats 14
- 2.1 The "excess method" and the effect of the stellar center-to-limb variation . 14
- 2.2 The "division method" and the residual RM- effect . . . 15
- 2.3 The "cross-correlation method" . . . 16

3 Overview of the Manuscripts 18
- 3.1 Manuscript I: "The potassium absorption on HD189733 and HD209458b", Monthly Notices of the Royal Astronomical Society: Letters, Volume 489, Issue 1, Pages L37–L41, October 2019 . . . 18
- 3.2 Manuscript II: "Probing the atmosphere of HD189733b with the Nai and Ki lines", Monthly Notices of the Royal Astronomical Society, Volume 498, Issue 1, Pages 1023–1033, October 2020 . . . 19
- 3.3 Manuscript III: "Spectral signature of atmospheric winds in high resolution transit observations", Monthly Notices of the Royal Astronomical Society, accepted 2021 January 11 . . . 19

4 The potassium absorption on HD189733b and HD209458b 20
- 4.1 Abstract . . . 20
- 4.2 Introduction . . . 20
- 4.3 Observations . . . 21
- 4.4 Data Analysis . . . 21
  - 4.4.1 Telluric lines . . . 22
  - 4.4.2 Excess absorption . . . 22

4.4.3 Center-to-limb variation . . . 23
4.5 Results . . . 24
4.5.1 Investigating potassium on HD189733b . . . 24
4.5.2 Stellar activity of HD189733 . . . 25
4.5.3 Investigating potassium on HD209458b . . . 25
4.6 Discussion . . . 26

5 Probing the atmosphere of HD189733b with the Nai and Ki lines 28
5.1 Abstract . . . 28
5.2 Introduction . . . 28
5.3 Observational data . . . 30
5.3.1 The Ki Observation . . . 30
5.3.2 Nai detection by Casasayas-Barris et al. (2017) . . . 30
5.4 Models . . . 30
5.4.1 The residual RM-feature . . . 30
5.4.2 The rotational broadening model . . . 31
5.4.3 The Synthetic Transmission spectra . . . 31
5.5 Method and Results . . . 32
5.5.1 Re-investigating the Ki-absorption on HD189733b . . . 32
5.5.2 Comparison of the synthetic- and observational Ki-line profile . . . 35
5.5.3 Comparison of the synthetic- and observational Nai-D-lines . . . 36
5.6 Discussion . . . 38
5.7 Summary & Conclusion . . . 42
5.8 Appendix . . . 42
5.8.1 Synthetic Transmission spectra . . . 42
5.8.2 Cautions on the estimated planetary Na/K abundance ratio . . . 43
5.8.3 The stellar Na and K abundance ratio . . . 44

6 Spectral signature of atmospheric winds in high resolution transit observations 46
6.1 Abstract . . . 46
6.2 Introduction . . . 46
6.3 Model . . . 48
6.4 Method . . . 49
6.5 Results . . . 51
6.5.1 Rotational broadening of weaker and stronger Nai- lines in an extended and unextended atmosphere . . . 51
6.5.2 Effect of an eastward streaming zonal jet reaching latitudes of ±20° and ±40° on the Nai- absorption line . . . 52
6.5.3 Effect of an eastward streaming zonal jet with different velocities on the trailing and leading limb reaching latitudes of ±20° and ±40° on the Nai- absorption line . . . 54
6.5.4 Effect of an eastward streaming zonal jet reaching latitudes of ±20° with additional westward streaming jets at the poles on the Nai-absorption line . . . 56
6.5.5 Time dependent line profile variation during ingress and egress . . . 57
6.6 Discussion . . . 59
6.6.1 Detectability of atmospheric wind pattern . . . 59
6.6.2 Investigating the resolved Nai-D2 lines on different exoplanets . . . 60
6.6.3 Caveats . . . 63
6.7 Summary . . . 64
6.8 Appendix . . . 66

7 Discussion **68**
7.1 Investigating exoplanets with the alkali lines: The Potassium Detection . . 68
7.2 Tracing atmospheric chemistry and properties with the alkali lines 69
7.3 Tracing atmospheric dynamics with the alkali lines 70
7.4 Closing words 71

Bibliography **72**

Acknowledgment **83**

Eidesstattliche Erklärung **85**

List of Figures

1.1 Detection and properties of exoplanets: (I) shows an orbiting exoplanet around its host star. The dashed lines illustrate the transit (blue box) and eclipse (red box). (II) shows the change in flux over the different orbital phases, where the solid lines refer to the transit (blue) and eclipse (red) (Winn, 2008). (III) shows the barycentric motion of star and planet around their center of mass which results in blue- and red-shift of stellar spectral lines. (IV) shows the theoretically expected absorption and emission of carbon monoxide from an exoplanet atmosphere which is Doppler-shifted regarding the different orbital phases (Snellen et al., 2010a). (I)-(IV) are updated for illustration purposes. 7

1.2 Different low-resolution transmission spectra from the optical to the near-infrared wavelength range of gaseous exoplanets together with synthetic spectra (solid) shown by Sing et al. (2016). The y axis shows the relative altitude in scale heights for better visibility. 9

2.1 Illustration of the CLV-effect: The stellar spectral lines arising from different surface regions are demonstrated top left (sodium) and top right (potassium). "clvline" and "clvcont" shows the transit lightcurve in the line core and continuum, respectively. The division of both results in the CLV-effect (lower left and right), which show emission- and absorption like feature in "excess absorption curves". The amplitude of the feature decreases for larger integration bandwidths (see legend). 15

2.2 Illustration of the residual RM-effect for the transit of HD189733b. Left panel: The planet transits (orange dot) from left to right and blocks different Doppler-shifted light arising from the stellar surface (colour-coding shows the velocity in km/s). Right panel: Dividing the stellar spectra inferred during transit and out-of-transit leads to a residual feature within the transmission spectra. 17

4.1 Full PEPSI spectra (top) and Ki lines (bottom). Dashed lines mark the Ki lines (red) and control lines (colored) and the solid blue line mark the telluric model for few telluric lines. Shaded area shows the planetary motion of around ±0.42Å during the transit. 22

4.2 K excess absorption (EA) for HD189733b (left) and HD209458b (right). EA curves at 0.8 Å bandwidth (BW) using reference bands (top) and no reference bands (middle). Bottom panel shows the EA level for different BW. Green line shows the CLV-curve and the blue line the planetary absorption (both mirrored to mimic the second half of the transit for HD209458b). Tables show EA up to 8Å. 24

4.3 Mean excess absorption for several control lines compared to Ki (red square) at 0.8 Å bandwidth for HD189733b. 25

5.1 Transmission spectra around the Ki-line at 7698.98 Å (orbital phase vs. velocity shift). Left panel: The observations divided by the Master out spectrum and subtracted by unity (red). Middle panel: The residual RM-model and the fit to the emission line induced by stellar activity. Right: The residual spectrum (left panel divided by the middle panel) showing the Ki absorption (dark region). Green dashed lines mark the 1st and 4rd contact and the yellow lines the 2nd and 3rd contact. 32
5.2 Excess absorption around a 0.5 Å bandwidth centered around the Ki-line at 7699 Å (first panel), the Caii- line at 8662 Å (second panel) and the control Cri-line at 7462 Å (third panel). 33
5.3 Transmission spectrum around the Ki-line at 7699 Å in [%] subtracted from unity. The black solid line shows the Gaussian fit. The dashed lines show the expected planetary absorption from the synthetic spectra without any broadening (red) and with the best-matching broadening solution of 3.8 km/s (green). The residual spectrum is shifted for clarity. 34
5.4 Shown is the abundance-temperature degeneracy for Ki-line. log K denotes the logarithmic volume mixing ratio of K. Reduced χ^2 values (color marked) relative to the best value compare the observational Ki-line with various synthetic line profiles. Each pixel corresponds to one comparison. 35
5.5 Top panel: Abundance-temperature degeneracy for Nai-D-lines, where log NaD2 and log NaD1 are the logarithmic volume mixing ratios. Reduced χ^2 values relative to the best value (color marked) compare the observational Nai-D-profiles with various synthetic spectra, whereby each pixel corresponds to one spectrum comparison. Middle panel: The introduced broadening to the synthetic spectra is shown. The color bar indicates the broadening value in km/s. Bottom panel: The line contrast over line center distance in units of velocity is shown for theNai-D2-line (left) and Nai-D1-line (right). The synthetic mean line profile with (dashed black) and without (dashed blue) introduced broadening. Red dots show the resolved planetary Nai-D-lines from Casasayas-Barris et al. (2017) (binned by 10 pixels) and grey show their unbinned data. 37
5.6 Top panel: Comparison of the mean synthetic Nai-D-lines and the Ki-line from this work. Dashed lines show line profiles before and solid lines after introduced rotational broadening. Bottom panel: Nai-D-lines and Ki-line modelled for isothermal temperature and solar abundance value at 2000K (blue), 4000K (red) and 6000K (yellow) for turbulence velocities of v_t of 1 km/s (solid), 10 km/s (dashed) and 20 km/s (dotted). The x-axis shows the distance to the line center in km/s. 39
5.7 Comparison of Na-line at 8195 Å (top) and the 7699 Å Ki-line (bottom) from PEPSI spectra with the spectrum synthesis model based on a standard 1D model atmosphere. "A" denotes the logarithmic abundance value. . . . 45

6.1 Effect of rotational broadening on absorption lines. Left panel: Illustration of an absorbing circle from the transparent region of a Jupiter type planet with a planetary rotation of ± 6 km/s. Middle panel: Dashed lines show absorption lines that are shifted in velocity with the colour coding illustrating the different regions from the atmospheric circle. The black solid line shows the final line profile which is the sum of all velocity shifted contributions. Note, that there is an overdensity of line profiles around the line core region of the black solid line which are not shown for better visibility of the illustration. Right panel: Yellow solid line shows the line profile before broadening and the black solid line after the broadening. The dashed lines show the broadening if one accounts for the full surface i.e. similar to a stellar surface and compares this work (magenta) to the PyAstronomy tool *pyasl.fastRotBroad* (green). 49

6.2 The effect of rotational broadening on a stronger (magenta) and weaker (purple) Nai absorption line before (dashed) and after (solid) broadening. The Nai-D2 line from Keles et al. (2020) is scaled for this purpose. The translucent atmospheric circle is set to ($R_{pl} < R_{Atmo} < 1.1 \times R_{pl}$) (first line) and ($R_{pl} < R_{Atmo} < 1.5 \times R_{pl}$) (second line). The second column shows a Jupiter type planet with $V_{rot} = 3$ km/s and the third with $V_{rot} = 6$ km/s. The first column illustrates the science cases. The third row shows the difference between the broadened line profiles from the panels above and the forth column shows the difference between the broadened line profile from the different rotating planets (each for the same line strength). Each column shares the x-axis and the second and third column share the same y-axis. 51

6.3 The effect of an eastward streaming jet with $V_{Jet} = \mp 6$ km/s $\times \sin\theta$ reaching latitudes of ±20° (first row) and ±40° (second row) on Nai-absorption lines (solid) on a planet with $V_{rot} = 3$ km/s (second column) and $V_{rot} = 6$ km/s (third column). The dashed lines consider only the planetary rotation for comparison. The atmospheric extension is fixed to ($R_{pl} < R_{Atmo} < 1.3 \times R_{pl}$). The first column illustrates the science cases. The fourth column show the difference between the broadened and unbroadened line profiles and the third row show the difference for the broadened line profiles with different jet streams. The label shows the 3σ spectral mean S/N value with $\Phi_{HD189733b} \approx 0.066$. Each column shares the x-axis and the second and third column share the same y-axis. 53

6.4 The effect of an eastward streaming jet with with $V_{JET} = \mp 6$ km/s and line of sight velocity of $V_{E\text{-}LOS} = (V_{rot} + V_{JET}) \times \sin\theta$ on the eastern hemisphere and $V_{W\text{-}LOS} = 0.33 \times (V_{rot} + V_{JET}) \times \sin\theta$ on the western hemisphere reaching latitudes of ±20° (first row) and ±40° (second row) on Nai-absorption lines (solid) on a planet with $V_{rot} = 3$ km/s (second column) and $V_{rot} = 6$ km/s (third column). The dashed lines consider only the planetary rotation for comparison. The atmospheric extension is fixed to ($R_{pl} < R_{Atmo} < 1.3 \times R_{pl}$). The first column illustrates the science cases. The fourth column show the difference between the broadened and unbroadened line profiles and the third row show the difference for the broadened line profiles with different jet streams. The label shows the 3σ spectral mean S/N value with $\Phi_{HD189733b} \approx 0.066$. Each column shares the x-axis and the second and third column share the y-axis. 55

6.5 The effect of an eastward streaming jet with $V_{Jet} = \mp$ 6 km/s reaching latitudes of $\pm 20^{\circ}$ and two westward streaming jets at the poles with $V_{WJET} = \pm 2$ km/s (first row) and $V_{WJET} = \pm 6$ km/s (second row) on Nai-absorption lines (solid) on a planet with $V_{rot} = 3$ km/s (second column) and $V_{rot} = 6$ km/s (third column). The dashed lines consider only the planetary rotation for comparison. The atmospheric extension is fixed to ($R_{pl} < R_{Atmo} < 1.3 \times R_{pl}$). The first column illustrates the science cases for the faster rotating planet. The fourth column show the difference between the broadened and unbroadened line profiles and the third row show the difference for the broadened line profiles with different westward streaming jet velocities. The label shows the 3σ spectral mean S/N value with $\Phi_{HD189733b} \approx 0.066$. Each column shares the x-axis and the second and third column share the same y-axis. 57

6.6 Time dependent line profiles for different snapshots during ingress and egress for a Jupiter type planet with $V_{rot} = 3$ km/s. Column 1, 2 and 3 show the same scenarios as presented in Section 6.5.2, Section 6.5.3 and Section 6.5.4, respectively. The dashed lines consider only the planetary rotation for comparison. The fourth column shows the different snap shots during ingress and egress, whereas the black shaded region illustrates the illuminated atmospheric region. The label shows the 3σ spectral mean S/N value with $\Phi_{HD189733b} \approx 0.279$. Each column shares the x-axis and the panel with the line profiles share the y-axis. 58

6.7 Inferred broadening values for the Nai-D2 lines detected on different exoplanets presented in Table 6.1. The y-axis shows the excess velocity i.e. $V_{Jet} = V_{bro}$ - V_{rot}. 62

6.8 Shown are the best matching line profiles between the observational (see also Table 6.1 for comparison) Gaussian line profiles (black solid) and the broadened line profiles inferred from the equivalent width comparison (blue dashed). The dashed yellow line shows the unbroadened line profile. The different columns share the x-axis. 66

List of Tables

6.1 Na-D2 line properties found for different exoplanets. 61

Zusammenfassung

Die Charakterisierung von Exoplaneten durch hoch-aufgelöste Transmissionsspektroskopie hat eine neue Ära eingeleitet, um Atome und Moleküle in hohen atmosphärischen Schichten zu untersuchen, welches uns Hilft die Entwicklung unseres Sonnensystems besser zu verstehen. In anderen Sternensystemen wurden Jupiter ähnliche Planeten gefunden, die ihren Mutterstern innerhalb weniger Tage umkreisen, sogenannte heiße- und ultra-heiße Jupiter. Die Bekanntesten sind HD209458b und HD189733b, welche auch die ersten Exoplaneten sind, bei denen atmosphärische Absorption detektiert wurde, und zwar von dem Alkali Element Natrium. Resonante Alkali Absorptionslinien sind in heißen Jupiter Atmosphären sehr prägnant aufgrund des hohen Absorptions-Wirkungsquerschnitts. Obwohl niedrig-aufgelöste Spektrographen bereits in den Atmosphären von verschiedenen heißen Jupitern die Alkali Elemente Natrium und Kalium nachgewiesen haben, wurde nur Natrium mit hoch-auflösenden Spektrographen gefunden; im Gegensatz zu Kalium. Dies war verwunderlich, da beide Elemente sehr ähnliche physikalische und chemische Eigenschaften besitzen, z.B. in Bezug auf Ausdünstung und Ionisierung.
Durch Beobachtungen des Transits von HD189733b und HD209458b mit einem hoch-auflösenden Spektrographen, konnten wir Kalium auf HD189733b nachweisen (Ausarbeitung I), welches die erste hoch-aufgelöste Detektion von Kalium in einer Planetenatmosphäre ist. Die Abwesenheit von Kalium auf HD209458b könnte durch Abbauprozesse wie Ausdünstung oder Ionisierung erklärt werden oder aber auch durch Wolken in sehr dünnen atmosphärischen Schichten, welche dessen Absorptionsprofile verbergen.
In einer zweiten Studie (Ausarbeitung II), konnten wir die Kalium Linie aus den Spektren auflösen und mit Natrium, welches in einer anderen Studie für HD189733b gefunden wurde, vergleichen. Dies zeigte, dass entweder Kalium in anderen Höhen und Temperaturen als Natrium existiert, oder dass Kalium in der Atmosphäre abgebaut sein muss, so dass das planetare Natrium - Kalium - Verhältnis viel größer ist als das des Muttersterns. Der Vergleich der Alkali Linien mit synthetischen Profilen zeigte, dass die Natrium Linien viel stärker verbreitert sind als die Kalium Linien, wobei Winde als mögliche Ursache gelten.
In einer dritten Studie wurde der Effekt von zonalen Winden auf heißen Jupitern auf die Natrium Linie untersucht (Ausarbeitung III). Es wurde nachgewiesen, dass solche Winde die Natrium Linien signifikant verbreitern können. Weiterhin zeigte die Untersuchung von Natrium Absorptionslinien, die auf diversen Planeten gefunden worden sind, dass die Linienverbreiterung einem Muster folgt. Auf kühleren Planeten ist die Verbreiterung der Linien stärker als auf heißeren Planeten, was darauf deutet, dass die Winde hier stärker sein müssen.
Die drei Teilstudien stellen einen Zusammenhang dar, so dass eine in sich geschlosssene Arbeit für die Untersuchung des Planeten HD189733b entstand. Die Untersuchung der Kalium Absorption mit diversen Methoden machte es notwendig, verschiedene Effekte zu berücksichtigen, z.B. die Entfernung von tellurischen Linien und Beachtung des CLV-Effektes (Ausarbeitung 1), die Modellierung des Rossiter- McLaughlin- Effektes (Ausarbeitung 2) und die Entwicklung eines Wind Modells (Ausarbeitung 3). Diese Arbeit zeigt, dass hoch-aufgelöste Transmissionsspektroskopie sehr wirkungsvoll ist, um dünne Absorptionslinien von Alkali Atomen auf heißen Jupitern zu beobachten und die Eigenschaften und Dynamik von Atmosphären heißer Jupiter Planeten zu untersuchen.

Summary

The characterization of exoplanets applying high-resolution transmission spectroscopy initiated a new era making it possible to trace atmospheric signature at high altitudes in exoplanet atmospheres and to determine atmospheric properties which enrich our understanding of the formation and evolution of the solar system.
In contrast to what is observed in our solar system, where gaseous planets orbit at wide orbits, Jupiter type exoplanets were detected in foreign stellar systems surrounding their host stars within few days, in close orbits, the so called hot- and ultra-hot Jupiters. The most well studied ones are HD209458b and HD189733b, which are the first exoplanets where absorption is detected in their atmospheres, namely from the alkali line sodium. For hot Jupiters, the resonant alkali lines are the atmospheric species with one of the strongest absorption signatures, due to their large absorption cross-section. However, although the alkali lines sodium and potassium were detected in low-resolution observations for various giant exoplanets, potassium was absent in different high-resolution investigations in contrast to sodium. The reason for this is quite puzzling, since both alkalis have very similar physical and chemical properties (e.g. condensation and ionization properties).
Obtaining high-resolution transit observations of HD189733b and HD209458b, we were able to detect potassium on HD189733b (Manuscript 1), which was the first high-resolution detection of potassium on an exoplanet. The absence of potassium on HD209458b could be reasoned by depletion processes, such as condensation or photo-ionization or high-altitude clouds. In a further study (Manuscript II), we resolved the potassium line and compared this to a previously detected sodium absorption on this planet. The comparison showed, that the potassium lines are either tracing different altitudes and temperatures compared to the sodium lines, or are depleted so that the planetary Na/K- ratio is way larger than the stellar one. A comparison of the alkali lines with synthetic line profiles showed that the sodium lines were much broader than the potassium lines, probably being induced by winds. To investigate this, the effect of zonal streaming winds on the sodium lines on Jupiter-type planets is investigated in a further study (Manuscript III), showing that such winds can significantly broaden the Na- lines and that high-resolution observations can trace such winds with different properties. Furthermore, investigating the Na-line observations for different exoplanets, I showed that the Na-line broadening follows a trend with cooler planets showing stronger line broadening and so hinting on stronger winds, matching well into theoretical predictions. Each presented manuscript depends on the results published within the previous manuscript, yielding a unitary study of the exoplanet HD189733b.
The investigation of the potassium absorption required to account for different effects: The telluric lines removal and the effect of center-to-limb variation (see Manuscript I), the residual Rossiter-Mc-Laughlin effect (see Manuscript II) and the broadening of spectral lines on a translucent atmospheric ring by zonal jet streams (see Manuscript III).
This thesis shows that high-resolution transmission spectroscopy is a powerful tool to probe sharp alkali line absorption on giant exoplanet atmospheres and to investigate on the properties and dynamics of hot Jupiter type atmospheres.

1 Introduction

Exoplanets – the science about planets orbiting foreign stars in other stellar systems which fascinates astronomers since ancient times and a research field becoming intensively studied since the discovery of the first exoplanet 51 Peg b in 1995 (Mayor & Queloz, 1995). To date, the number of confirmed[1] exoplanets is >4300 and increasing. The majority of planets to date is discovered by space missions such as the Kepler mission (Borucki et al., 2010) launched 2009. Another very promising space mission for the hunt for exoplanets is the Transiting Exoplanet Survey Satellite (TESS) mission (Ricker et al., 2015) launched 2018. But not only space missions are suitable to detect exoplanets. Although ground-based observations have several disadvantages such as day-night-cycles, cloud coverage, or telluric contamination, also the ground-based search showed large success in finding especially giant exoplanets such as the Kilodegree Extremely Little Telescope (KELT) (Pepper et al., 2007) survey or the Wide Angle Search for Planets (WASP) (Pollacco et al., 2006) survey. With future prospects, the Holy Grail is the investigating of terrestrial exoplanets around nearby stars (Ribas et al., 2018) and especially the atmospheres of planets in habitable zones (i.e. the place around the star where liquid water may exist), especially to date where 60 habitable[2] zone planets are known. Especially the investigation of the non-transitting Earth-sized planet around the nearest star Proxima Centauri or the seven transiting Earth-size planets around TRAPPIST-1 at a distance of ∼12 pc will be of special interest (Birkby, 2018). This perspective seems to be reachable soon with the launch of the James Webb Space Telescope (JWST) (Deming et al., 2009), but also first attempts were made with ground-based facilities to study the atmosphere of smaller exoplanets in the size of Super-Earths (Ridden-Harper et al., 2016; Esteves et al., 2017).

1.1 Hot and ultra-hot Jupiter type exoplanets

Although the investigation of habitable-zone planets is the key perspective, such kinds of planets are difficult to investigate due to their tiny atmospheres. But another class of exoplanets emerged in the last decades enabling the investigation of exoplanets with much larger significance, the so-called hot- and ultra hot Jupiter type planets. In contrast to our solar system where giant planets orbit the Sun at wide orbits, such Jupiter-type planets (i.e. planets with similar mass and radius to Jupiter) were detected at close orbits in foreign stellar systems with orbital periods in the order of days. Due to the short distance to their host stars, such planets become tidally locked with hemispheres separated into a permanent day- and a permanent nightside, where one may expect the atmosphere to fully evaporate. But the large gravity bounds these planetary atmospheres and prohibits a so-called "catastrophic escape", where the planet loses its gaseous envelope. However note, that recent studies show that also near-UV radiation may introduce "catastrophic escape" on ultra-hot Jupiter type planets (Fossati et al., 2018; Muñoz & Schneider, 2019). Furthermore, atmospheric winds exist on Jupiter type planets (Showman et al., 2008), similar to what is seen on Jupiter in our solar system (Lian & Showman, 2010), which re-distribute the energy within the atmosphere and can cool down the system by irradiating

[1] https://exoplanetarchive.ipac.caltech.edu/, (18.01.2021)
[2] http://phl.upr.edu/projects/habitable-exoplanets-catalog, (04.11.2020)

the radiation back to space on the night-side, leading to lower day-to-nightside temperature contrasts (Burrows, 2014). Winds on hot- Jupiter type planets are triggered mainly from differential heating of the hemispheres which induce pressure gradient forces (Heng & Showman, 2015) and divide into two categories being, a day-to-nightside wind blowing at high altitudes and/or equatorial zonal jet streams at lower altitudes streaming into the direction of the planetary rotation (Miller-Ricci Kempton & Rauscher, 2012; Showman et al., 2008). The day-to-nightside winds manifest themselves in blueward Doppler-shift of absorption lines (see e.g. Snellen et al. (2010b); Wyttenbach et al. (2015); Louden & Wheatley (2015); Brogi et al. (2016)) and atmospheric zonal jet streams mainly in line broadening (Seidel et al., 2020; Gebek & Oza, 2020; Keles et al., 2020; Keles, 2021). The availability of either one or both winds is a complex procedure depending on the redistribution of energy in planetary atmospheres (Showman et al., 2012) and are addressed in different 3D modeling approaches see e.g. Dobbs-Dixon et al. (2010), Perna et al. (2010), Showman & Polvani (2011), Kempton et al. (2014), Zhang et al. (2017), Flowers et al. (2019). Those winds can have large impacts on the dynamics of exoplanets e.g. shifting the hottest point on the dayside, the so-called "hot spot" (Knutson et al., 2008), which can lead to different absorption signature on the eastern and western hemispheres of the planet (Ehrenreich et al., 2020). Due to their enhanced atmospheres showing strong absorption and emission feature which can be used to trace exoplanet properties, Jupiter-type planets are the major class of planets investigated to date and the first exoplanets where atmospheric absorption during transit is detected (Charbonneau et al., 2002).

1.2 Exoplanet detection and characterization methods

1.2.1 Detection of exoplanets: The Transit and RV- method

Different methods can be used to detect and characterize exoplanets (such as direct imaging (Macintosh et al., 2014) or microlensing (Tsapras, 2018)), where especially two methods are pointed out here: The transit method and the radial- velocity (RV)- method.
The former method makes use of the observed stellar flux which becomes diminished during a planetary transit. This decrease in stellar flux observed photometrically over several orbital periods can show the existence of an exoplanet and yields the planetary radius via $\Delta F \sim (R_{pl}/R_*)^2$. The method is illustrated in Figure 1.1, where "(I)"[3] shows the planet at different orbital phases and "(II)"[4] the change in the observed flux which diminishes significantly during transit. For the latter method, as the star and planet show a barycentric motion around their center of mass, the stellar spectral lines show a Doppler-shift to the blue and red wavelengths during the planetary orbital motion, which is illustrated with "(III)"[5] in Figure 1.1. The Doppler-shift can be in the order of $\sim$ 100 m/s level for giant planets in close orbits and $\sim$ dm level for an Earth-sized planet (Birkby, 2018) and observing this spectroscopically, the existence of the planet is inferred and yields the planetary mass dependent on the inclination via $\sim M_{pl} \times \sin(i)$. The benefit of the latter method is that the planet does not need to show a transit to infer a lower limit of the planetary mass. But combining both techniques the inclination can be determined and thus the exact planetary mass. Both methods favor large and heavy planets at closer-orbits which are easier to detect rather than light and small planets.

[3] https://www.nap.edu/read/25187/chapter/6, (14.01.2021)
[4] https://astrobites.org/2016/12/08/a-new-discovery-of-a-secondary-eclipse/, (14.01.2021)
[5] https://www.laserfocusworld.com/test-measurement/research/article/16554881/ultrafast-lasers-frequency-combs-refine-doppler-search-for-distant-planets, (14.01.2021)

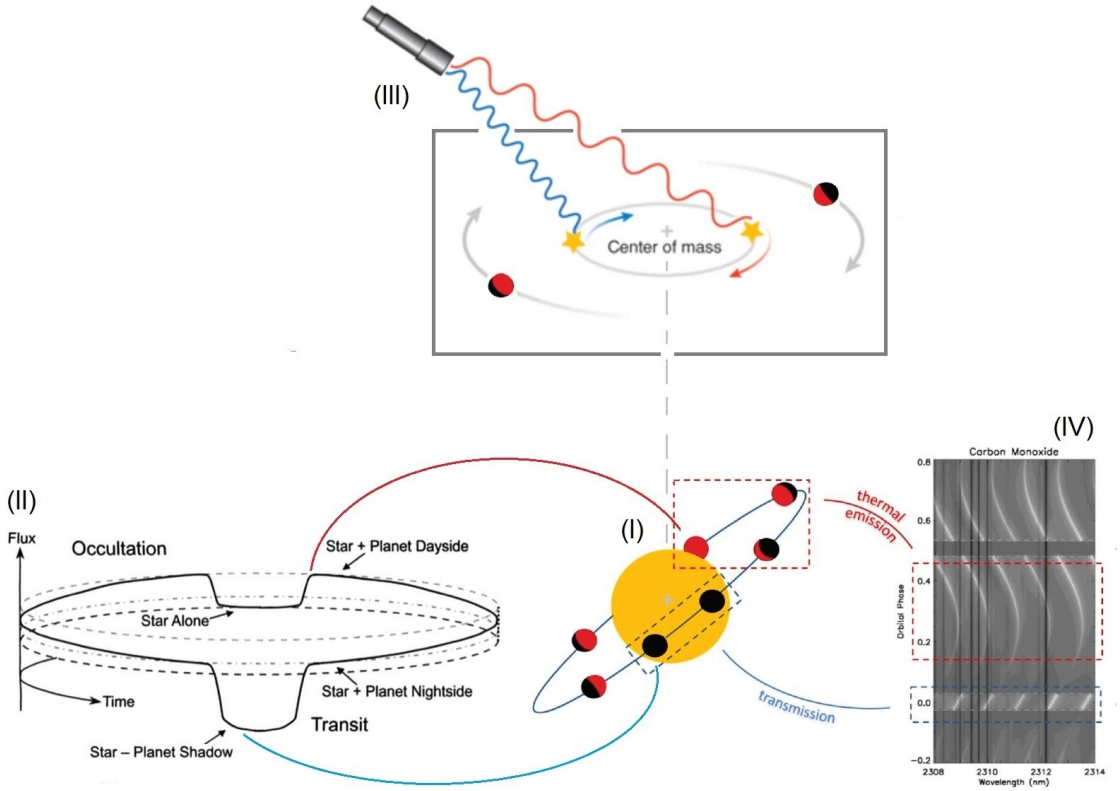

Figure 1.1: Detection and properties of exoplanets: (I) shows an orbiting exoplanet around its host star. The dashed lines illustrate the transit (blue box) and eclipse (red box). (II) shows the change in flux over the different orbital phases, where the solid lines refer to the transit (blue) and eclipse (red) (Winn, 2008). (III) shows the barycentric motion of star and planet around their center of mass which results in blue- and red-shift of stellar spectral lines. (IV) shows the theoretically expected absorption and emission of carbon monoxide from an exoplanet atmosphere which is Doppler-shifted regarding the different orbital phases (Snellen et al., 2010a). (I)-(IV) are updated for illustration purposes.

1.2.2 Characterization of exoplanets: Transits, eclipses and phase curves

Besides the ability to discover planets, especially spectroscopic studies are used to determine planetary and atmospheric properties of the planet during the transit via transmission spectroscopy and during the eclipse via occultation spectroscopy as well as during its position at different orbital phases (see dashed boxes in "(I)" within Figure 1.1). The investigation of transit and eclipse spectra gives complementary information as different atmospheric regions are probed, being the dayside region (for tidally locked planets) in eclipse spectra and the terminator region in the transit observations. During the primary transit, the atmospheric opacities block light at certain wavelengths demonstrating atmospheric absorption or scattering. During the eclipse, the thermal emission and reflection from the planet are blocked (Kreidberg, 2018). The thermal emission from close-in planets is mainly re-radiation of incident stellar flux from the photosphere and the observed spectrum at different wavelengths can be translated into a brightness temperature observed at different altitudes (Madhusudhan, 2019). Comparing the transit (or eclipse) observations with observations shortly before and after the transit (or eclipse), referred to as the transmission (or emission) spectrum, cancel out the stellar contribution and

show the atmospheric signatures, which are Doppler-shifted in their wavelength position with respect to the orbital motion of the planet. This is demonstrated in Figure 1.1, where "(IV)"[6] shows the theoretical absorption and emission of carbon monoxide lines which are Doppler-shifted with respect to the orbital phase. This approach can be used to infer different exoplanet properties such as surface albedos, atmospheric temperature, atmospheric winds, atmospheric composition and more (Kreidberg, 2018; Madhusudhan, 2019). Furthermore, the "phase curve" enables to map surface albedos and temperature at different planetary longitudes as well as to trace atmospheric dynamics (Knutson et al., 2008; Madhusudhan, 2019). With those, i.e. transits, eclipses, and phase curves observations, different aspects of exoplanets became suspect of investigation showing a huge variety, here mentioning only a few reviews (Burrows & Marcy, 2014) accounting for: dynamical processes, evolution, and formation of exoplanet systems (Lithwick & Wu, 2013; Ford, 2014), the population of exoplanets (Batalha, 2014), the detection of planetary atmospheres via photometry and spectroscopy (Burrows, 2014), the habitability of exoplanets and the requirements of life (Kasting et al., 2014; McKay, 2014) and tracing the spectral signature of life, so-called biosignature, on rocky exoplanets (Seager, 2014).

1.3 Fingerprints of exoplanet atmospheres in transmission spectra

Probing planetary atmospheres applying transmission spectroscopy is a wavelength-dependent measure of the extinction due to the planetary atmosphere (Madhusudhan, 2019) and can show the atmospheric composition of especially such gaseous exoplanets, as during the planetary transit a small fraction of the starlight is absorbed by atmospheric constituents, putting a fingerprint on the stellar spectrum (Seager & Sasselov, 2000). The composition of those atmospheres depends on the atmospheric properties of the planet which affects the atmospheric kinetics, where thermochemical reactions dominate at ∼bar pressure regimes due to the large temperature and densities and photochemical reactions dominate at low density ∼bar pressure regimes due to UV and optical flux (Madhusudhan, 2019). However, the planets are expected to contain similar initial composition as their host star (thus showing primordial composition consisting of the main constituents hydrogen, helium, carbon, nitrogen, and oxygen) (Moses, 2014; Kreidberg, 2018). The detectability of an atmospheric constituent depends on one side on its abundance and the other side on its absorption cross-section. However, the investigation of several Jupiter type planets showed that not all planets show absorption signature within their atmospheres during transit (Sing et al., 2016).

1.3.1 Atmospheric opacities: Clouds and hazes

One key effect hiding spectral features are clouds and hazes. Hazes can be understood as clouds of small particles of trace species condensates or UV photolysis products (Burrows, 2014). Such hazes can hide atomic and molecular species or show strong scattering slopes at the optical wavelength range (Kreidberg, 2018) due to Rayleigh scattering by small particles as well as Mie scattering by large particles, whereas the likelihood of clouds rises for planets with lower equilibrium temperature (Madhusudhan, 2019). Note that the apparent planet radius depends on the scale height and atmospheric cross-sections, thus are wavelength-dependent (Burrows, 2014), where such a slope suggests a larger transit depth (Pont et al., 2013). In combination with the diversity of exoplanets where the atmospheric feature can be present and absent, such hazes can complicate the investigation by hiding

[6] https://www.nap.edu/read/25187/chapter/6, (14.01.2021)

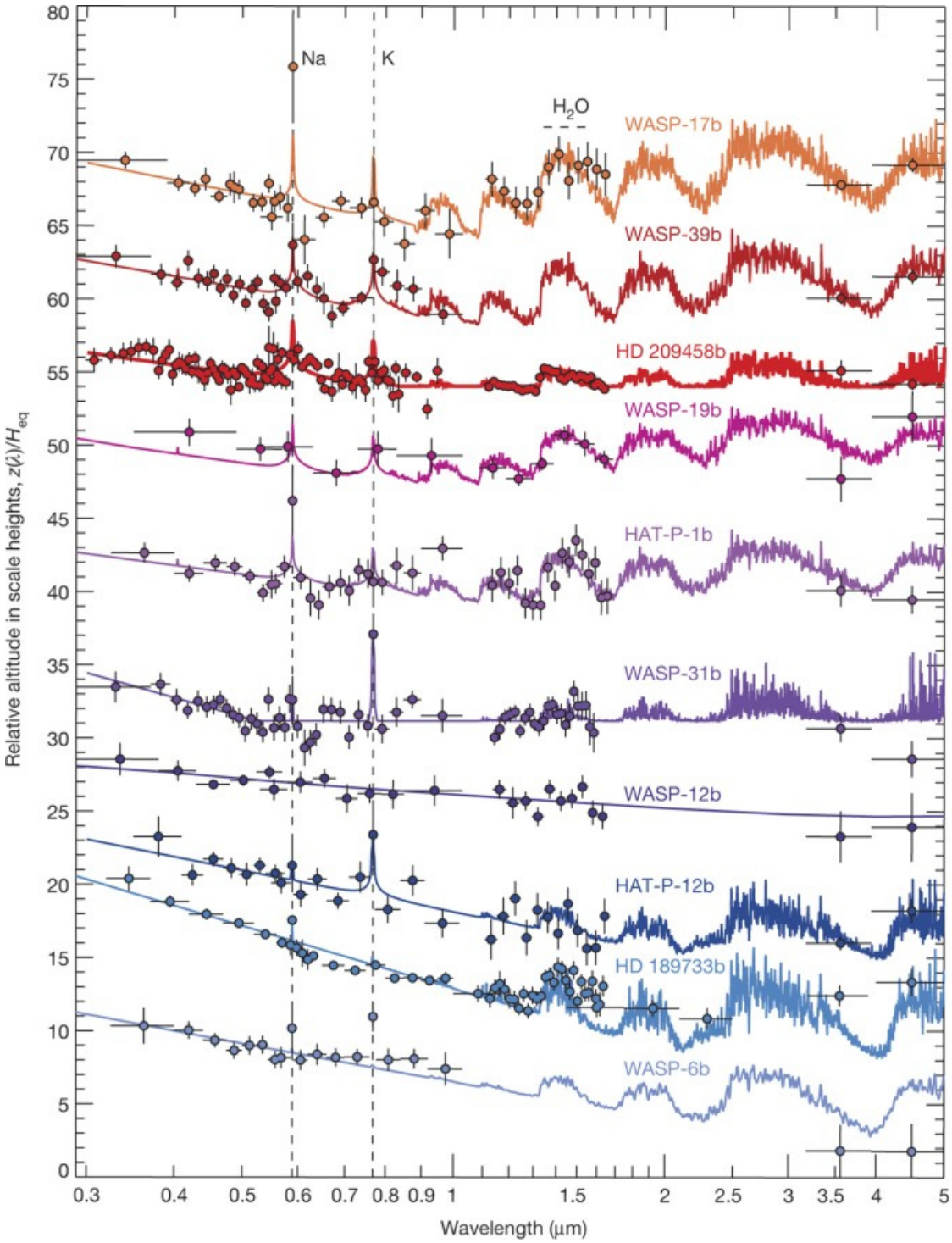

Figure 1.2: Different low-resolution transmission spectra from the optical to the near-infrared wavelength range of gaseous exoplanets together with synthetic spectra (solid) shown by Sing et al. (2016). The y axis shows the relative altitude in scale heights for better visibility.

spectral features and suggest a different atmospheric composition than is the case. This is demonstrated in Figure 1.2, which shows the low-resolution transmission spectra of hot Jupiter type planets covering the optical and the infrared wavelength range observed with the Hubble Space Telescope and the Spitzer Space Telescope. The planetary transmission spectra are diverse, demonstrating the presence and absence of water (expected to be highly abundant) and the alkalis (which are less abundant but have strong absorption cross-section) by comparing the observations with synthetic spectra (Sing et al., 2016).

1.3.2 Atmospheric opacities: Atoms and molecules

One possibility to probe absorption signature by atoms and molecules beyond the cloud deck, if available, is the application of high-resolution observations which probe higher altitudes compared to low-resolution ones (Birkby, 2018). It is worth to emphasize, that atomic and molecular opacities depend on the models which calculate the abundances depending on the atmospheric kinetics but rely on fixed cross-sections. These depend strongly on accurate absorption line lists (Madhusudhan, 2019) from databases such as HITRAN (Gordon et al., 2017a) and HITEMP (Rothman et al., 2010), which are either measured in laboratories or based on quantum chemistry calculations and become especially important in high-resolution observations (Birkby, 2018). Observing in the red and infrared wavelength range, one probe low altitudes where mainly molecules absorb (like H_2O and CO) due to their rotational-vibrational bands, whereas observing in the UV and optical light probes high altitudes where atomic species absorb mainly (Madhusudhan, 2019). As the scattering and absorption cross-section is wavelength-dependent (Burrows, 2014), the transit radius is larger at wavelengths where absorption is present, showing the existence of the constituent of interest (Seager & Sasselov, 2000; Brown, 2001). Absorption signature are stronger on planets which have lower gravity g and mean molecular mass μ but larger atmospheric equilibrium temperature T_{eq} so that the atmospheric scale height H is large (i.e. $H = k_b\ T_{eq}\ \mu^{-1}\ g^{-1}$, with k_b being the Boltzmann constant). For comparison, the amplitude of spectral features expected for Earth-like planets is two to three orders of magnitude smaller than for hot Jupiter type planets (Kreidberg, 2018), favoring the investigation of the latter ones.

1.4 Revealing exoplanet atmospheres

To date, several atmospheric species were detected in exoplanet atmospheres during transit. In low resolution transit observations e.g. Lyman-α absorption by hydrogen (Vidal-Madjar et al., 2003), water absorption (Huitson et al., 2013), evidence of TiO (Sedaghati et al., 2017),evidence of AlO absorption (von Essen et al., 2019) but also scattering signature (Lecavelier des Etangs et al., 2008; Pont et al., 2013) and clouds (Mallonn & Strassmeier, 2016) were detected. Applying high resolution transit observations e.g. hydrogen (Yan & Henning, 2018), helium (Nortmann et al., 2018), titanium and iron (Hoeijmakers et al., 2018), magnesium (Cauley et al., 2019), ionized calcium (Yan et al., 2020) and more (Hoeijmakers et al., 2019) were detected (whereas molecules are only detected in secondary eclipse observations e.g. carbon monoxide (de Kok et al., 2013), water (Birkby, 2018), TiO (Nugroho et al., 2017) and more). Further to these species, especially the alkali lines are of interest for exoplanet investigations. The first detected exoplanet atmosphere showed the absorption of sodium (Na) on the exoplanet HD209458b observed with space-based facilities (Charbonneau et al., 2002) and later on confirmed by ground-based high-resolution observation (Snellen et al., 2008). Later on, being the second detected atmosphere, sodium was detected on the exoplanet HD189733b with ground-based facilities in high-resolution (Redfield et al., 2008). Due to their bright host stars and large

scale heights, these two exoplanets are the most investigated hot Jupiter-type planets to date. Even more surprising, the definite detection of potassium (K) did not happen on HD209458b (Jensen et al., 2011) or HD189733b (Pont et al., 2013; Jensen et al., 2011), although both alkalis show very similar condensation and ionization properties (Lavvas et al., 2014) and so being both predicted.

1.5 This work: Science question and investigation

1.5.1 The Science question

The alkali lines show one of the strongest atmospheric opacities for a hot-Jupiter type planet (Burrows, 2014) and are investigated in different high resolution observations such as Casasayas-Barris et al. (2017); Casasayas-Barris et al. (2019),Chen et al. (2020),Jensen et al. (2011); Jensen et al. (2018), Khalafinejad et al. (2018),Seidel et al. (2019), Wyttenbach et al. (2015, 2017), Žák et al. (2019) and more. Therefore, these lines are excellent species to trace hot Jupiter atmospheres, arising the question:

What kind of atmospheric properties and dynamics of gaseous exoplanets can be inferred from high-resolution alkali line transmission spectroscopy ?

1.5.2 The Investigations

To investigate this science question, we observed the two exoplanets HD189733b and HD209358b during their transit. These hot Jupiter are chosen, as these planets have bright host stars enabling high signal-to-noise observations and have detected sodium in their atmospheres making the presence of potassium reasonable. To investigate this, we used the high-resolution spectrograph PEPSI (Potsdam Echelle Polarimetric and Spectroscopic Instrument) (Strassmeier et al., 2015, 2018a) at the LBT (Large-Binocular-Telescope), which is a binocular telescope with 2 times 8.4 m mirrors. This setup assured high precision and signal-to-noise observations at high spectral resolution, which were required to probe the sharp potassium line absorption arising at high atmospheric altitudes. Its presence, absence and line properties made it possible to investigate the science question which resulted in three publications:

The potassium absorption on HD189733 and HD209458b

Applying high spectral resolution (R$\sim$130 000) transmission spectroscopy of the benchmark exoplanets HD189733b and HD209458b with the high resolution spectrograph PEPSI at the Large-Binocular-Telescope, we investigated the potassium absorption on those planets detecting it on HD189733b, which was also the first high resolution detection of potassium on an exoplanet. The absence of potassium on HD209458b was first intriguing, as for this planet a strong sodium absorption was found in low-resolution observations hinting that potassium may be depleted on this planet by condensation or photo-ionization processes, showing that the atmospheric chemistry on both planets is highly different. Note, that a recent high resolution observation of HD209458b by other authors showed that the detection of sodium may be a spurious signal introduced by the Rossiter-Mc-Laughlin-effect, being in agreement with the non-detection of potassium. The manuscript "The potassium absorption on HD189733 and HD209458b" is published (Keles et al. 2019, Monthly Notices of the Royal Astronomical Society: Letters, Volume 489, Issue 1, October 2019, Pages L37–L41).

Probing the atmosphere of HD189733b with the Nai and Ki lines

With the detection of potassium on HD189733b, we were able to probe its atmospheric properties and dynamics by comparing the atmospheric alkali lines. For this, using the same dataset, we resolved the potassium absorption from the planetary atmosphere and compared this to previous high resolution observation which resolved the sodium absorption on this exoplanet. Comparing the alkali lines with synthetic transmission spectra, we were able to show that both alkali lines probe either different atmospheric altitudes with different temperatures or HD189733b has a way larger Na/K abundance ratio than its host star, hinting that potassium may be depleted. Furthermore, the comparison showed that the sodium lines were significantly stronger broadened than the potassium line, hinting on atmospheric dynamics in form of winds. We derived the expected unbroadened line profiles for HD189733b and estimated the wind strengths. The manuscript "Probing the atmosphere of HD189733b with the Nai and Ki lines" is published (Keles et al. 2020, Monthly Notices of the Royal Astronomical Society, Volume 498, Issue 1, October 2020, Pages 1023–1033).

Spectral signature of atmospheric winds in high resolution transit observations

In the last part of this thesis, I used the derived unbroadened sodium line profile for HD189733b to investigate the atmospheric dynamics on HD189733b. For this, applying a grid model, I investigated the effect of winds in form of zonal equatorial jet streams and if this could introduce enhances broadening to the sodium lines. This work showed that zonal jet streams can broaden the sodium lines on hot and ultra-hot Jupiter type rotating planets in a significant way. Furthermore, by comparing already detected sodium lines on different exoplanets with synthetic spectra, I showed that there is a strong correlation between the equilibrium temperature and line broadening with stronger winds arising on cooler planets. This is in agreement with theoretical expectations, hinting that the ionization of alkali lines on the hotter exoplanets induces Lorentz drag to the winds decreasing their speeds. The manuscript "Spectral signature of atmospheric winds in high resolution transit observations" is accepted (Keles, 2021, Monthly Notices of the Royal Astronomical Society).

1.5.3 Bottom line

To put absorption signature into a bigger context of planetary evolution and formation, especially high resolution observations are able to give new insights on the properties of exoplanets as the inferred absorption profile properties can hint at different atmospheric processes (Brown, 2001). These can be inferred by comparing the observations with forward modeled synthetic line profiles (which rely on specific assumptions such as chemical abundances and chemical equilibrium) or applying atmospheric retrieval techniques (which rely on parametric properties and not on chemical equilibrium) (Madhusudhan, 2018, 2019). Properties such as altitude-temperature profile (Wyttenbach et al., 2015), depletion of alkali elements in atmospheres (Keles et al., 2019), atmospheric escape of hydrogen (Fossati et al., 2018) and its atmospheric number density (Huang et al., 2017), atmospheric elemental ratios (Madhusudhan, 2012; Keles et al., 2020), the presence of aerosols (Pino et al., 2018a,b), atmospheric winds (Seidel et al., 2020; Keles, 2021), the planetary rotation period (Brogi et al., 2016), condensation processes (Ehrenreich et al., 2020) and more can be inferred, making it possible to investigate on the diversity of exoplanet atmospheres.

2 Signature in high-resolution exoplanet observations: approaches and caveats

To infer absorption of atomic and molecular species via transmission spectroscopy, three main methods exist: The "excess method", the "division method" and the "cross-correlation" method. Applying these techniques, different absorption signatures were detected in planetary atmospheres to date, but different effects which can introduce spurious signature must be considered before their application, e.g. the center-to-limb variation (CLV-effect) (Czesla et al., 2015), the Rossiter-McLaughlin (RM)- effect (Rossiter, 1924; McLaughlin, 1924) and the spectral telluric contamination (i.e. absorption and emission by the Earth´s atmosphere). These main effects need to be considered and addressed in high resolution observations to avoid spurious signature in transmission spectra (see e.g. Casasayas-Barris et al. (2019); Keles et al. (2019); Cauley et al. (2020); Wyttenbach et al. (2020); Keles et al. (2020); Chen et al. (2020); Yan et al. (2020); Wyttenbach et al. (2020) and more). Within this work, models were developed to account for these three effects and demonstrated in Manuscript I and Manuscript II. Note, that these effects will be of importance for each detection method applied, however, some effects are of more importance for some detection techniques as reconsidered below.

2.1 The "excess method" and the effect of the stellar center-to-limb variation

Applying the "excess method" in low- and high-resolution observations, the spectral flux where atomic absorption is expected is integrated within a bandwidth and divided by the same amount of flux integrated within a spectral region where planetary absorption is not expected (Charbonneau et al., 2002; Keles et al., 2019). Increasing the bandwidth, the absorption level decreases, showing the finite absorption by the planetary atmosphere. The absorption level inferred from the "excess curve" can be used to calculate the number of scale heights probed by the absorbing species (Wyttenbach et al., 2015) and compared to other absorbing species within the atmosphere (Keles et al., 2019). Note, that the exact position of the bandwidth can affect the "absorption level" depending on the scatter and noise within the spectra, thus different reference bands should be considered accounting for this approach. Keles et al. (2019) showed that, with sufficiently high S/N observations, it is possible to normalize by the continuum of the excess light curve instead of dividing this by a reference band, decreasing this scatter. One effect becoming especially important applying this approach is the CLV- effect. The CLV- effect arises due to the differential limb darkening on the stellar surface, where the planet blocks different amount of photons during its transit at the stellar line core and stellar continuum which leads to darkening or brightening effects (Czesla et al., 2015; Yan et al., 2017). This can introduce emission and absorption like features in "excess light curves", especially for small bandwidths used. Figure 2.1 shows the illustration of the CLV- effect at the alkali lines for the transiting exoplanet HD189733b. The stellar spectral alkali lines are shown on the top left and right arising from the different regions μ on the stellar surface (mark the color-coding). The lightcurve during transit at the line core ("clvline") and continuum ("clvcont") are shown below the transit illustration. At the lower left and right the CLV-curves from

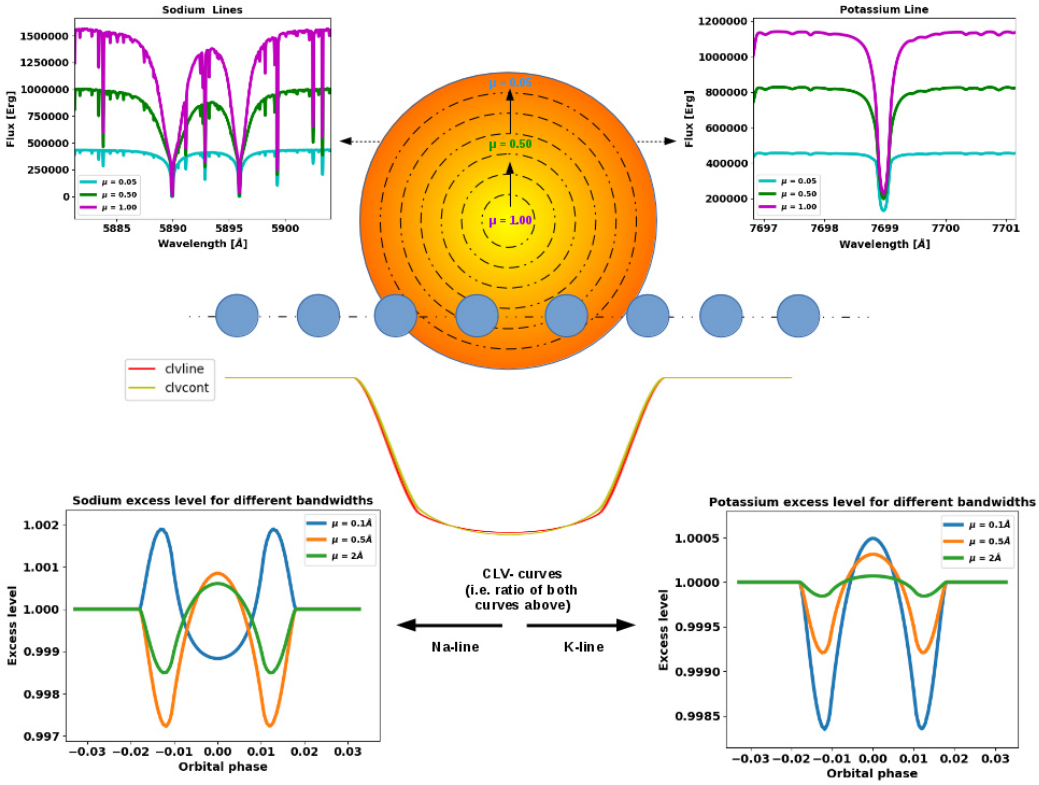

Figure 2.1: Illustration of the CLV-effect: The stellar spectral lines arising from different surface regions are demonstrated top left (sodium) and top right (potassium). "clvline" and "clvcont" shows the transit lightcurve in the line core and continuum, respectively. The division of both results in the CLV-effect (lower left and right), which show emission- and absorption like feature in "excess absorption curves". The amplitude of the feature decreases for larger integration bandwidths (see legend).

the developed model for different integration bandwidths (see legend) are shown which manifest themselves in "excess curves". Note, that the CLV-effect depends on the stellar properties calculated by 1D stellar spectra, which could under- or overestimate this effect within the excess light curves. Further information are provided in Manuscript I.

2.2 The "division method" and the residual RM- effect

With sufficiently high spectral resolution and signal-to-noise observations, atomic absorption can also be inferred by the "division method", where one divides the observed spectra acquired during the transit by the mean of the out-of- transit observations, showing the spectrally resolved planetary absorption (Wyttenbach et al., 2015) in the so-called "transmission spectrum". During the transit, a wavelength shift (or Doppler shift) is introduced to the absorption signature within the spectra by the planetary motion in the order of dozens of km/s for hot Jupiter type planets (Birkby, 2018). The Doppler-shifted absorption signature visible at different phases during the transit demonstrates that the signature is arising by the absorbing species within the planetary atmosphere. By shifting the absorption profiles back to the planetary rest frame and co-adding them, the planetary

absorption is shown (Keles et al., 2020). With this method, different further atmospheric properties can be inferred such as asymmetric absorption arising from the planetary hemispheres at the trailing limb (the limb of the planet moving towards us) and leading limb (the limb of the planet moving away from us) (Ehrenreich et al., 2020), atmospheric day-to-nightside winds which introduce blueshifts to spectral lines (Louden & Wheatley, 2015) or hints on evaporating atmospheres showing very strong absorption signature which are close to the Roche-lobe (i.e. the region around the planet in which the material is gravitationally bound) (Yan & Henning, 2018). But several effects which can introduce spurious signature in transmission spectra need to be considered for the "division method" (Wyttenbach et al., 2020). For instance, it is of main importance to account correctly for the expected Doppler-shifts of the planetary absorption profiles, where small deviations will introduce spurious signature to the inferred line profile or even vanish out the absorption signature (Cauley et al., 2020). Of further special interest is the residual RM- effect. The RM -effect (Rossiter, 1924; McLaughlin, 1924) arises as during transit the planet blocks different strong blue- and redshifted light components coming from the stellar surface due to the stellar rotation. This introduces a shift and deformation to the stellar line profile compared to the mean stellar line profile which is not blocked by a transiting planet. Due to this, by creating the transmission spectrum, a residual feature arises. This effect can cause large spurious signals and have a huge impact on the absorption feasibility, as demonstrated by Casasayas-Barris et al. (2020), who showed that the first detection of a planetary atmosphere on HD209458b by Charbonneau et al. (2002) may be attributed to this effect. However, the modeling of this effect can be challenging as it depends on the star/planet contrast, stellar parameter, orbital velocities, 1D stellar spectra and more (Yan et al., 2020). Figure 2.2 shows the residual RM-effect from the developed model for the investigation of the transmission spectrum of HD189733b (Manuscript II). The illustration shows a transiting planet (from left to right) in front of the star. The color-coding shows the stellar rotation velocity in km/s i.e. left hemisphere moving towards us and the right hemisphere moving away from us. The planet blocks at different positions in front of the star different Doppler-shifted stellar line profiles, where their division required to create the transmission spectrum introduces residual feature (see right panel). Further information are provided in Manuscript II.

2.3 The "cross-correlation method"

For atomic and molecular absorption which are to shallow to be resolved in single lines and thus hidden in the stellar noise (Birkby, 2018), the "cross-correlation method" can be applied. Here, the observed spectra are compared to absorption templates which usually have unique properties accounting for a high number of absorption lines (Hoeijmakers et al., 2018; Hoeijmakers et al., 2019), which increase the detection significance via $\sim \sqrt{N_{\rm lines}}$. However, in low-resolution observations the line depths become shallower and blended with other lines, making this method more suitable for high-resolution investigations (Birkby, 2018). Another way around, this technique depends strongly on accurate templates which base on accurate line lists with shape and position of the expected absorption lines (Birkby, 2018). With such cross-correlation, also the radial velocity semi-amplitude of the planet can be inferred, which results in the determination of the planetary mass and inclination separately also for non-transiting planets (Birkby, 2018). This technique is used extensively also in secondary eclipse observations to investigate the presence or absence of atoms and molecules to investigate e.g. winds (Snellen et al., 2010b) or temperature inversion (caused by the absorption of UV light and emission of thermal light) predicted in ultra-hot Jupiter atmospheres (Fortney et al., 2008) due to TiO (Nugroho et al., 2017) or, predicted recently, due to Fe- lines (Yan et al., 2020; Pino et al., 2020).

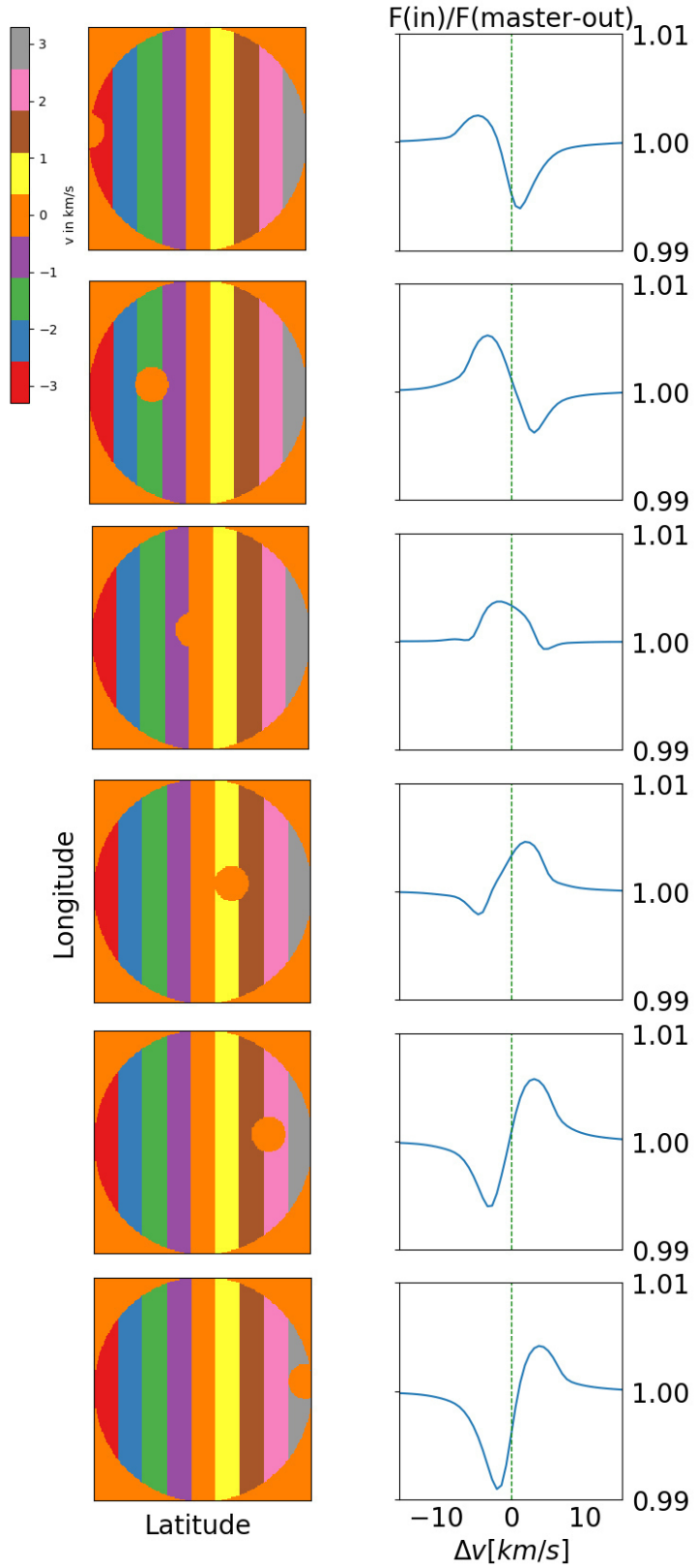

Figure 2.2: Illustration of the residual RM-effect for the transit of HD189733b. Left panel: The planet transits (orange dot) from left to right and blocks different Doppler-shifted light arising from the stellar surface (colour-coding shows the velocity in km/s). Right panel: Dividing the stellar spectra inferred during transit and out-of-transit leads to a residual feature within the transmission spectra.

3 Overview of the Manuscripts

The Manuscripts demonstrated hereafter show the manuscript versions accepted by the Referee and Editor for publication. The format of the Manuscripts is adapted to match the style of the thesis. The bibliography for all chapters is shown at the end of the thesis.

3.1 Manuscript I: "The potassium absorption on HD189733 and HD209458b", Monthly Notices of the Royal Astronomical Society: Letters, Volume 489, Issue 1, Pages L37–L41, October 2019

Authors:] Engin Keles,[1] Matthias Mallonn,[1] Carolina von Essen,[2] Thorsten A. Carroll,[1] Xanthippi Alexoudi,[1] Lorenzo Pino,[3] Ilya Ilyin,[1] Katja Poppenhäger,[1] Daniel Kitzmann,[4] Valerio Nascimbeni,[5,6] Jake D. Turner,[7,8] Klaus G. Strassmeier[1]

[1]Leibniz-Institut für Astrophysik Potsdam (AIP), 14482 Potsdam, Germany
[2]Stellar Astrophysics Centre, Department of Physics and Astronomy, Aarhus University, Aarhus C, Denmark
[3]Leiden Observatory, Leiden University, 2300 RA Leiden, The Netherlands
[4]University of Bern, Center for Space and Habitability, CH-3012, Bern, Switzerland
[5]Istituto Nazionale di Astrofisica, Osservatorio Astronomico di Padova, 35122 Padova, Italy
[6]Dipartimento di Fisica e Astronomia - Universta di Padova, 35122 Padova, Italy
[7]Cornell University, Ithaca, New York, USA;
[8]University of Virginia, Charlottesville, Virginia, USA

Contributions: I did the entire data analysis and interpretation of the results. I wrote the whole text, except parts within Section 7.3 dealing with the data reduction process, which is done by Ilya Ilin and parts dealing with the 1D stellar spectra, which is done by Thorsten A. Carroll. I developed the models accounting for the CLV- effect and telluric lines as well as the "excess absorption".
Besides scientific discussions with all Co-authors, the 1D-stellar spectra needed for the CLV-model are delivered by Thorsten A. Carroll. The telluric model bases on "hapi", which is provided by the HITRAN database calculating absorption cross-sections and profiles. The data reduction is applied by Ilya Ilin. Furthermore, *Pyastronomy* tools are used, which are open source tools.

3.2 Manuscript II: "Probing the atmosphere of HD189733b with the Nai and Ki lines", Monthly Notices of the Royal Astronomical Society, Volume 498, Issue 1, Pages 1023–1033, October 2020

Authors:] E. Keles,[1] D. Kitzmann,[2] M. Mallonn,[1] X. Alexoudi,[1] L. Fossati,[3] L. Pino,[4,5] J. V. Seidel ,[6] T. A. Carroll,[1] M. Steffen,[1] I. Ilyin,[1] K. Poppenhäger,[1] K. G. Strassmeier[1] C. von Essen,[7] V. Nascimbeni,[8,9] J. D. Turner,[10,11]

[1]Leibniz-Institut für Astrophysik Potsdam (AIP), 14482 Potsdam, Germany
[2]University of Bern, Center for Space and Habitability, CH-3012, Bern, Switzerland
[3]Space Research Institute, Austrian Academy of Sciences, 8042 Graz, Austria
[4]Anton Pannekoek Institute for Astronomy, University of Amsterdam, 1098 XH Amsterdam, The Netherlands
[5]INAF-Osservatorio Astrofisico di Arcetri, I-50125 Firenze, Italy
[6]Observatoire de l'Université de Genève, 1290 Versoix, Switzerland
[7]Stellar Astrophysics Centre, Department of Physics and Astronomy, Aarhus University, 8000 Aarhus C, Denmark
[8]Istituto Nazionale di Astrofisica, Osservatorio Astronomico di Padova, 35122 Padova, Italy
[9]Dipartimento di Fisica e Astronomia - Universta di Padova, I-35122 Padova
[10]Cornell University, Ithaca, New York, USA;
[11]University of Virginia, Charlottesville, Virginia, USA

Contributions: I did the entire data analysis and interpretation of the results. I wrote the whole text, except parts within Section 8.5.3 and 8.1.0 dealing with the synthetic spectra, which is provided by Daniel Kitzmann and Section 8.12 dealing with the stellar Na/K ratio provided by Matthias Steffen. I developed the models accounting for the RM-effect, transmission spectra and the broadening model.
Besides scientific discussions with all Co-authors, the 1D-stellar spectra needed for the residual RM-model are delivered by Thorsten A. Carroll. The data reduction is applied by Ilya Ilin. Furthermore, *Pyastronomy* tools are used, which are open source tools.

3.3 Manuscript III: "Spectral signature of atmospheric winds in high resolution transit observations", Monthly Notices of the Royal Astronomical Society, accepted 2021 January 11

Authors:] E. Keles,[1]

[1]Leibniz-Institut für Astrophysik Potsdam (AIP), An der Sternwarte 16, 14482 Potsdam, Germany

Contributions: I did the entire data analysis and interpretation of the results. I wrote the whole text and developed the model accounting for different atmospheric winds.
The synthetic spectra model bases on *petitradtrans*, which is an open-source tool. Furthermore, *Pyastronomy* tools are used, which are open source tools.

4 The potassium absorption on HD189733b and HD209458b

4.1 Abstract

In this work, we investigate the potassium excess absorption around 7699Å of the exoplanets HD189733b and HD209458b. For this purpose, we used high spectral resolution transit observations acquired with the 2 × 8.4m Large Binocular Telescope (LBT) and the Potsdam Echelle Polarimetric and Spectroscopic Instrument (PEPSI). For a bandwidth of 0.8Å, we present a detection > 7-σ with an absorption level of 0.18 % for HD189733b. Applying the same analysis to HD209458b, we can set 3-σ upper limit of 0.09%, even though we do not detect a Ki- excess absorption. The investigation suggests that the Ki-feature is less present in the atmosphere of HD209458b than in the one of HD189733b. This comparison confirms previous claims that the atmospheres of these two planets must have fundamentally different properties.

4.2 Introduction

A suitable method for the characterization of planetary atmospheres is transmission spectroscopy (Seager & Sasselov, 2000). During transit, a small fraction of the starlight is absorbed or scattered by atoms and molecules, putting a fingerprint on the stellar spectrum. One possibility to infer these fingerprints is the "excess absorption" method, where the flux of the spectral range of interest is integrated within a bandwidth and divided by the flux within a reference band (a spectral region where planetary absorption is not expected), showing the absorption within the atmosphere during the transit (Charbonneau et al., 2002). Especially hot giant planets are suitable targets of these kind of investigations due to their large scale heights and short orbital periods, where several atmospheric constituents have been successfully detected e.g. sodium (Redfield et al., 2008; Snellen et al., 2008; Casasayas-Barris et al., 2017), potassium (Sing et al., 2011), titanium and iron (Hoeijmakers et al., 2018), hydrogen (Yan & Henning, 2018), and magnesium (Cauley et al., 2019).
For hot Jupiter atmospheres with T $\sim$ 1500K, the strongest atomic absorber in the optical wavelengths are Nai and Ki (Fortney et al., 2010). Different investigations on HD189733b and HD209458b have confirmed the presence of Nai using low- and high resolution spectroscopy (see e.g. for HD209458b Charbonneau et al. (2002) and Snellen et al. (2008) or for HD189733b Redfield et al. (2008) and Wyttenbach et al. (2015)). However, the detection of Ki was not yet assured from high resolution investigations for any exoplanet, although attempts were made e.g. recently by Gibson et al. (2019) investigating Ki on the exoplanet Wasp-31b.
Several investigations attempted to detect Ki on HD189733b and HD209458b. For instance, Jensen et al. (2011) used the Hobby-Eberly-Telescope and stated a non-detection of Ki for both exoplanets. A tentative 2.5-σ detection of Ki in the atmosphere of HD189733b was claimed by Pont et al. (2013) using the ACS camera at the Hubble Space Telescope. To date, there is no significant detection of Ki for these two exoplanets, neither in low- nor in high- resolution observations.

4.3 Observations

We observed one transit for HD189733b on October 11, 2017 at 01:47 – 06:39 UT (PI: J.D. Turner, UVA) and one transit for HD209458b on October 13, 2017 at 03:03 – 08:04 UT (PI: K.G. Strassmeier, AIP) using the PEPSI instrument (Strassmeier et al., 2015, 2018b) with a 3.2– pixel resolution of 130 000 at the LBT operated in the binocular mode. The wavelength region of interest was covered with cross disperser VI (7340 Å – 9070 Å) in the polarimetric mode and the beams recombined yielding the integral light spectrum. The spectrograph is a white–pupil fiber–fed spectrograph located in a pressure-controlled chamber at a constant pressure, temperature and humidity to ensure constant refractive index of the air inside, providing radial velocity stability about 5 m/s on the long term and less than 0.5 m/s on the short term (Strassmeier et al., 2018a).
For the HD189733b transit, we obtained 24 spectra (15 out-of-transit (OOT) and 9 in-transit (IT)) setting the exposure time to 10 min. We exclude one OOT exposure due to a systematically lower relative flux determination. The resulting signal-to-noise ratio (S/N) in the final processed data varied due to increase in airmass during the night in the Ki line at 7699 Å from around 160 to 70 and at the continuum at 7700 Å from around 540 to 270. For the HD209458b transit, we obtained 17 spectra (9 OOT and 8 IT) setting the exposure time to 10 min. The observations paused from 06:26 UT – 07:19 UT due to bad weather conditions, leading to a loss of phase coverage at the second part of the transit. The resulting S/N in the final processed data varied due to an increase in airmass during the night in the Ki line at 7699 Å from around 230 to 80 and at the continuum at 7700 Å from around 425 to 160.
The image processing steps includes bias subtraction and variance estimation of the source images, super–master flat field correction for the CCD spatial noise, echelle orders definition from the tracing flats, scattered light subtraction, wavelength solution for the ThAr images, optimal extraction of image slicers and cosmic spikes elimination of the target image, wavelength calibration and merging slices in each order, normalization to the master flat field spectrum to remove CCD fringes and blaze function, a global 2D fit to the continuum of the normalized image, and rectification of all spectral orders in the image to a 1D spectrum. The software numerical toolkit and graphical interface application for PEPSI is described in Strassmeier et al. (2018a), and its complete description is in preparation by Ilyin (2019).
The blaze function was removed by the division of the master flat field spectrum. The residual spectra were fitted with a low order 2D spline with subsequent rectification of spectral orders where the overlapping parts of spectral orders were averaged with their weights as the inverse variances of the individual wavelength pixels. After that, the continuum of individual spectra was corrected again with the mean spectrum as the weighted average of all the observed spectra. The mean spectrum was normalized to its continuum and each observed spectrum was divided by the mean normalized spectrum. A low order spline fit to the ratio constitutes the final continuum of the individual spectrum.

4.4 Data Analysis

The Ki doublet absorption lines are at 7698.98 Å and 7664.92 Å (see bottom panels of Figure 4.1). Since the latter line is surrounded by a strong pair of telluric oxygen lines, we focus our analysis only on the line at 7698.98 Å. To demonstrate the reliability of the excess absorption, we apply the same procedure on several control lines, where we do not expect planetary absorption (see e.g. Redfield et al. (2008)). Each chosen control line is free of telluric contamination and has a normalized flux level < 0.5 in the line centre. We use

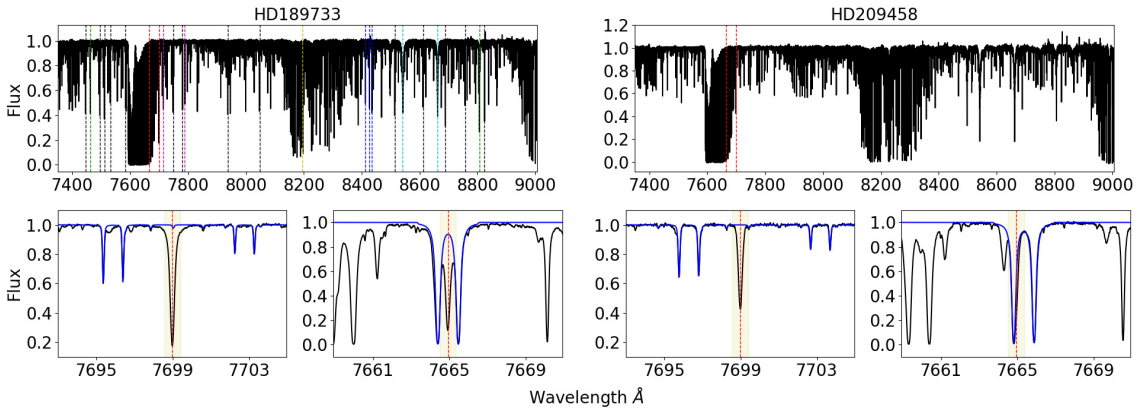

Figure 4.1: Full PEPSI spectra (top) and Ki lines (bottom). Dashed lines mark the Ki lines (red) and control lines (colored) and the solid blue line mark the telluric model for few telluric lines. Shaded area shows the planetary motion of around ±0.42Å during the transit.

synthetic stellar spectra to model the center-to-limb variation (CLV) (see Section 4.4.3) to avoid a false-positive detection. Top panels in Figure 4.1 show PEPSI spectra of the targets.

4.4.1 Telluric lines

Telluric lines are spectral features induced by Earths atmosphere. To investigate if telluric line contamination has an effect on the results (as the HD189733 spectra exhibit a weak telluric line at 7699 Å), each spectrum is telluric corrected around the Ki lines (see bottom panel of Figure 4.1) and then sampled to a common wavelength grid using a spline function. For this, we developed a telluric line corrector called "Telluric Hapi Observation Reducer" (THOR), which uses the "HITRAN Application Programming Interface" (HAPI) as a basis (Kochanov et al., 2016). HAPI consists of different python routines enabling the calculation of absorption spectra using line-by-line data provided by the HITRAN database (Gordon et al., 2017b). THOR iterates HAPI for different parameters (e.g. wavelength shifts, wavelength resolution, mean free path) until it reaches a χ^2 – min between the observed and modelled telluric lines. To prove the reliability of our telluric correction, we verify the increase in line depth with airmass for the modelled telluric line at 7699 Å applying a Pearson correlation test, which result in a value of 0.90 (thus showing high correlation). As the telluric contamination is weak, the excess level shown in Section 6.5 do not change within 1-σ either applying telluric correction or not. For further analysis, we use the telluric corrected spectra.

4.4.2 Excess absorption

For both targets, the planetary motion during the transit of around ±16 km/s introduces a shift in the absorption wavelength of approximately ±0.42Å. To search for the Ki excess absorption, we use bandwidths from 0.8 Å to 10.0 Å in steps of 0.4 Å (whereby one pixel corresponds to ∼0.016 mÅ). This lower limit of the bandwidth ensures that a major part of the planetary absorption (shifted by the planetary motion) is inside the integration band. The lower limit also contains a major part of the spectral line, avoiding artifacts introduced by line shape changes (Snellen et al., 2008) due to the Rossiter- McLaughlin-

effect.
We use two methods to infer the planetary excess absorption. First, we follow the "traditional" way, integrating the flux in the spectral range of interest and dividing it by the mean of the integrated flux (at same bandwidth) at two reference positions adjacent to the red and blue. The center of the reference bands for the HD189733b investigation are at 7693.40 Å and 7700.40 Å and for the HD209458b investigation at 7692.40 Å and 7705.40 Å. Second, we will infer the excess absorption by using no reference bands at all (thus only integrating the flux in the Ki-line). This is possible for high S/N continuum normalized spectra with stable blaze functions. For both of these methods, we made use of a 2-order polynomial fit to the OOT data for normalization.
The error bars are calculated using the uncertainties sourcing from the photon and readout noise propagated in the data. They are scaled according to the standard deviation of the OOT values, if the mean error was underestimated compared to this standard deviation. We determine the excess absorption level using a Markov-Chain Monte Carlo (MCMC) method provided by PyAstronomy (a collection of Python routines implemented in the PyMC (Patil et al., 2010) and SciPy packages (Jones et al., 01), where we simulate a transit and scale the area of a planetary body to mimic an absorbing atmosphere. We applied 100 000 MCMC iterations (rejecting the first 30000 samples as burn-in phase) to ensure that the final best-fit is provided. We checked for convergence of the chains by splitting them in three equally sized sub-groups and verified that their individual mean agreed within 1-σ, whereby their individual uncertainty agree within 3.5%. The uncertainties for the excess absorption level correspond to a 1-σ confidence level.

4.4.3 Center-to-limb variation

As the planet covers different parts of the stellar surface during its transit, the differential limb darkening between the line core and the stellar continuum leads to darkening or brightening effects, which are evident in the excess absorption curves. A detailed discussion of the CLV effect and its influence on excess absorption curves is shown e.g. in Czesla et al. (2015) and Yan et al. (2017).
We simulate a transit to derive the CLV curves using synthetic stellar spectra, which are calculated using the "spectrum" program by R.O. Gray (Gray & Corbally, 1994). For the calculation of the model atmospheres we used the Kurucz model (Kurucz, 1970; Castelli & Kurucz, 2004). For HD189733b, we used an effective temperature of 4875 K, a surface gravity of log g = 4.56 and a metallicity of dex -0.03. For HD209458b, we used an effective temperature of 6092 K, a surface gravity of log g = 4.25 and a metallicity of dex 0.02 (see also Boyajian et al. (2015) for comparison). We set $\mu = \cos\theta$ to specify the limb angle, whereby $\mu = 0$ refers to the limb and $\mu = 1$ to the center of the disk. We generated 20 spectra with limb angles between $\mu = 0$ and $\mu = 1$ with a spacing of 0.05.
To derive the CLV curves, the stellar surface is mapped by a grid of 100 × 100 pixels containing the limb angle dependent fluxes and the planetary surface is mapped by 31.6 × 31.6 pixels (whereby higher pixel values did not change significantly the results, but increased the computational time). For each planet position in front of the star, we calculate the total stellar limb angle dependent flux at the position where we expect planetary absorption and the reference band position. The CLV- curve is then produced by the same way as the excess curve. We validated our model by comparing the CLV effect for the sodium excess absorption simulated for HD189733b by Yan et al. (2017), getting similar results.

BW[Å]	EA[%]
0.8	0.184 ± 0.022
1.2	0.139 ± 0.017
1.6	0.116 ± 0.016
2.0	0.108 ± 0.021
2.4	0.087 ± 0.020
2.8	0.084 ± 0.018
3.2	0.079 ± 0.018
3.6	0.074 ± 0.018
4.0	0.068 ± 0.018
4.4	0.064 ± 0.017
4.8	0.060 ± 0.017
5.2	0.057 ± 0.016
5.6	0.060 ± 0.015
6.0	0.058 ± 0.014
6.4	0.059 ± 0.014
6.8	0.054 ± 0.014
7.2	0.049 ± 0.013
7.6	0.049 ± 0.013
8.0	0.050 ± 0.012

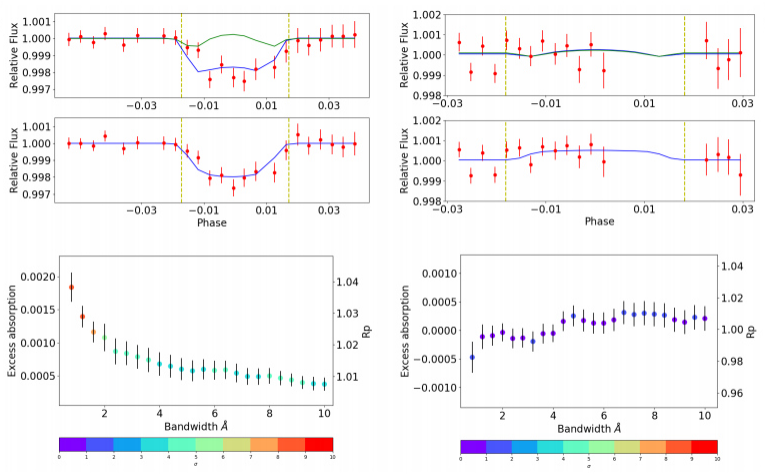

BW[Å]	EA[%]
0.8	-0.047 ± 0.028
1.2	-0.011 ± 0.021
1.6	-0.009 ± 0.018
2.0	-0.004 ± 0.016
2.4	-0.014 ± 0.018
2.8	-0.013 ± 0.017
3.2	-0.019 ± 0.017
3.6	-0.006 ± 0.017
4.0	-0.005 ± 0.016
4.4	0.016 ± 0.017
4.8	0.025 ± 0.018
5.2	0.017 ± 0.019
5.6	0.013 ± 0.018
6.0	0.013 ± 0.019
6.4	0.018 ± 0.019
6.8	0.031 ± 0.020
7.2	0.028 ± 0.021
7.6	0.030 ± 0.021
8.0	0.028 ± 0.021

Figure 4.2: K excess absorption (EA) for HD189733b (left) and HD209458b (right). EA curves at 0.8 Å bandwidth (BW) using reference bands (top) and no reference bands (middle). Bottom panel shows the EA level for different BW. Green line shows the CLV-curve and the blue line the planetary absorption (both mirrored to mimic the second half of the transit for HD209458b). Tables show EA up to 8Å.

4.5 Results

4.5.1 Investigating potassium on HD189733b

The left panel of Figure 4.2 shows the mean excess absorption curve for HD189733b at a 0.8 Å integration band using adjacent reference bands (top) and no reference bands (middle). The blue curve shows the MCMC fit and the green solid line represents the CLV effect. As the CLV effect has a negligible effect on the overall excess absorption, we neglect it in the middle panel. The excess absorption levels are 0.181 % ± 0.022 % (top) and 0.184 % ± 0.025 % (middle), thus similar within their error bars. This shows that both methods are suitable to infer the planetary excess absorption. This absorption value corresponds to ∼13 scale heights, hinting that the absorption must originate at high altitudes in the atmosphere. The left bottom panel shows the mean absorption for different bandwidths (using no reference bands) and the significance level. By increasing the bandwidth more than 0.8 Å, the absorption level decreases, as expected, due to the integration of less atmospheric Ki absorption relative to the continuum flux. Also shown on the right y-scale is the apparent planetary radius i.e. the radius until which the atmosphere is opaque in units of the white light radius. The significance level of the Ki detection for the 0.8 Å bandwidth is determined with > 7-σ with respect to the zero level. For the remaining other bandwidths, the determined excess absorption levels are also above 3-σ with respect to the zero level.

Comparing our results to other investigations, we can qualitatively confirm the tentative Ki- detection of Pont et al. (2013). Other way around, Jensen et al. (2011) investigated at a resolution of 60 000 potassium on HD189733b, stating a non-detection. In their work, they averaged the IT and OOT spectra from several observations to produce one master F_{in}/F_{out} spectrum and determined thereafter from this the excess absorption. To do this, they subtracted the integrated flux from the line core at the Ki-line from the mean of two reference band fluxes using an 8Å integration band deriving an excess level of (-0.77 ± 1.04) x 10^{-4}. Determining the excess absorption at 8Å bandwidth, we infer an excess absorption value of (4.95 ± 1.20) x 10^{-4}, deviating significantly more than 3-σ from their

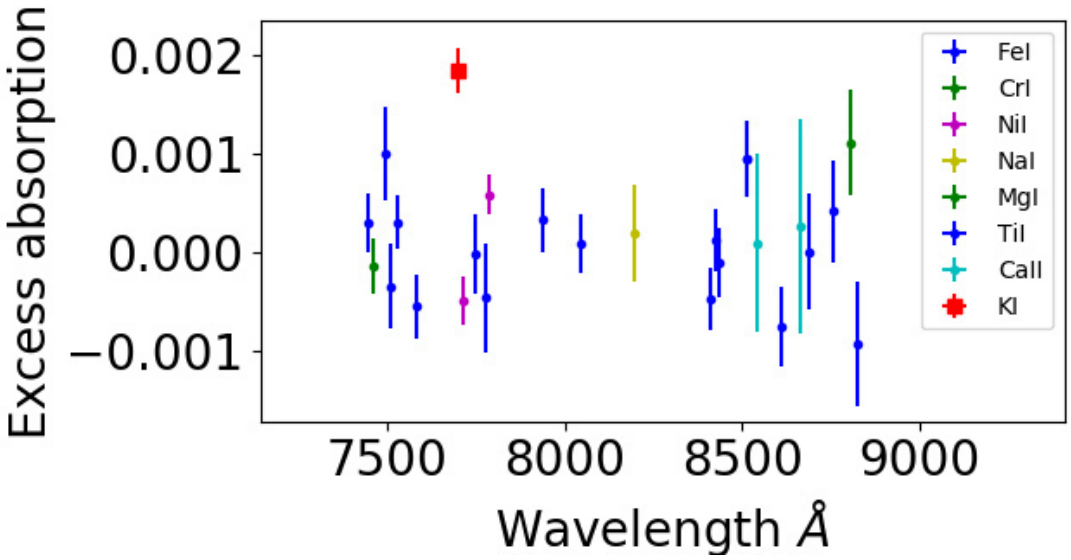

Figure 4.3: Mean excess absorption for several control lines compared to Ki (red square) at 0.8 Å bandwidth for HD189733b.

findings. Possible reasons which could explain this discrepancy are e.g. telluric lines and stellar activity in some of the observations which can affect the combined master spectra or even the difference in the technique used to derive the excess level.
Figure 4.3 shows the excess level at a 0.8 Å integration band (using no reference bands) for several control lines which all lie within 3-σ around zero opposite to the excess level at the Ki- line at 7698.98 Å (red square). The significance level of the Ki absorption remains $>$ 3-σ with respect to the standard deviation of the excess level for the control lines, presenting a strong evidence on the atmospheric Ki- absorption.

4.5.2 Stellar activity of HD189733

As the star HD189733 is an active K-dwarf, the stellar variability could cause errors in the determined excess levels e.g. by flares (Klocová et al., 2017; Khalafinejad et al., 2017; Cauley et al., 2018). Cauley et al. (2018) showed for HD189733b that the transit of active latitudes with bright facular and plage regions can cause emission feature in stellar lines. Also the strong magnetic field of HD189733 could have a significant effect on the emission in lines (Cauley et al., 2017). Possibly related to the activity, we see an emission-like feature in several stellar line cores as e.g. in Nai (8183.28 Å), Fei (7511.03 Å) and the investigated Ki line (7698.98 Å). As the integrated flux in the line core is low compared to the integrated flux over the line width (of at least 0.8Å), this has a negligible influence on the result. Moreover, this feature increases over the night and it is not restricted to the transit, opposite to the excess absorption in Figure 4.2, which appears only during the transit, making us confident about the Ki absorption within the atmosphere of HD189733b.

4.5.3 Investigating potassium on HD209458b

The right panel in Figure 4.2 shows the same approach on HD209458b as for HD189733b. Similar to HD189733b, the CLV- effect is very weak and does not affect the result. In contrast, there is no excess absorption evident at the investigated bandwidths, either using reference bands or not. Moreover, the result suggests an emission like behaviour

at low bandwidths. Assuming zero excess absorption to not underestimate the error (as a negative excess level would suggest emission either than absorption), we determine a 3-σ upper limit of around 0.084% at a bandwidth of 0.8Å. Concluding, in comparison to HD189733b, HD209458b shows no significant absorption of potassium in its atmosphere.

4.6 Discussion

Although both targets could have experienced different evolutionary scenarios, changing their primordial atmospheres leading to different atmospheric composition and properties, we make the assumption that the initial alkali metal abundances could be similar for both targets, as they orbit a host star of solar metallicity (Boyajian et al., 2015). As gas giants form and accrete H/He-dominated gas, they also accrete planetesimals that enrich their envelope in metals, thus they can possess even a higher absolute metellicity compared to the parent star (Nikolov et al., 2018). Independent of any formation location in the protoplanetary disc, the alkali metal ratios should not be affected significantly, as the accretion of planetesimals will enrich both (here sodium and potassium) similarly. Therefore, to make an assumption about the expected Ki excess level on HD209458b, we compare the previously detected Nai excess level on both planets assuming similar Nai/Ki–ratio.

Although the Nai excess absorption level for HD189733b is around two times larger than for HD2093458 (Snellen et al., 2008; Jensen et al., 2011), it corresponds to a similar variation in apparent planet radius (Snellen et al., 2008). Translating the Ki excess absorption of 0.184% on HD189733b to the variation in apparent planet radius, one would expect a Ki absorption of around 0.108% for HD209458b. This value is larger than our upper 3-σ limit of 0.084%, indicating that potassium could be depleted on HD209458b, either by condensation processes in the lower and/or photo-ionization processes in the upper atmosphere. Such an indication is also suggested by Sing et al. (2008b,a), who observed a broad absorption plateau at lower altitudes and a narrow absorption line core for the Nai feature. The authors argued that condensation on the night side of the planet can lead to the loss of atmospheric sodium, as the atmospheric temperatures become cool enough to condensate sodium and lead to the absence on high altitudes. This was also confirmed by Vidal-Madjar et al. (2011) showing temperature-pressure-profile simulations to match the observations by Sing et al. (2008b,a) and Snellen et al. (2008).

Comparing to those findings, the interpretation of the Ki detection is puzzling. The condensation of sodium to Na_2S as well as NaCl happens at higher temperature than the condensation of potassium to KCl (Lodders, 1999), so that one would expect potassium to be more abundant than sodium, in contrast with what is observed. An alternative depletion process is photo-ionization. Potassium has a slightly lower ionization energy than sodium, leading to easier photo-ionization of potassium (Fortney et al., 2003; Barman, 2007). Then, one may expect that depletion of potassium is stronger on HD189733b (which orbits an active star) than on HD209458b, not being in agreement with our findings, making the atmospheric conditions on HD209458b puzzling.

Although both planets have similar properties (e.g. size, orbital period and equilibrium temperature) there are deviations especially on their cloud properties (Lines et al., 2018). Modelling approaches suggest that cloud formation on HD189733b originates at lower pressure levels due to its higher gravity and cloud particle density (Lines et al., 2018) opposite to dust clouds on HD209458b, which extent to large areas on the atmosphere (Helling et al., 2016).

These differences (among others) could lead to different condensation chemistry on both targets, affecting the alkali depletion processes and thus the implications discussed above.

5 Probing the atmosphere of HD189733b with the Nai and Ki lines

5.1 Abstract

High spectral resolution transmission spectroscopy is a powerful tool to characterize exoplanet atmospheres. Especially for hot Jupiters, this technique is highly relevant, due to their high altitude absorption e.g. from resonant sodium (Nai) and potassium (Ki) lines. We resolve the atmospheric Ki-absorption on HD189733b with the aim to compare the resolved Ki-line and previously obtained high resolution Nai-D-line observations with synthetic transmission spectra. The line profiles suggest atmospheric processes leading to a line broadening of the order of ∼10 km/s for the Nai-D-lines, and only a few km/s for the Ki-line. The investigation hints that either the atmosphere of HD189733b lacks a significant amount of Ki or the alkali lines probe different atmospheric regions with different temperature, which could explain the differences we see in the resolved absorption lines.

5.2 Introduction

The characterization of exoplanets and especially their atmospheres increases our understanding of planetary formation and evolution. One possibility to characterize exoplanets is transmission spectroscopy, thus inferring the fingerprints of planetary atmospheres (Seager & Sasselov, 2000), as a part of the starlight is absorbed or scattered by atmospheric constituents during transit.

Using high-resolution spectroscopy (Snellen et al., 2010b; Cauley et al., 2019; Yan et al., 2019) one can reveal information about sharp line absorption at high altitudes. These absorptions are investigated usually using either the so called "excess absorption method", where the flux of the spectral range of interest is integrated within a bandwidth and divided by the flux within a reference band (Charbonneau et al., 2002) or the "division method", where the observations during the transit are divided by the mean of the out- of- transit observations (Wyttenbach et al., 2015), showing the spectrally resolved planetary absorption. The information inferred from the spectral lines can be used to determine different properties from the probed atmospheric region e.g. the temperature profile (Wyttenbach et al., 2015), number densities (Huang et al., 2017), escape (Fossati et al., 2018), aerosols (Pino et al., 2018a,b) or the pressure level (Gibson et al., 2020; Turner et al., 2020). Absorption lines of interest are the alkali lines Nai and the Ki with their strong absorption cross-sections (Lavvas et al., 2014), where the exoplanet HD189733b is one of the first exoplanets where atmospheric Na absorption was found (Redfield et al., 2008).
The exoplanet HD189733b has an apparent radius of $1.151 \times R_{Jup}$ and an orbital period of 2.21 days. It orbits an active K-dwarf star with an apparent magnitude of V = 7.7 mag and a radius of $0.752 \times R_{Sun}$. The first Nai detection in the atmosphere of HD189733b was presented by Redfield et al. (2008) using the High Resolution Spectrograph (HRS) instrument attached to the 9.2 m Hobby-Eberly-Telescope. A Nai excess absorption of 0.0672 ± 0.0207 % was found, as well as a blue-shift in the planetary absorption signal within the transmission spectrum. The authors speculated that this was caused by high-speed winds flowing from the hot dayside to the cooler nightside of HD189733b. This

result was confirmed by Wyttenbach et al. (2015) and Casasayas-Barris et al. (2017) using the ESO 3.6 m telescope and the High Accuracy Radial velocity Planet Searcher (HARPS) spectrograph as well as Khalafinejad et al. (2017) using the Ultraviolet and Visual Echelle Spectrograph (UVES) instrument attached to the Very Large Telescope (VLT). Several investigations attempted to detect K on HD189733b. For instance, Jensen et al. (2011) used the Hobby-Eberly-telescope, but without success. A tentative 2.5-σ detection of Ki in the atmosphere of HD189733b is shown by Pont et al. (2013) where the Advanced Camera for Surveys (ACS) instrument on-board of the Hubble Space Telescope (HST) was used for their observations. Recently, Keles et al. (2019) detected Ki with an excess level of 0.184 ± 0.022 % on HD189733b using the Large Binocular Telescope (LBT) and the Potsdam Echelle Polarimetric and Spectroscopic Instrument (PEPSI).

A particular emphasis is given to wind properties within the atmosphere of HD189733b, which are investigated in different high-resolution transit observations e.g. Louden & Wheatley (2015), Brogi et al. (2016), Salz et al. (2018) or Seidel et al. (2020). Winds on giant exoplanets can vary, e.g. being equatorial jets that originate from the lower parts of an atmosphere (around 1 bar) and stream into the direction of the planet's rotation, day-to-night-side winds which arise at higher altitudes (around 1 mbar) or atmospheric super-rotation (Brogi et al., 2016). These winds can vary from planet to planet, as different effects have an influence on their atmospheric properties e.g. a planetary magnetic field or synchronization between the atmosphere and planet interior (Brogi et al., 2016). In the case of day-to night-side winds, the line cores of resolved absorption lines show a blue-shift as the wind pushes the atmosphere into the observer's line of sight during transit. In the other cases, the absorptions arising from different positions on the observable annulus are velocity shifted regarding the projected distance to the rotation axis (largest shift on the greatest projected distance and lowest at the region where the atmosphere becomes opaque). On the trailing and leading limbs the shift is of opposite direction (Louden & Wheatley, 2015). The resulting observed final absorption line is the sum of each of these intrinsic shifted absorptions, which results in a broadened and shallower absorption line compared to an absorption line from a stagnant atmosphere. The aforementioned studies show a tentative consensus for the existence of an eastward equatorial jet in the atmosphere of HD189733b, which is consistent with modeling approaches (see Showman et al. (2012) and the references therein).

In this work, we spectrally resolve the atmospheric Ki line on HD189733b from the observation presented by Keles et al. (2019) and compare the line shape to the resolved Nai-D-lines presented by Casasayas-Barris et al. (2017). The alkali atoms Na and K are known to have very similar condensation curves as well as similar ionization potentials (Lavvas et al., 2014), leading to very similar shaped mixing ratio profiles (Lavvas & Koskinen, 2017). As the observations suggest a strong broadening of the Nai-D-lines, also recently shown by Seidel et al. (2020) and Gebek & Oza (2020), we investigate the line widths by comparing them to synthetic line profiles. We discuss the difference in the broadening of the alkali lines and their possible trigger, such as winds. The comparison between the alkali lines enables us to discuss either a scenario where the alkali lines probe the same atmospheric region which would hint on a super-solar planetary Na/K- ratio or a scenario where both features trace significantly different atmospheric regions with different temperature.

This paper is structured as follows. Section 5.3 shows the observational data and Section 5.4 the models used. The methods and results are presented in Section 6.5, where we resolve the Ki-absorption and compare both alkali lines with synthetic transmission spectra. In Section 6.6, we compare the alkali lines with each other and discuss the results. Section 6.7 presents the summary and conclusion.

5.3 Observational data

5.3.1 The Ki Observation

A transit of HD189733b was observed at the LBT with PEPSI, which is a white–pupil fiber–fed spectrograph (Strassmeier et al., 2015, 2018a,b). The observation covered the wavelength range 7340 - 9070 Å at a 4-pixel spectral resolution of 130 000. During the observation, 15 out-of-transit and 9 in-transit spectra were observed at an exposure time of 10 min. The telluric and blaze correction, as well as the image processing steps, are described in detail in Keles et al. (2019) (hereafter KEL19). The authors found a significant Ki excess absorption for bandwidths between 0.8 - 8.0 Å around the Ki-line at 7698.98 Å in their observation. We use the processed and telluric corrected dataset from KEL19 and spline them to the wavelength grid with a spacing of 0.01 Å to resolve the planetary Ki-line at 7698.98 Å. The second resonant Ki-line at 7664.92 Å is contaminated by strong telluric oxygen lines and is not investigated.

5.3.2 Nai detection by Casasayas-Barris et al. (2017)

Casasayas-Barris et al. (2017) (hereafter CSB17) presented three transit observations of HD189733b acquired with the HARPS instrument (Mayor et al., 2003) with a resolution of ∼115 000 on the ESO 3.6 m telescope (La Silla Observatory). They comprised of 99 spectra (46 being in-transit and 53 being out-of-transit) at exposure times of 5 min and 10 min. The authors find a significant Nai absorption resolved around both Nai-D-lines at 5889.906 Å and 5895.879 Å. Although the detection of the Nai-D-lines using the same data set is made first by Wyttenbach et al. (2015), we will compare the resolved Ki-line profile with the findings by CSB17, as the authors considered the effect of center-to limb-(CLV) variation (see e.g. Czesla et al., 2015; Yan et al., 2017) and the Rossiter-McLaughlin (RM) -effect (Rossiter, 1924; McLaughlin, 1924) in their investigation. For this, we use the unbinned resolved Nai-D-line profiles from CSB17 presented in their Figure 7 (top panel).

5.4 Models

5.4.1 The residual RM-feature

Due to the stellar rotation, the stellar lines become shifted in wavelength according to their position on the stellar surface, whereby the line-shifts decrease towards the stellar center. During the transit, in case of HD189733, the planetary body blocks blue-shifted light during the first part of the transit and red-shifted light during the second part of the transit hence introduces a line deformation and shift to the observed mean stellar line. This effect introduces a residual feature after dividing the in-transit spectra by the master out-of-transit spectrum, which we denote here as the "residual RM-feature".

The shape of the residual RM-feature in the transmission spectra depends strongly on the line-properties of the investigated stellar line, the star-planet geometrical properties and the stellar properties e.g. stellar rotation velocity and obliquity. This side effect introduced by the RM-effect is addressed in different investigations in the literature e.g. Louden & Wheatley (2015), Brogi et al. (2016), Chen et al. (2020) and especially in the recent work by Casasayas-Barris et al. (2020), showing the non-detection of Nai in the atmosphere of HD209458b and the importance to consider the RM-effect.

We model the residual RM-effect using a grid model, where we map the stellar surface by a grid of 100 x 100 pixels containing limb angle dependent fluxes, thus considering

also the CLV-effect (for further information on the stellar spectra we refer to section 3.3 in KEL19). To account for the stellar rotation, each spectrum is shifted according to the differential velocity on the stellar surface. During the transit, the planetary surface (mapped by 70 x 70 pixels) blocks different regions of the stellar surface, leading to the afore-mentioned effect.

5.4.2 The rotational broadening model

We model the rotational broadening of the synthetic transmission lines using a grid model, where we map the planetary surface by a grid of 100 x 100 pixels containing the synthetic lines. To account for the rotational broadening, each spectrum is shifted according to the differential velocity on the planetary surface. The planetary surface consists of the planetary body (at $1 \times R_p$) and the probed atmospheric ring, where the absorption lines originate. To compute the broadened absorption line profile, we sum over all pixels on the atmospheric ring. We define the border of the atmospheric ring at $1.285 \times R_p$ for the Nai-D2-line absorption, at $1.200 \times R_p$ for the Nai-D1-line absorption and at $1.136 \times R_p$ for the Ki-line absorption inferred according to the line contrasts of the non-broadened line profiles derived in this work (see Section 6.6). Note, that these boundaries are first order approximations. However, the choice of the boundary has a small effect on the outcome, as the line broadening is determined, mainly by the rotational velocity.
We validated our model by comparing it to the [1] PyAstronomy tool *pyasl.fastRotBroad* which introduces rotational broadening according to (Gray & Corbally, 1994) (i.e. for a stellar surface). We introduced different broadening values to synthetic line profiles, which show no significant deviations from each other for both models.

5.4.3 The Synthetic Transmission spectra

We will compare the alkali lines with line profiles from synthetic transmission spectra. The theoretical transmission spectra are calculated for different atmospheric temperatures and volume mixing ratios. The temperature is varied between 2000 - 6000 K in steps of 200 K. The volume mixing ratio for potassium is varied in the range around $\sim 10^{-9}$ -10^{-5} and the sodium volume mixing ratio in the range of $\sim 10^{-7}$ - 10^{-3} around the solar composition values, which are $\sim 10^{-6}$ for Na and $\sim 10^{-7}$ for K (Pino et al., 2018a). The atmosphere of HD189733b is well known for showing a scattering slope in the visible wavelength region that is far larger than predicted by molecular Rayleigh scattering alone (e.g. Pont et al., 2013). A well-accepted explanation for this effect is the occurrence of small aerosol particles in the upper atmosphere that contribute to the scattering optical depth in this wavelength range. We follow the work of Pino et al. (2018a) (see their equation (10)) and include this aerosol scattering via analytic approximations, which are based on the HST spectra of HD189733b. The transmission spectra are calculated with a reference pressure of 10 bar located at the measured white-light radius of HD189733b. Further details on the computation is provided in Appendix 5.8.1.
All synthetic spectra were calculated with a spacing of 0.01Å similar to the spacing of the observational data and convolved with the instrumental resolution using the PyAstronomy tool *PyAstronomy.pyasl.instrBroadGaussFast*. As the synthetic transmission spectra mirror the wavelength dependent radius (R_p) of HD189733b, we convert them via 1 -$(R_p/R_*)^2$, equivalent to the observational line profiles and normalize them with a second order polynomial fit to the continuum from 5000Å - 10000Å.

[1] https://github.com/sczesla/PyAstronomy

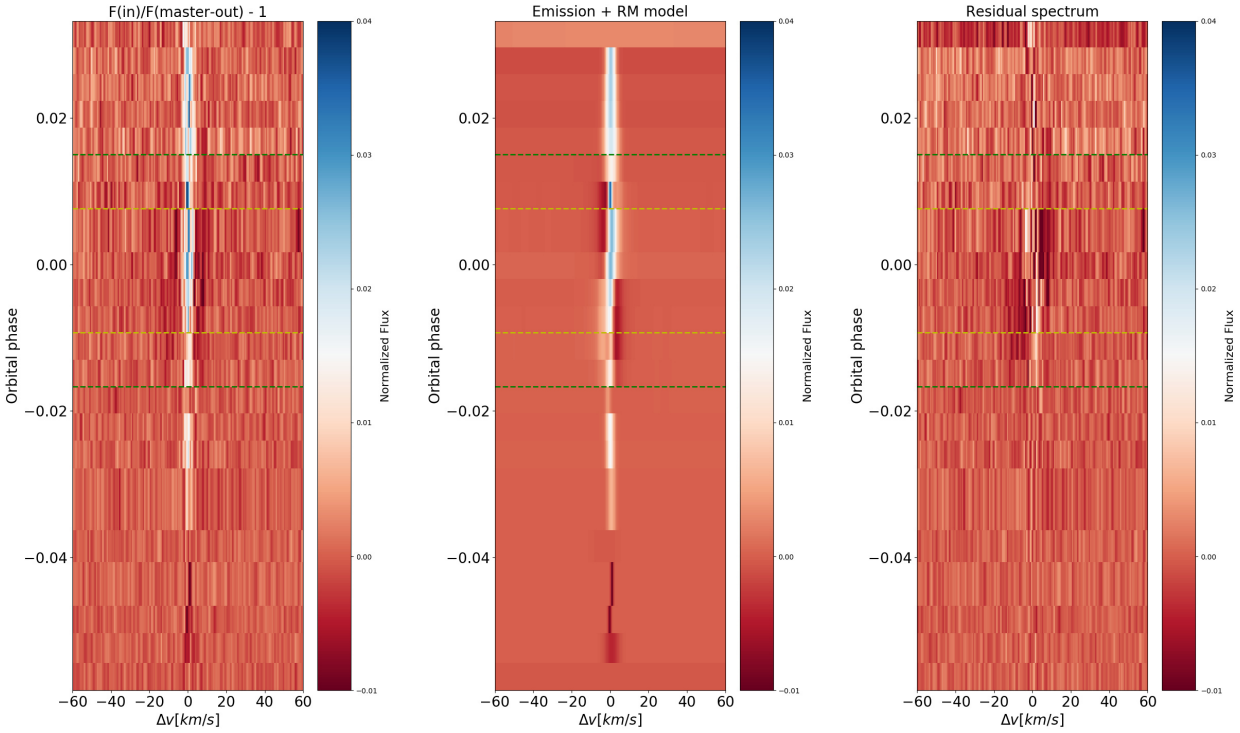

Figure 5.1: Transmission spectra around the Ki-line at 7698.98 Å (orbital phase vs. velocity shift). Left panel: The observations divided by the Master out spectrum and subtracted by unity (red). Middle panel: The residual RM-model and the fit to the emission line induced by stellar activity. Right: The residual spectrum (left panel divided by the middle panel) showing the Ki absorption (dark region). Green dashed lines mark the 1st and 4rd contact and the yellow lines the 2nd and 3rd contact.

5.5 Method and Results

5.5.1 Re-investigating the Ki-absorption on HD189733b

We aim to spectrally resolve the planetary Ki-line and compare its line shape to the Nai-D-lines presented in CSB17. Many processes can affect high-resolution transit spectra and need to be considered e.g. telluric lines (see e.g. Allart et al. (2017)), the center-to-limb variation (see e.g. Czesla et al. (2015),Yan et al. (2017)), the Rossiter-McLaughlin effect (see e.g. Cameron et al. (2010), Cegla et al. (2016), Dravins et al. (2018), Bourrier et al. (2018)) or stellar activity (see e.g. Cauley et al. (2018)). To separate the planetary Ki-absorption from the stellar line profile, one needs to derive the transmission spectrum by dividing the in-transit spectra (the observations acquired during the transit) by a master out-of-transit spectrum (the mean spectrum of the observations acquired before and after the transit). We derive the master out-of-transit spectrum using 14 out-of-transit spectra, neglecting ingress and egress observations. The planetary motion introduces a Doppler shift to the wavelength position of the planetary absorption lines. Due to this, each transmission spectrum is shifted back to the planetary rest frame and the transmission spectra co-added, demonstrating the planetary absorption. The left panel in Figure 5.1 shows the transmission spectra subtracted by unity (orbital phase vs. velocity shift). There is an emission-like feature increasing with planetary orbital phase, which is continuing also in the out-of-transit observations (visible beyond the green dashed lines which mark the 1st and 4rd contact). This is mentioned also by KEL19 and was related to stellar activity.

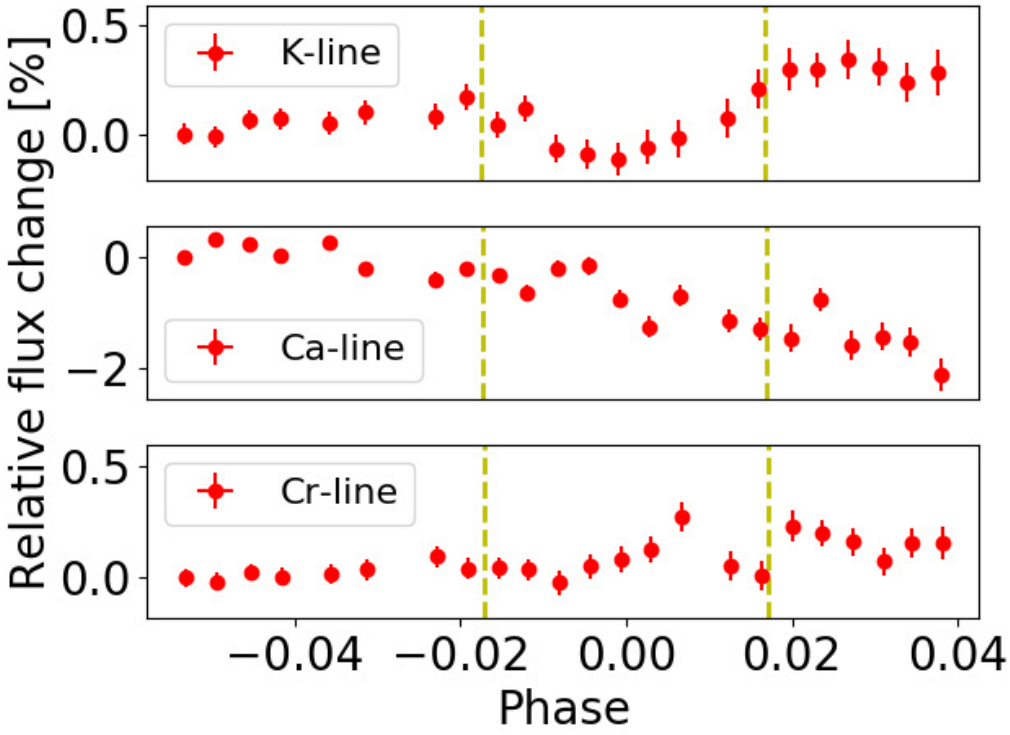

Figure 5.2: Excess absorption around a 0.5 Å bandwidth centered around the Ki-line at 7699 Å (first panel), the Caii- line at 8662 Å (second panel) and the control Cri-line at 7462 Å (third panel).

In order to investigate spurious stellar activity during the transit, Figure 5.2 shows the excess absorption around the Ki-line at 7699 Å (top), the Caii-line at 8662 Å (second panel) and the control Cri-line at 7462 Å (third panel). The excess absorption derived here is the flux integrated around the line cores within a bandwidth of 0.5 Å and normalized using a linear fit to the out-of-transit values. To show the relative flux change, the values are divided again by the value of the first observation. As mentioned by KEL19, we see a slope in the top two excess curves which can be well described by a linear fit. The Caii-IR triplet lines are known to show variations due to stellar chromospheric activity. Klocová et al. (2017) investigated a flare during one transit of HD189733b determining a change in flux of the Caii- line at 8498 Å of around 2-3 % (see their Figure 6). Comparing this to Figure 5.2, we see a decrease in flux of around 2 % in the Caii- line, showing a possible correlation with the activity. We show this correlation also for the weaker control Cri-line, which is less affected than the strong Ki-line.
To account for the emission feature and the residual RM-feature (see Section 5.4.1) in the transmission spectra shown in the left panel of Figure 5.1, we fit the emission line with a Gaussian profile using the Pyastronomy tool *funcfit* and combine it with the residual RM-feature model (middle panel in Figure 5.1). Due to the low rotation velocity of 3.3 km/s of the host star HD189733, the residual RM-feature does not move much and overlaps with the emission feature in the line core region. As the transit duration of around ∼109 min is quite short, there are only five transmission spectra available after neglecting the ingress and egress spectra, where the planetary absorption moves around ± 8 km/s corresponding to ± 0.21 Å.

The transmission spectra are subsequently corrected for the resulting model by division (right panel in Figure 5.1), showing the velocity shifted planetary absorption at different

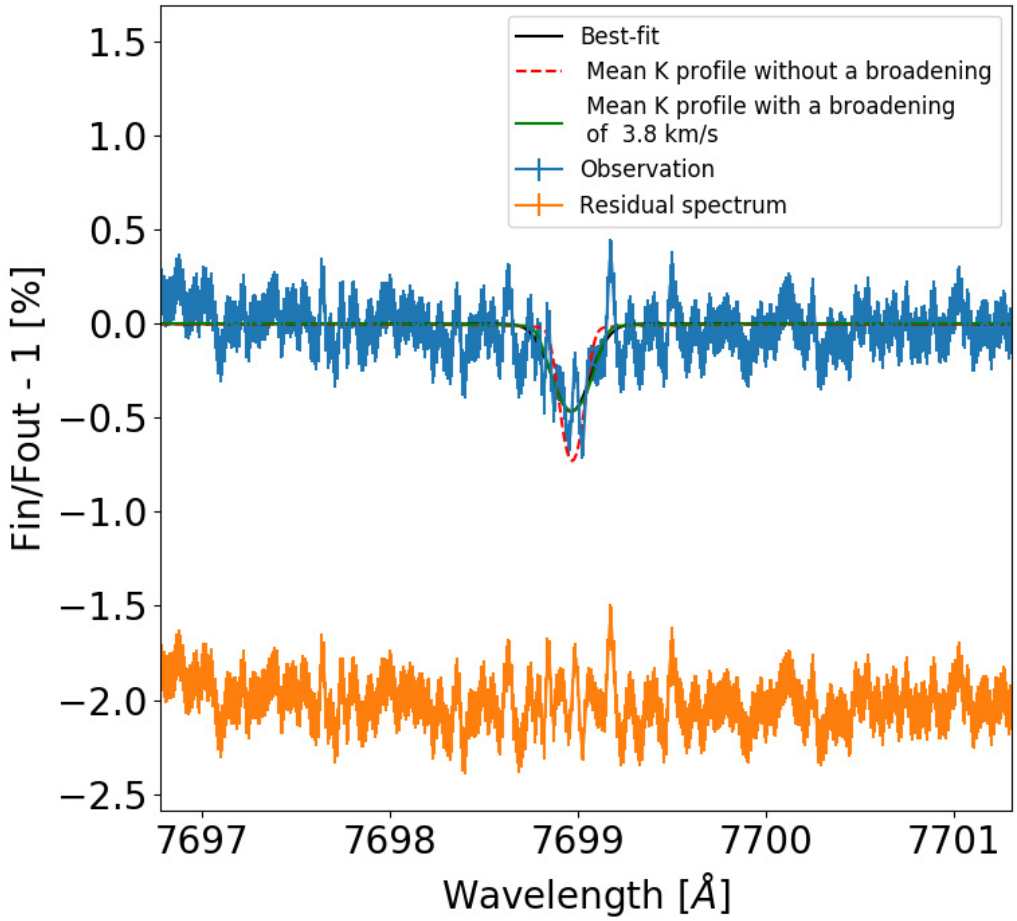

Figure 5.3: Transmission spectrum around the Ki-line at 7699 Å in [%] subtracted from unity. The black solid line shows the Gaussian fit. The dashed lines show the expected planetary absorption from the synthetic spectra without any broadening (red) and with the best-matching broadening solution of 3.8 km/s (green). The residual spectrum is shifted for clarity.

orbital phases. To derive the final planetary transmission spectrum, we shift the in-transit transmission spectra corrected by the model to the planetary rest frame and co-add them. The final transmission spectrum is shown in Figure 5.3. Applying a Gaussian fit (black solid line), we determine the FWHM $= 0.24 \pm 0.03$ Å and the LC $= 0.46 \pm 0.04$ %. The residual spectrum is shown with an offset (orange solid line), showing no correlated noise. We expect the line center at 7698.965 Å (as we removed the systemic velocity of -2.277 km/s). The line center is at 7698.966 $\pm$ 0.01 Å and shows no significant wavelength shift.

To verify our result, we calculate the Ki excess absorption from the final transmission spectrum and compare it with the results of KEL19 for different integration bandwidths. For this, we integrate the final F_{in}/F_{out} spectrum around the line core and normalize it by the number of integrated points. The excess absorption agree within their error bars up to 4.0 Å bandwidths and remain within 3-error bars for larger bandwidths. The deviations at larger bandwidths may arise due to the different techniques used to derive the excess absorption level (Casasayas-Barris et al., 2020).

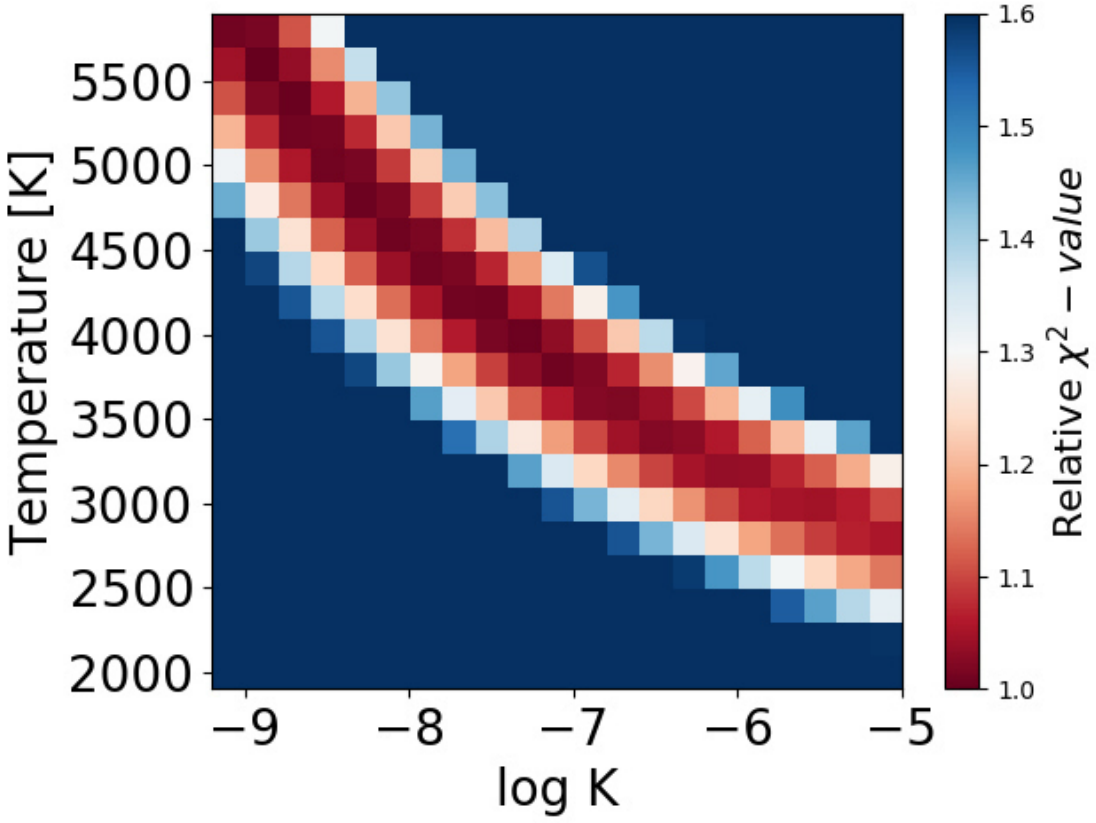

Figure 5.4: Shown is the abundance-temperature degeneracy for Ki-line. log K denotes the logarithmic volume mixing ratio of K. Reduced χ^2 values (color marked) relative to the best value compare the observational Ki-line with various synthetic line profiles. Each pixel corresponds to one comparison.

5.5.2 Comparison of the synthetic- and observational Ki-line profile

To investigate the Ki-line shape, we compare the resolved Ki-line with the line profiles from the synthetic transmission spectra. For this purpose, we calculate the reduced χ^2-value ± 0.24 Å around the Ki-line core corresponding to $\sim 2 \times$ the FWHM (in total 48 spectrally resolved data points). Before the reduced χ^2- value calculation, we introduce rotational broadening to the synthetic line profiles according to Section 5.4.2 to account for line broadening. We increase this in steps of 0.1 km/s and calculate the reduced χ^2-value repeatedly until we reach a reduced χ^2-minimum between the observational and synthetic line profiles. We do this exercise for each synthetic temperature-abundance spectrum separately.

Here, we emphasize that high resolution observations are insensitive to the atmospheric continuum and can only measure the contrast of an absorbing feature i.e. the difference between the line core and the continuum. This contrast does not change increasing (or decreasing) the abundance of a species, as the feature originates higher up (or lower down) in the atmosphere not changing its contrast (Pino et al., 2018a). In this work, the continuum (and thus the contrast) is set by the haze layer. Therefore, increasing the temperature or abundance shifts the absorption line higher up in the atmosphere which arises more and more above the haze layer and mimics an increase in absorption for higher temperature and abundance.

The comparison map between the synthetic and observed Ki line profile is shown in Figure 5.4. Each pixel corresponds to one synthetic transmission spectrum and observation

comparison. The color bar shows the reduced χ^2-minimum value relative to the best value. The characteristic shape of the color map highlights the degeneracy between the temperature and the K abundance. Increasing the temperature, the scale height increases as well and shifts the absorption to higher altitudes. Similarly, higher abundances lead to a stronger absorption signature above the haze layer which reaches higher altitudes. Thus, an absorption feature induced by an increased temperature can not be distinguished apriori by an absorption feature induced by higher abundance if the continuum is determined by a haze layer. The same scenario is valid for decreasing the temperature or abundance where the absorption is shifted to lower altitudes. Thus, increasing the temperature, synthetic spectra with lower abundances match the observations and show a lower reduced χ^2- value (and vice versa). Note, that this effect is completely degenerate with the location of the haze layer and reference pressure level. Thus, the characteristic shape will shift linearly changing these parameters, denying the determination of the "real" absolute abundance - temperature values.

However, from this grid of different temperature-abundance spectra, we are able to derive the mean synthetic Ki-line profile. For this, we determine the best matching line profile at each temperature grid on the characteristic shape (i.e. the red stripe) and calculate the mean line profile by averaging those. The mean synthetic line profile is shown in Figure 5.3 with a green dashed line, while the mean synthetic Ki-line profile prior to the broadening process is presented in a red dashed line. A rotational broadening of ∼3.8 km/s is needed further to the accounted line broadening mechanisms such as instrumental resolution and atmospheric properties (for instance temperature and pressure broadening) to match the observational line profile (excluding the planetary rotation).

5.5.3 Comparison of the synthetic- and observational Nai-D-lines

We want to compare the resolved Nai-D-lines in CSB17 (see Section 5.3.2) with the Nai-D- absorption lines produced from the synthetic transmission spectra (in the same way as done in Section 5.5.2 for the Ki-line). We compare the synthetic and observed absorption lines ±0.62 Å around the Nai-D-line cores corresponding to ∼2 × the FWHM (in total 124 spectrally resolved data points for each Nai-D-line).

Figure 5.5 shows the resulting comparison map for the Nai-D-lines (top). Similar to the Ki investigation, one can see the degeneracy for the different temperature-abundance combinations due to the haze layer. The middle panel of Figure 5.5 shows the corresponding velocity broadening map, where the color bar indicates the introduced rotational broadening in km/s (the scales are adapted for best visibility). The maps show, that the synthetic lines of interest need to be broadened around ∼8-12 km/s to match the observation for both Nai-D-lines. We derive the mean synthetic Nai-D-line profiles in the same way as done for the mean synthetic Ki-line profile. The bottom panel of Figure 5.5 shows the resolved line profiles from CSB17 (unbinned = grey solid; binned by 10 pixels for clarity = red dots) and the derived mean synthetic Nai-D-line profiles (dashed black line). The emission-peak in the line center arises due to the fact, that only broadened lines from the atmospheric ring are contributing to the final line profile, neglecting the blocked velocity shifted absorption profiles from the planetary body. For small velocities, this peak vanishes, but becomes significant for larger ones. The mean synthetic broadened line profiles match well with the observations. We also show the mean synthetic line profiles before broadening (dashed blue).

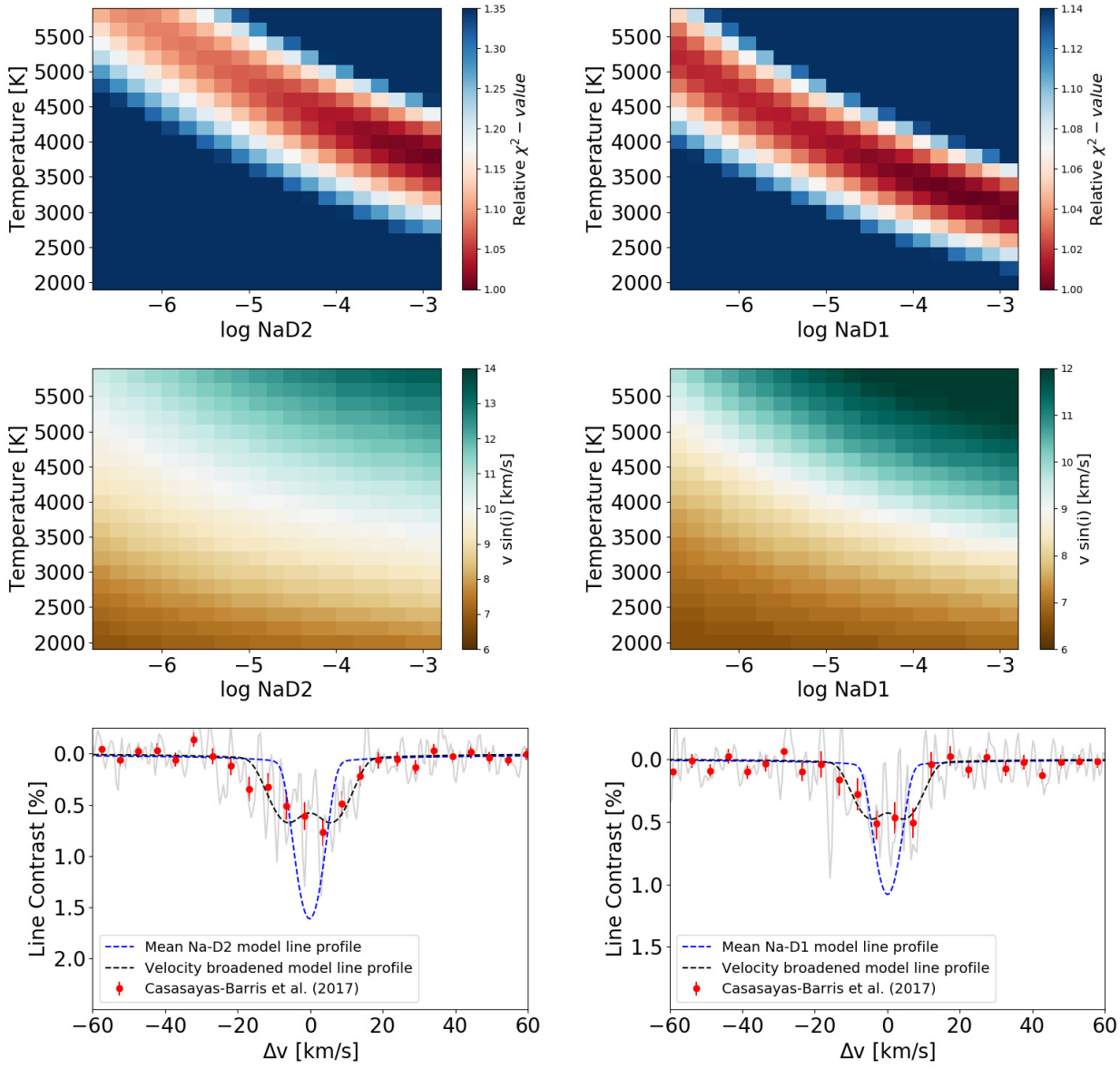

Figure 5.5: Top panel: Abundance-temperature degeneracy for Nai-D-lines, where log NaD2 and log NaD1 are the logarithmic volume mixing ratios. Reduced χ^2 values relative to the best value (color marked) compare the observational Nai-D-profiles with various synthetic spectra, whereby each pixel corresponds to one spectrum comparison. Middle panel: The introduced broadening to the synthetic spectra is shown. The color bar indicates the broadening value in km/s. Bottom panel: The line contrast over line center distance in units of velocity is shown for theNai-D2-line (left) and Nai-D1-line (right). The synthetic mean line profile with (dashed black) and without (dashed blue) introduced broadening. Red dots show the resolved planetary Nai-D-lines from Casasayas-Barris et al. (2017) (binned by 10 pixels) and grey show their unbinned data.

5.6 Discussion

We discuss the different possibilities, which could be the reason for the large difference in the line widths (around a factor of 2) for both alkali lines shown in the top panel of Figure 5.6, where we show the derived mean synthetic line profiles from this work. The comparison of the resolved Nai-D-line profiles from CSB17 with the synthetically derived ones suggests that the Nai-D-lines need to be broadened by velocities in the order of ∼10 km/s, regardless of the atmospheric temperature for the best matching synthetic line profiles, as shown in the middle panel of Figure 5.5. Applying a Gaussian fit, the line profiles show a FWHM of ∼22.9 km/s for the Nai-D2-line and ∼18.8 km/s for the Nai-D1-line. Comparing the resolved Ki-line profile (which has an FWHM of ∼9.4 km/s) with the synthetically derived mean line profile, only a broadening of around 3.8 km/s is needed, which is 2-3 times less compared to that we see for the Nai-D-lines. The resolved Nai and Ki lines were obtained with different spectrographs (HARPS and PEPSI). Both instruments are high resolution fiber-fed spectrographs which are pressure and temperature controlled and observed the alkali lines at similar resolution. The difference in line widths seems to be too large to be explained by potential systematic effects arising from the usage of different instruments. In both cases, one would expect a line broadening of around 2.7 km/s due to the planetary rotation (further to the temperature and pressure broadening introduced into the synthetic line profiles). Taking into account that the alkali lines absorb at higher altitudes around 1-1.3 R_P, this would increase the broadening around a few hundred m/s only. Furthermore, as the planet moves during the transit, the planetary absorption arises at different wavelength positions due to the Doppler-shift. At large exposure times, this introduce also a broadening to the observed line profiles regarding the orbital phase. For a 10 min exposure time, this is on the order of a few km/s (at the ingress and egress phase) and decrease down to a few hundred m/s at the mid-transit phase. The line broadening of the resolved Ki-line can be explained by the orbital motion and the fixed exposure time.

Different atomic lines are found and resolved in other hot-and ultra-hot Jupiter type planets showing different line widths e.g. on WASP-49 (Wyttenbach et al., 2017), on Wasp-76 (Seidel et al., 2019), on Wasp-33b (Yan et al., 2019), on KELT-9b (Yan & Henning, 2018; Yan et al., 2019; Hoeijmakers et al., 2019; Cauley et al., 2019; Turner et al., 2020). To the best of our knowledge, so far only Chen et al. (2020) detected another resolved Ki-line for the exoplanet WASP-52b observed with the high resolution spectrograph ESPRESSO (Echelle SPectrograph for Rocky Exoplanets and Stable Spectroscopic Observations) at the VLT. The authors show the detection of the the Nai-D-lines with a FWHM(Nai-D2) = 21.6 ± 1.8 km/s and FWHM(Nai-D1) = 11.5 ± 1.6 km/s and the Ki-D1- line with a FWHM(Ki-D1) = 13.7 ± 3.3 km/s. Even if the FWHM of the Nai-D-lines show a strong deviation to each other, their mean FWHM is comparable with the FWHM of the Ki-D1-line, opposite to that we see comparing the Ki-line with the much broader Nai-lines in our investigation. Large line widths do not have to be necessarily attributed to being broadened by e.g. winds, as also other factors determine the line broadening such as pressure- and temperature-broadening or the cross-section of the absorbing species. However, if the observed line broadening can not be explained by only accounting for these mechanisms, broadening by planetary winds can be considered as the trigger for the enhanced broadening.

An explanation for the strong broadening of the Nai-D-lines is shown by Seidel et al. (2020). The authors show that super-rotational winds, day-to night-side winds or vertical wind patterns can introduce strong broadening to the Nai-D-lines in the upper atmosphere of HD189733b. The authors propose a possible scenario, where a planetary magnetic field in the order of 50G propels Na^+-ions via the Lorenz force from a super-rotational jet in the lower atmosphere up to the upper atmosphere, which recombines there to neutral Na

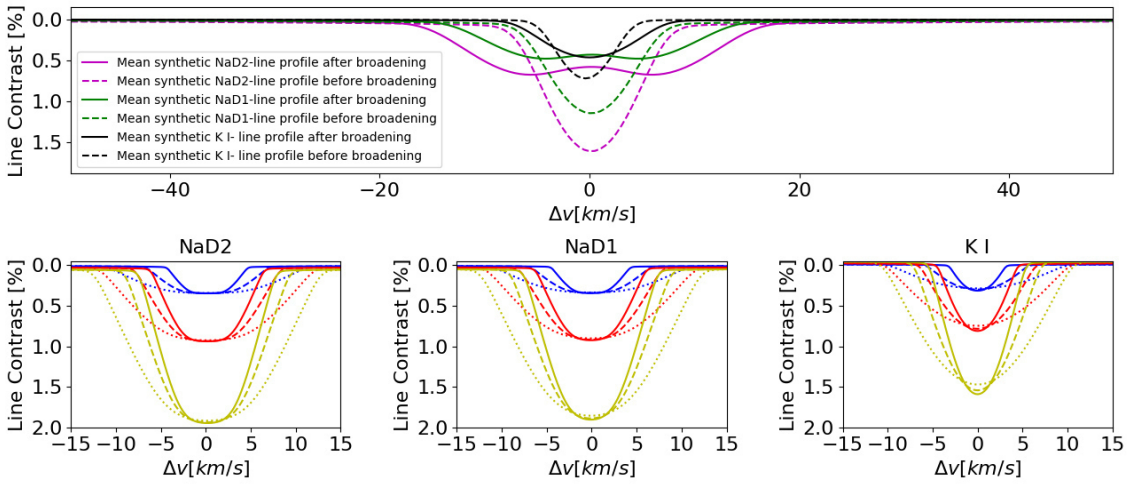

Figure 5.6: Top panel: Comparison of the mean synthetic Nai-D-lines and the Ki-line from this work. Dashed lines show line profiles before and solid lines after introduced rotational broadening. Bottom panel: Nai-D-lines and Ki-line modelled for isothermal temperature and solar abundance value at 2000K (blue), 4000K (red) and 6000K (yellow) for turbulence velocities of v_t of 1 km/s (solid), 10 km/s (dashed) and 20 km/s (dotted). The x-axis shows the distance to the line center in km/s.

at the same speed.

Another explanation for the large broadening may be turbulences in the planetary atmosphere. In contrast to the introduced rotational broadening, turbulences would lead to a line broadening by an intrinsic change of the Doppler-width which can be described by:

$$\sigma_{\mathrm{D}} = \frac{\nu_0}{c}\sqrt{\frac{k_{\mathrm{B}}T}{m} + v_t^2}\ , \tag{5.1}$$

The bottom panel in Figure 5.6 shows the effect of turbulent velocities v_t on the Nai-D-lines and the Ki line modelled for solar Na and K abundance value (at a isothermal temperature of 2000K, 4000K and 6000K for v_t of 1 km/s, 10 km/s and 20 km/s). Introducing rotational broadening, the corresponding equivalent width of the absorption lines remain conserved, thus deeper lines become broader but shallower. On the other hand, regarding turbulences, this is not the case and the equivalent widths are not conserved. High turbulent velocities flatten the line profiles in the line core region and introduce a characteristic shape, especially at lower temperatures. But also in the case of turbulences, one would expect similar broadening effects for both alkali lines if the turbulences are not variable. Note, that a mix of rotational broadening and turbulences may be possible. In this case, the observed line widths would be affected by the degeneracy between rotational broadening, temperature and turbulences, making the investigation even more complex.

In two recent works, Seidel et al. (2020) and Gebek & Oza (2020) investigate also the broadened Nai-D-lines on HD189733b increasing the Doppler-width of the lines. Both authors derive velocities even larger than presented in this study for the Nai-D-lines. However, a direct comparison of the wind velocities is not possible as the winds are introduced in a different way (Doppler width broadening vs. rotational broadening). Changing the Doppler-width (i.e. using Equation 1), the absorption profile changes as a result of the different velocity distribution of the absorbing Na- atoms, where v_t can be also denoted as the microturbulence. On the other way, in case of rotational broadening, the Na atoms in each atmospheric column (in the line of sight) move as a unit and produce an

absorption profile which is velocity shifted with respect to the distance to the rotational axis. The final absorption profile is then the sum of all velocity shifted line profiles on the atmospheric ring. However, the results are similar in a qualitative way, stating that the Nai-D-lines may experience strong broadening on HD189733b.

However, we emphasize if the broadening of the lines arises from winds or turbulences in the order ∼10 km/s and higher, this would hint on wind velocities larger than the sound speed. But as the atmospheric region where the Nai and Ki lines form is below the exobase and thus collisionally dominated, supersonic winds are not possible. Therefore, the inferred velocities should be considered cautiously and rather qualitatively hinting on some broadening mechanisms in the upper atmosphere than quantitatively.

In general, both alkali features were expected to show very similar mixing ratio profiles and to probe similar pressure levels (see Figure 7 & 12 in Lavvas & Koskinen (2017)) for HD189733b, thus one could expect similar line broadening. But comparing the absorption level (at similar bandwidths) for Nai shown by Wyttenbach et al. (2015) and Ki shown by KEL19, Nai probes ∼27 scale heights and so much higher altitudes compared to Ki which probes ∼13 scale heights, deviating a factor of ∼2 (assuming that the same temperature region is probed). A roughly similar result is inferred comparing the LC of the non-broadened alkali line profiles shown in the top panel of Figure 5.6. Hence, Na seems to probe higher altitudes compared to K. However, if Na probes higher temperature around $T_{Na} \sim 2 \times T_K$ (and therefore higher altitude level), the noted difference in scale heights would be in agreement with the expectations. As the atomic mass of K is ∼1.7 times larger than the atomic mass of Na, the Na atoms may be lifted into the upper atmosphere by hydrodynamic motion more easily than K atoms, explaining the difference in altitude. However, advanced modelling effort would be needed to proof this which is out of the scope of this work.

If the Nai absorption probes much higher altitudes compared to the Ki absorption, this could indicate that some mechanism is leading to a broadening to the absorption lines with decreasing pressure level on HD189733b. This is also suggested comparing the Ki-absorption to other high resolution investigations regarding wind properties. In case of day-to night-side winds, the largest blue-shifts are found for the lightest elements which probe the lowest pressure regimes such as He-I (Salz et al., 2018) (-3.5 ± 0.4 km/s at the mid-transit) up to the evaporating regime probed by the Ly-α line (Lecavelier des Etangs et al., 2012), where probably evaporation plays also a significant role on such a shift. We find no significant blue-shift of the resolved Ki-line, where we deduce a shift of 0.001 ±0.01 Å (∼ 0.04 ± 0.4 km/s). However, this can not exclude the presence of a day-to night-side wind on HD189733b. This value is similar within 2σ to the findings by Louden & Wheatley (2015), who found a velocity shift of $-1.9^{+0.7}_{-0.6}$ km/s investigating the Nai-D-lines. Brogi et al. (2016) used the CRIRES (CRyogenic high-resolution InfraRed Echelle Spectrograph) instrument at the VLT to investigate the different molecular absorption features around 2.3 μm during the transit of HD189733b. The authors also probe a lower day-to-night side wind of $-1.7^{+1.1}_{-1.2}$ km/s, which is also consistent within 2σ with our finding. In case of rotational broadening, Brogi et al. (2016) state a rotational velocity of $v_{rot} = 3.4^{+1.3}_{-2.1}$ km/s, which would be in agreement within 1σ with the broadening value needed for the Ki-line of ∼3.8 km/s. The results of Brogi et al. (2016) have been confirmed by Flowers et al. (2019) analyzing the same dataset applying 3D GCM (general circulation model) simulations, also being in agreement with our broadening values in sense of wind speed (see their Table 1) and blueshift-values. As the molecular lines originate at lower altitudes compared to the alkali-lines, this appears to be consistent with the fact that some mechanism is producing significant line broadening at low pressure levels. Comparing the widths of the Nai-D-lines with the Hα-line (Cauley et al., 2016), both features probe similar altitudes and show similar large widths (Huang et al., 2017), strengthening this

picture.

Recently, Gebek & Oza (2020) compared the observational Nai-D-lines shown by Wyttenbach et al. (2015) for HD189733b with synthetic transmission spectra computed for different scenarios such as a hydrostatic atmosphere and three evaporative scenarios being an escaping atmosphere, an outgassed cloud sourced by an exomoon and a torus representing circumplanetary material, showing a strong evidence that these lines probe optically thin regions in the atmosphere. Comparing the K-absorption by Keles et al. (2019) with their scenarios, the best match is given by a hydrostatic scenario probing an optically thick region. The authors note, that their optically thin scenarios are very sensitive to the planetary Na/K ratio, which can vary if this differs from the stellar one. We aim to probe the planetary Na/K ratio and compare this to the stellar Na/K abundance ratio, which we derive in Appendix 5.8.3. The inferred stellar Na/K abundance ratio is log(Na/K) = ∼1.2 similar to the solar value (Asplund et al., 2009). Although the exoplanet could have undergone evolutionary processes changing its Na/K ratio, we expect a similar Na/K ratio for HD189733b which seems to be an appropriate assumption in the first order (Lavvas et al., 2014). Note, that due to the extinction by Earth's atmosphere, high-resolution transit observations are typically not suitable to determine absolute abundances of atmospheric constituents. The continuum information usually gets lost due to re-normalization of the spectra and becomes degenerate with the reference pressure level and transit radius (Benneke & Seager, 2012; Heng & Kitzmann, 2017; Welbanks & Madhusudhan, 2019), whereby under certain circumstances the degeneracies can be broken (see e.g. Benneke & Seager (2012), Fisher & Heng (2018), Brogi & Line (2019) or Welbanks & Madhusudhan (2019)). However, the degeneracies cancel out (for the model assumptions used in this work) deriving the ratio of the abundances, such as the Na/K ratio, unless the temperature at which the lines form is different. We roughly estimate the Na/K ratio by comparing the upper panel of Figure 5.4 and Figure 5.5 assuming that both features arise at the same atmospheric temperature and use the abundance value for the best matching model (i.e. the model with the lowest reduced χ^2 value). For the temperature range of 3400K - 5000K, we infer a planetary $\overline{Nai}/Ki$ ratio which is ∼ 20 - 400 times higher than the stellar Na/K abundance ratio. Note, that if Na originates at higher temperature than K, the planetary Na/K abundance ratio will decrease to a lower level, down to the solar Na/K abundance value.

We emphasize here that the roughly estimated Na/K values should be considered only as a hint that the alkali lines may probe different atmospheric temperature regions, as the inferred Na/K ratio has large uncertainties and relies on different assumptions (which we present in Appendix 5.8.2). Furthermore, such an increased abundance ratio seems to be unlikely to be present either in the protoplanetary disk or the atmosphere of the planet taking into account primordial elemental abundances and alkali chemistry as discussed for the hot Jupiter HD209458b in Lavvas et al. (2014), which also orbits a solar metallicity star. Furthermore, a strong variation in the alkali abundances due to depletion by e.g. by ionization processes as well as condensation processes seems to be unreasonable. Condensation for K and Na would be expected below an atmospheric temperature of 1000 K for both species in a very similar way (Lavvas & Koskinen, 2017), where both alkalis can condense into various different solids and liquids. Likely candidates (see e.g. (Marley et al., 2013)) are sodium sulfide (Na2S) and potassium chloride (KCl). The former condenses around 900 K in a solar metallicity atmosphere at 0.1 bar, while the latter requires slightly lower temperatures (about 720 K). For a extended presentation of alkali chemistry we refer here to Lavvas et al. (2014). In the case of photo-ionization, K (∼4.34 eV) has only slightly lower ionization potential than Na (∼5.14 eV) (Fortney et al., 2003; Barman, 2007), making also this process unlikely to be the reason for such a difference.

5.7 Summary & Conclusion

We compared previously observed high resolution Nai (Casasayas-Barris et al., 2017) and Ki (Keles et al., 2019) absorption in the atmosphere of HD189733b with synthetic transmission spectra modeled for a variety of temperature and abundance values. The comparison of the Nai-D-lines shows that the observed Nai-D-line widths are much larger than the modeled ones. The Nai-D-lines have to be broadened by velocities in the order of ∼10 km/s to match the observations if only rotational broadening is taken into account. To compare the Ki-line with the synthetic transmission spectra, we used the previous high-resolution observation by KEL19 and resolved the Ki-absorption from the data. The Ki-line profile shows a broadening comparable with the modeled synthetic line profiles, which is significantly less in comparison to the Nai-D-lines. Comparing to different investigations, there is a hint that the line widths show stronger broadening with increasing altitude: Starting from molecular absorption signature from the lower atmosphere showing weak or even no significant broadening effects (Brogi et al., 2016), up to the slightly larger broadened Ki-line (this work) and even to higher altitudes where the Nai-D-lines (Wyttenbach et al., 2015; Louden & Wheatley, 2015; Barnes et al., 2016; Casasayas-Barris et al., 2017; Borsa & Zannoni, 2018; Seidel et al., 2020) and the Hα-line (Cauley et al., 2016) show very large broadening. The same picture is drawn comparing the wavelength shifts introduced by a probably day-to night-side wind, which shows stronger blue-shifts for the lines emerging at lower pressure levels. This hints that the main Ki-absorption may arise from lower altitudes than the Nai-absorption. Estimating the planetary Na/K ratio and comparing this to the derived stellar Na/K ratio, HD189733b would possess a very high super-solar atmospheric Na/K ratio if Na and K trace the same atmospheric temperature for the model assumptions used in this work. However, the derived Na/K ratio depends on several assumptions and is such enhanced, that this scenario seems to be very unlikely. In case that K traces lower altitudes at a cooler temperature compared to Na, the planetary Na/K ratio can coincide with the stellar Na/K ratio being in agreement with other studies such as (Welbanks et al., 2019), which seems to be a more likely scenario.

Another high resolution and high S/N transit observation, which covers the wavelength range of different atomic and molecular species, would be needed to compare the broadening mechanisms to avoid artifacts attributed to the stellar activity, different instrumentation or even variable weather conditions on the exoplanet.

5.8 Appendix

5.8.1 Synthetic Transmission spectra

We compute theoretical transmission spectra by calculating the effective tangent height and the wavelength-dependent, apparent planetary radius with the `Helios-o` model as described in Bower et al. (2019a) or Gaidos et al. (2017a). The isothermal atmosphere is divided equidistantly in log(P) into 200 layers from 10 bar to 10^{-10} bar. The spectra are computed at a constant resolution of 0.01 cm^{-1} in the wavenumber range between 10,000 cm^{-1} and 20,000 cm^{-1}.

The opacity sources that are included in the calculations are the collision-induced absorption of H_2-H_2 and H_2-He pairs, the D_1 and D_2 resonance lines of Ki and Nai, and molecular Rayleigh scattering of H_2 and He. The line strengths S for the Nai and Ki resonance lines are obtained via

$$S = \frac{g_2 A_{21}}{8\pi\nu_0^2 Q} \exp\left(-\frac{E_1}{k_B T}\right)\left[1 - \exp\left(-\frac{hc\nu_0}{k_B T}\right)\right] , \tag{5.2}$$

where g_2 is the statistical weight of the upper level, A_{21} the Einstein A-coefficient, ν_0 the wavenumber of the transition, E_1 the energy of the lower level, Q the partition function, and T the temperature. The values for g_2 and A_{21} are taken from Draine (2011), while E_1 is zero because the resonance lines are ground-level transitions. The line profile is modeled by a Voigt profile, consisting of a Doppler core and Lorentzian line wings, where the standard deviation of the Doppler profile σ_{D} is given by

$$\sigma_{\mathrm{D}} = \frac{\nu_0}{c}\sqrt{\frac{k_{\mathrm{B}}T}{m}} \ , \tag{5.3}$$

with the molecular mass of the species m. The Nai and Ki resonance lines are well known for possessing a far-wing line profile that is non-Lorentzian (e.g. Burrows & Volobuyev, 2003; Allard et al., 2016). We approximate this behavior by using the analytic fits to the Burrows & Volobuyev (2003) line profiles according to Baudino et al. (2015). We note, however, that because of the strong aerosol scattering slope, the far wings of these lines are practically invisible and only the thermally-broadened Doppler cores are located above the spectrum's continuum level.

5.8.2 Cautions on the estimated planetary Na/K abundance ratio

The estimated planetary Na/K abundance ratio in this work is based on different assumptions, which will be discussed here. The temperature distribution at the terminator may not be constant as expected from the isothermal profiles, thus it can affect the abundance ratio, as the line cores form at a much higher temperature than the line wings (Huang et al., 2017). We estimate the Na/K ratio from the Figure 5.4 and Figure 5.5, where we introduced rotational broadening. If the line broadening is a result of turbulences, the equivalent width of the absorption lines is not conserved, thus the line widths will be larger without an increase in line depth, which will lead to overestimation of the Na/K abundance ratio. Furthermore, the synthetic line profiles depend on the functional form of the continuum which is determined by the aerosol layer. Changing the functional form of the continuum will also affect the results presented here. For instance, Welbanks et al. (2019) derived the atmospheric abundances of Na and K for several planets and compared them to those of their host stars. In this study, the authors investigated also the planet HD189733b using HST data acquired with the STIS instrument as presented by Sing et al. (2016). The authors infer similar stellar and planetary Na and K abundances based on their retrieval analysis of these data. However, inspecting panel 15 on their Figure 2, the retrieval results are based only on 2 data points around the Ki-line, resulting probably in a debatable conclusion. However, as the derived planetary Na/K abundance ratio is much larger than what would be expected, we only state the estimated super-solar Na/K ratio on HD189733b as a hint that Na and K may originate at different atmospheric regimes, as the aforementioned effects have a strong impact on the result, similar to non-LTE effects, which could also play a role. Note that high resolution observations are not always described well by simple theoretical models (such as the one employed here) and mismatches between observational and modelled line profiles can be found e.g. in Hoeijmakers et al. (2018) and Hoeijmakers et al. (2019). While in those studies, the Fe lines match extremely well with the theoretical predictions, the Fe^+ measurements, on the other hand, deviate by quite a large degree. It is obvious, that the theoretical models lack some of the physics to describe the spectral lines or the chemical abundances in the very high atmosphere properly.

5.8.3 The stellar Na and K abundance ratio

The metallicity of HD 189733 is known to be roughly solar, according to previously published investigations, and so is its Na abundance, e.g. [Na/H]=-0.04 ± 0.06, [Fe/H]=-0.10 ± 0.03 (Montes et al., 2018). However, even if the Na/K abundance ratio of HD189733 is expected to be solar (Welbanks & Madhusudhan, 2019), we could not find similar abundance information about K. We decided therefore to derive an estimate of the stellar K abundance based on the available PEPSI spectrum. For this purpose, we selected the clean Ki-line at 7699 Å and compared its profile with synthetic spectra computed for a set of different K abundances, $A(\mathrm{K})$[2], between 4.5 and 5.5, centered on the solar abundance of $A(\mathrm{K})=5.03 \pm 0.09$ (Asplund et al., 2009). The comparison is shown in the bottom panel of Figure 5.7.

The spectrum synthesis is based on a standard 1D model atmosphere taken from the MARCS grid (Gustafsson et al., 2008) with parameters $T_{\mathrm{eff}} = 5000\,\mathrm{K}$, $\log g = 4.5$, [Fe/H]=0.0, and $\xi_{\mathrm{micro}} = 1.0\,\mathrm{km/s}$, which represents HD 189733 reasonably well (cf. stellar parameters compiled by Southworth, 2010). This model atmosphere was then used by the line formation code Turbospectrum[3] (Plez, 2012) that generates synthetic line profiles for a given set of atomic parameters characterizing the spectral line in question. The atomic line data were taken from the VALD3 database[4] (Ryabchikova et al., 2015, and updates), including updated pressure broadening constants.

Comparing observed and synthetic line profiles, we notice that the line cores of the synthetic spectra are too shallow. This presumably indicates that the assumption of LTE (Local Thermodynamic Equilibrium) is not a valid approximation in the core of this rather strong Ki-line (line depth $d > 0.8$). However, we may assume that the wings of the line, where $d < 0.2$, form in LTE conditions and can be used to estimate the K abundance from a comparison with the synthetic LTE spectra. The best match of the wings is found for $A(\mathrm{K})=5.1 \pm 0.1$. This result is fully consistent with the expectation that HD 189733 has a solar K abundance. As a sanity check, we have performed the same exercise with the Na-line at 8194 Å. The comparison is shown in the top panel of Figure 5.7. Also, in this case, the observed line core is much deeper than the model results, for the same reason responsible for the mismatch in the Ki-line discussed above. Fitting the line wings, we deduce $A(\mathrm{Na})=6.2 \pm 0.1$, which is fully consistent with the solar photospheric abundance of $A(\mathrm{Na})=6.24 \pm 0.04$ (Asplund et al., 2009). We conclude that the stellar Na/K abundance ratio is indistinguishable from solar, $N(\mathrm{Na})/N(\mathrm{K}) \approx 16$.

[2] $A(\mathrm{X})= \log(N(\mathrm{X})/N(\mathrm{H}))+12$
[3] ttps://github.com/bertrandplez/Turbospectrum2019
[4] http://vald.astro.uu.se/

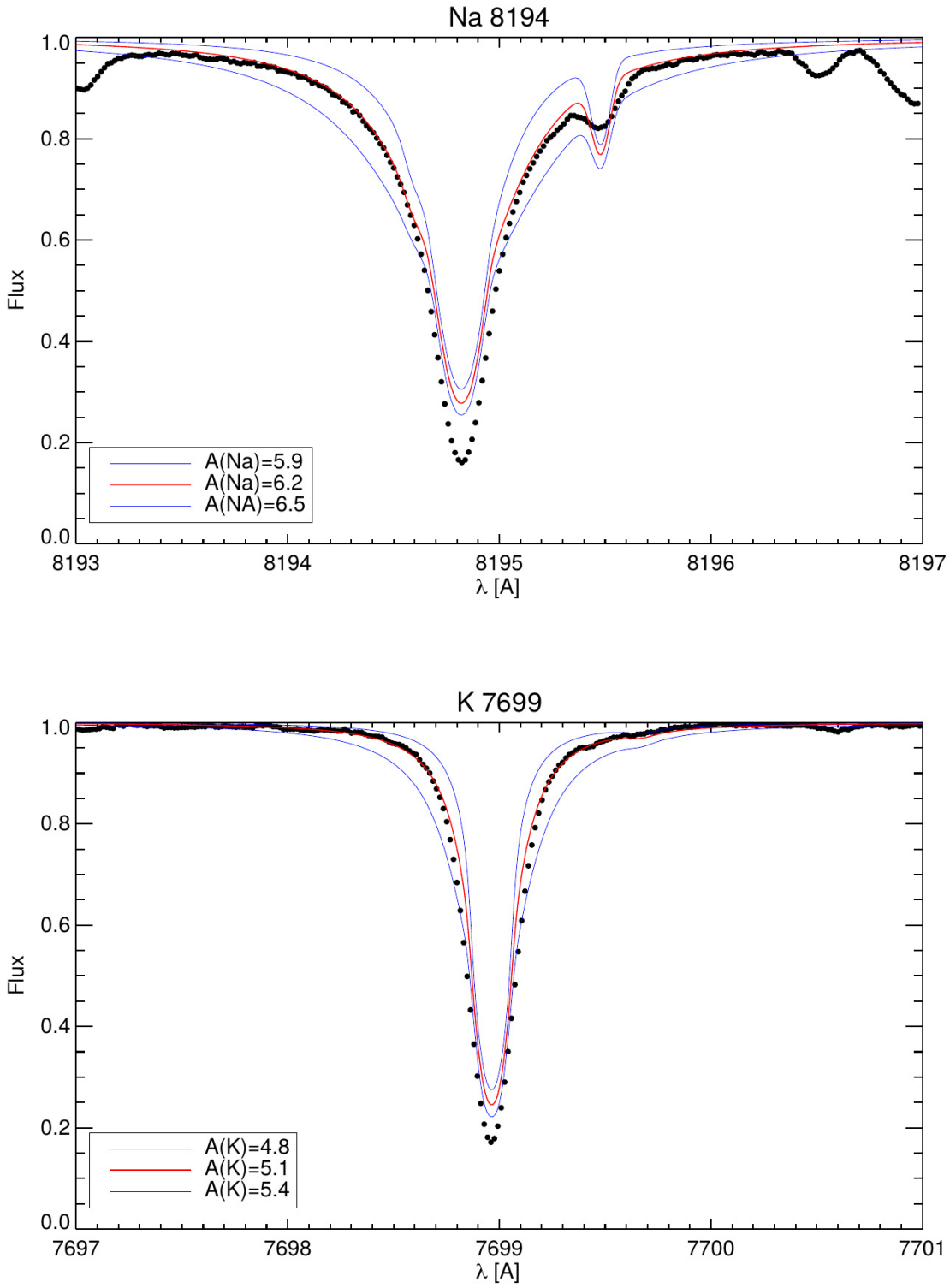

Figure 5.7: Comparison of Na-line at 8195 Å (top) and the 7699 Å Ki-line (bottom) from PEPSI spectra with the spectrum synthesis model based on a standard 1D model atmosphere. "A" denotes the logarithmic abundance value.

6 Spectral signature of atmospheric winds in high resolution transit observations

6.1 Abstract

The study of exoplanet atmospheres showed large diversity compared to the planets in our solar system. Especially Jupiter type exoplanets orbiting their host star in close orbits, the so-called hot and ultra-hot Jupiters, have been studied in detail due to their enhanced atmospheric signature. Due to their tidally locked status, the temperature difference between the day- and nightside triggers atmospheric winds which can lead to various fingerprints in the observations. Spatially resolved absorption lines during transit such as sodium (Na) could be a good tracer for such winds. Different works resolved the Nai- absorption lines on different exoplanets which show different line widths. Assuming that this could be attributed to such zonal jet streams, this work models the effect of such winds on synthetic absorption lines. For this, transiting Jupiter type planets with rotational velocities similar to hot and ultra-hot Jupiter are considered. The investigation shows that high wind velocities could reproduce the broadening of Nai-line profiles inferred in different high-resolution transit observations. There is a tendency that the broadening values decrease for planets with lower equilibrium temperature. This could be explained by atmospheric drag induced by the ionization of alkali lines which slow down the zonal jet streams, favoring their existence on hot Jupiter rather than ultra-hot Jupiter.

6.2 Introduction

The last decades showed the existence of Jupiter like giant planets in very close orbits to their host stars. Although being comparable in size and mass with Jupiter, the extrasolar hot and ultra hot Jupiter type planets are exposed by strong stellar radiation, leading to much different atmospheric dynamics (and therefore atmospheric fingerprints) compared to Jupiter in our solar systems. Due to the expected tidally locked status of these planets where the rotation and orbital periods become equal, the planetary hemispheres separate into a permanent night- and a dayside making these atmospheres more turbulent compared to Jupiter with temperature contrasts of 500K - 1000K (Knutson et al., 2008) depending on the vertical atmospheric advection and radiation timescales (Heng & Showman, 2015). The energy budget of the planetary atmosphere becomes dominated by the intense radiation, where the differential heating of the atmosphere induces pressure gradient forces resulting in atmospheric motions i.e. winds (Dobbs-Dixon et al. (2010); Perna et al. (2010); Heng & Showman (2015)). The wind speeds are a result of a balance between the atmospheric kinetic energy and the sustained friction within the atmosphere. Coming across, although tidally locked, the planetary rotational velocities can still be large especially for ultra hot Jupiter (UHJ) type planets (e.g. $\sim$6.6 km/s for KELT-9b or $\sim$7 km/s for WASP-33b) leading to the combination of both. The redistribution of energy in planetary atmospheres triggering the atmospheric circulations is a complex issue where the radiative transfer and atmospheric dynamics is addressed in different 3D modeling approaches see e.g. Showman et al. (2008), Dobbs-Dixon et al. (2010), Lian & Showman (2010), Perna et al. (2010), Showman & Polvani (2011), Miller-Ricci Kempton & Rauscher (2012), Showman et al.

(2012), Kempton et al. (2014), Zhang et al. (2017), Flowers et al. (2019), Steinrueck et al. (2019) or Debrecht et al. (2020). For hot Jupiter (HJ) type planets, these studies show two main outcomes related with atmospheric winds, being an equatorial super-rotating jet around 1 bar pressure moving into the direction of planetary rotation with wind velocities around a few km/s (Showman et al., 2008; Showman & Polvani, 2011; Showman et al., 2012) and the existence of day-to-nightside winds with velocities on the order of 1 - 10 km/s at mbar pressure regime (Miller-Ricci Kempton & Rauscher, 2012). In the case of the day-to-nightside winds, the winds become stronger for larger day-to-nightside temperature contrasts, pushing the atmosphere into the nightside direction (Showman et al., 2012). Note, that the wind velocities and directions depend strongly on the frictional drag within the atmosphere (see for instance Figure 3 in Miller-Ricci Kempton & Rauscher (2012)) and can show timely variable conditions (Komacek & Showman, 2019). For instance, one kind of friction is induced by the planetary magnetic field which tends to reduce wind velocities of weakly ionized winds by magnetic drag, as the thermally ionized particles interact with this field (Perna et al., 2010).

That atmospheric dynamics can cause signals in transmission spectra by acting on the absorption profiles from the planetary atmosphere is known for decades and comprehensively discussed in detail in e.g. Brown (2001), but also in combination with high resolution observations in very recent studies such as Seidel et al. (2020) and Cauley et al. (2020). Several works investigated and/or showed wind properties for transiting exoplanets using observations and modeling approaches e.g. Spiegel et al. (2007), Snellen et al. (2010b), Miller-Ricci Kempton & Rauscher (2012), Showman et al. (2012), Kempton et al. (2014), Wyttenbach et al. (2015), Louden & Wheatley (2015), Brogi et al. (2016), Flowers et al. (2019), Seidel et al. (2019), Casasayas-Barris et al. (2019), Cauley et al. (2019), Seidel et al. (2020), Gebek & Oza (2020), Keles et al. (2020), Ehrenreich et al. (2020), Cauley et al. (2020) and more. Two categories seem to be of main interest for the majority of the studies investigating atomic and molecular lines: On the one side, the investigation of day-to-nightside winds by searching for the blueshift of spectral lines, where it is expected that most irradiated planets should show the strongest blueshifts (Miller-Ricci Kempton & Rauscher, 2012; Showman et al., 2012). On the other side, the effect of atmospheric circulation on spectral lines, mainly sodium (Na) for the atomic lines and carbon monoxide for the molecular lines, which result in line deformation mostly due to line broadening.

One reason to use the Nai- absorption lines as tracer for atmospheric circulation is due to its strong atmospheric opacity on HJ type planets leading to strong absorption signature. In recent years, several authors resolved Nai lines on exoplanets in high resolution observations e.g. on HD189733b (Wyttenbach et al., 2015), on WASP-69b (Casasayas-Barris et al., 2017), on WASP-49b (Wyttenbach et al., 2017), on KELT-20b (Casasayas-Barris et al., 2019), on WASP-17b (Khalafinejad et al., 2018), on WASP-76b (Seidel et al., 2019), on WASP-127b (Žák et al., 2019) and on WASP-52b (Chen et al., 2020), whereas in several cases the Nai-lines show blueshifts due to day-to-nightside winds and very large full width at half maximum (FWHM) values, the latter hinting that some mechanism seems to broaden these lines.

This work aims to investigate the effect of super-rotating atmospheres with different wind patterns on Nai absorption line profiles on Jupiter type planets inferred during a planetary transit. The most comparable study to this work is shown by Spiegel et al. (2007), who investigated the effect of planetary rotation on the Nai-lines in transmission spectra for the HJ HD209458b, giving a nice overview of the different dynamical stellar and planetary effects affecting the transmission spectra. However, this work concentrates only on planetary rotation neglecting other kinds of atmospheric motion in contrast to that is presented in this work. Note, that although Nai-D2 line deformation is investigated, the effect is similar also for other spectral lines which can be resolved in planetary atmospheres

such as magnesium (see e.g. Cauley et al. (2019)), calcium (see e.g. Yan et al. (2019)), iron (see e.g. Casasayas-Barris et al. (2019)), potassium (see e.g. Chen et al. (2020)) and more. For lighter elements probing very high altitudes resolved in planetary atmospheres such as Hydrogen (see e.g. Jensen et al. (2018)) or Helium (see e.g. Nortmann et al. (2018)) evaporative winds may play another significant role (Salz et al., 2016, 2018) as well as line broadening further induced by large number densities which lead to optically thick absorption layers (Huang et al., 2017; Wyttenbach et al., 2020).

This paper is structured as follows. In Section 6.3 the model used is described. Section 6.4 explains the methodology of this paper. The results are presented in Section 6.5. Section 6.6 discuss the results and caveats of the application and Section 6.7 presents the summary.

6.3 Model

The effect of a rotating atmosphere on synthetic absorption lines is modelled using a grid model that maps the planetary surface by 200 x 200 pixels assuming that the planet´s spin axis is perpendicular to its orbital plane which is in line-of-sight. Each pixel on the spherically symmetric atmosphere contains the atmospheric Nai-D2 absorption line profile from Keles et al. (2020) for the exoplanet HD189733b to make the investigation more applicable to observational findings. The authors compared synthetic transmission spectra with the resolved Nai- lines observed by Casasayas-Barris et al. (2017) for this exoplanet and derived the unbroadened Nai-D2 line profile (see Gaidos et al. (2017b); Bower et al. (2019b); Keles et al. (2020) for further details on the synthetic line modelling approach). The right panel in Figure 6.1 shows the Nai-D2 line profile (yellow). The model assumes rigid body rotation and each spectral line in each pixel is Doppler-shifted according to its distance to the planetary rotation axis. Assuming a constant angular velocity of the atmosphere, the line of sight velocity is calculated via $V_{LOS} = V_{rot} \times \sin\theta$ with V_{rot} being the planetary rotation velocity and θ being the line of sight angle. The absorption arising from the atmosphere with the largest distance to the rotation axis ($\theta = 90°$) shows the largest Doppler shift. Additional winds are dealt additive in each pixel e.g. in case of zonal jet streams, the line of sight velocity is the sum of all velocity contributions i.e. $V_{LOS} = (V_{rot} + V_{Jet}) \times \sin\theta$. Day-to-nightside winds are not included in the model, assuming that these act in the same way at all latitudes and longitudes, leading to an overall net blueshift of the final line profiles without inducing a line deformation.

Figure 6.1 demonstrates the model. The left panel shows a Jupiter type planet with V_{rot} = 6 km/s, where only the atmospheric circle at $R_{pl} < R_{Atmo} < 1.3 \times R_{pl}$ (with R_{pl} being the white light radius of the planet) contributes to the transmission signal. The middle panel shows few Doppler-shifted absorption profiles (dashed) arising from the different parts of the atmosphere for illustration purposes, whereas the final line profile (solid black) is the sum over all pixels on the atmospheric circle. The right panel shows the line profile before broadening (yellow) and the line profile after broadening (black). For demonstration purposes, the dashed lines show the broadened line profiles not accounting only for the atmospheric circle but the full surface (i.e. similar to stellar surfaces) from the model used in this work (magenta) and the [1] PyAstronomy tool *pyasl.fastRotBroad* (green) which introduces rotational broadening for stellar surfaces according to (Gray & Corbally, 1994). Accounting only for absorption by a transparent circle leads to a broader and shallower line profile. Therefore, it is important to account for this effect to not over-/underestimate the velocity amplitudes needed to broaden spectral lines, especially for large velocities as the deviation increases non-linear with increasing velocity amplitude.

[1] https://github.com/sczesla/PyAstronomy

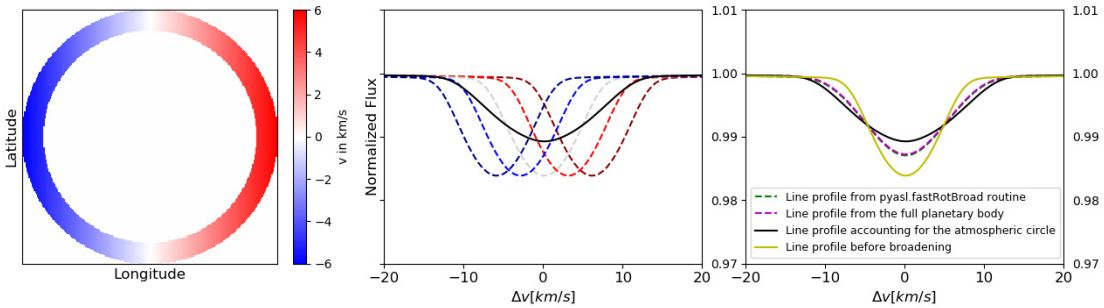

Figure 6.1: Effect of rotational broadening on absorption lines. Left panel: Illustration of an absorbing circle from the transparent region of a Jupiter type planet with a planetary rotation of ± 6 km/s. Middle panel: Dashed lines show absorption lines that are shifted in velocity with the colour coding illustrating the different regions from the atmospheric circle. The black solid line shows the final line profile which is the sum of all velocity shifted contributions. Note, that there is an overdensity of line profiles around the line core region of the black solid line which are not shown for better visibility of the illustration. Right panel: Yellow solid line shows the line profile before broadening and the black solid line after the broadening. The dashed lines show the broadening if one accounts for the full surface i.e. similar to a stellar surface and compares this work (magenta) to the PyAstronomy tool *pyasl.fastRotBroad* (green).

6.4 Method

This study aims to investigate the line deformation of spectral lines induced by atmospheric winds in form of zonal jet streams in high resolution transmission spectra. For this, it is assumed that the atmospheric motion introduces a Doppler-shift to the spectral lines leading to a velocity broadening in form of rotational broadening, thus not changing the intrinsic Doppler-width of the absorption lines from each pixel element from the transparent atmospheric circle. Shown is the integrated absorption line profile in the planetary rest frame, assuming that the high spectral resolution spectra taken at short exposure times (to avoid Doppler smearing, see e.g. Cauley et al. (2020)) are corrected for spurious observational and instrumental effects (see e.g. Wyttenbach et al. (2020) for a comprehensive overview on extracting transmission spectra). Such effects could be telluric contamination, stellar activity or velocity shifts due to the planetary orbital motion, whereby in the latter case one has to consider non-zero eccentricities, non-edge orbits, or other factors that could lead to radial velocity shifts in the residual spectra, which could be misunderstood as the effect of different kind of winds (Zhang et al., 2017).

Different scenarios will be investigated showing different wind patterns for a Jupiter type planet with V_{rot} = 3 km/s and with V_{rot} = 6 km/s. The rotational velocity of V_{rot} = 3 km/s is representative for the rotational velocity of an HJ (see e.g. HD189733b with ∼2.7 km/s) and the rotational velocity of V_{rot} = 6 km/s representative for the rotational velocity of an UHJ (see e.g. KELT-9b with ∼6.6 km/s). The scenarios presented are described below (see corresponding sections for further details on the motivation):

1. The rotational broadening in an extended ($R_{pl} < R_{Atmo} < 1.1 \times R_{pl}$) and unextended ($R_{pl} < R_{Atmo} < 1.5 \times R_{pl}$) atmosphere with a weaker and stronger Nai-absorption line (Section 6.5.1)

2. A eastward streaming equatorial zonal jet with $V_{Jet} = \mp$ 6 km/s at the trailing and leading limb respectively and different widths reaching latitudes of $\pm 20°$ and $\pm 40°$ (Section 6.5.2)

3. A eastward streaming equatorial zonal jet with asymmetric velocities on the limbs being $V_{Jet} = \mp 6$ km/s at the trailing and $V_{Jet} = \mp 2$ km/s at the leading limb (i.e. a third velocity amplitude) reaching latitudes of $\pm 20°$ and $\pm 40°$ (Section 6.5.3)

4. A eastward streaming equatorial zonal jet with $V_{Jet} = \mp$ 6 km/s at the trailing and leading limb respectively reaching a latitude of $\pm 20°$ and westward streaming zonal jets at the poles with $V_{WJet} = \pm$ 2 km/s and $V_{WJet} = \pm$ 6 km/s (Section 6.5.4)

5. Timely resolved spectra during ingress and egress for the demonstrated science cases in Section 6.5.2, Section 6.5.3 and Section 6.5.4 showing a Jupiter type planet with $V_{rot} = 3$ km/s (Section 6.5.5)

To investigate if the wind structure according to the Scenarios (ii)-(v) can be differentiated from the profiles that are not accounting for winds or even between the different wind properties, the required observational stellar spectral signal-to-noise (S/N) values are shown in the corresponding sections (i.e. Section 6.5.2, Section 6.5.3, Section 6.5.4 and Section 6.5.5). The quantitative determination of a wind pattern with high significance will require high spectrally and timely resolved observations with high S/N ratios by observations with current high-resolution spectrographs. The required spectral mean S/N from the stellar spectrum can be approximated by:

$$S/N_{n\sigma} \approx \frac{1}{\overline{|\Delta F|}} \times \frac{n\sigma}{\sqrt{m} \times \sqrt{obs} \times \sqrt{spec} \times \sqrt{lines}} \approx \frac{1}{\overline{|\Delta F|}} \times \Phi_{\mathrm{Planet}} \tag{6.1}$$

Here, "$\overline{|\Delta F|}$" is the mean of the absolute flux difference between the modelled line profiles i.e. the difference between the broadened and unbroadened line profiles as well as the difference between the broadened line profiles with different wind properties. "$(\overline{|\Delta F|})^{-1}$" is approximated as the required mean S/N per resolved spectral resolution element (neglecting minor error contributions such as from the "Master-out" spectrum, which is used to infer the transmission profile, see e.g. Wyttenbach et al. (2020)). In the second term, abbreviated by Φ_{Planet}, nσ is the significance of the detection, "m" the number of resolved points, "obs" the number of observed transits, "spec" the number of snapshots for the same pattern for one transit (i.e. one for ingress/ egress observations but several during the in-transit phase) and "lines" the number of spectral lines which can be combined (assuming similar absorption line strengths). To investigate the detectability of the wind pattern on a real test case, Φ_{Planet} is determined for the exoplanet HD189733b for a 3σ (n$\sigma = 3$) detection and one transit (obs = 1), with m = 58 (corresponding to points ± 15 km/s around the line core), lines = 2 (assuming that 2 Nai-D-lines are used) and spec $\approx$ 18 (assuming that an exposure time of 4 min (neglecting readout time) is taken between the second and third contact of HD189733b). This results in $\Phi_{\mathrm{HD189733b}} \approx 0.066$ during the in-transit phase Scenarios (ii)-(iv) and $\Phi_{\mathrm{HD189733b}} \approx 0.279$ for Scenario (v), because for the latter, only single snapshots are possible.

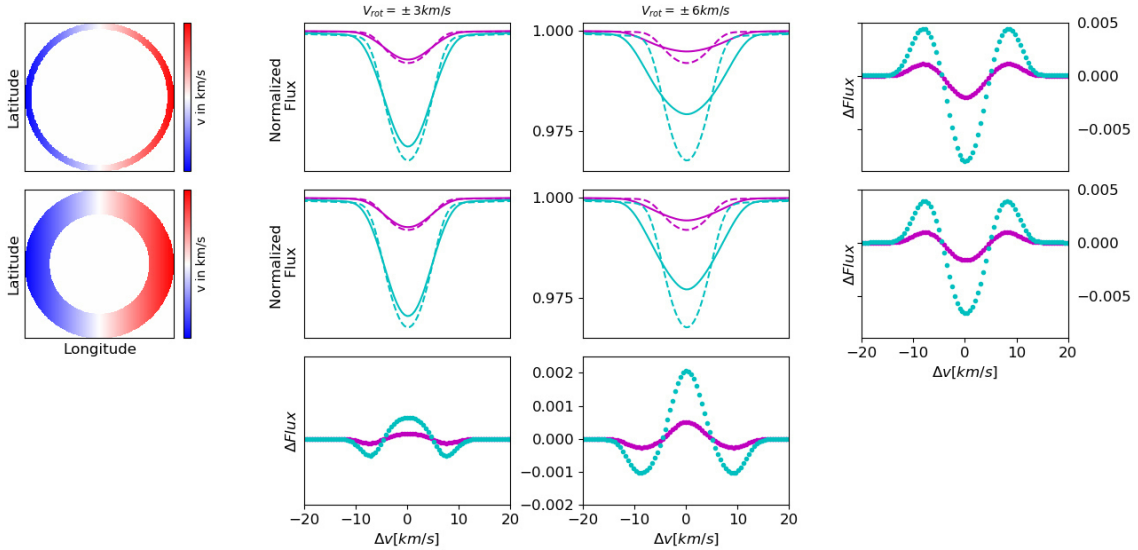

Figure 6.2: The effect of rotational broadening on a stronger (magenta) and weaker (purple) Nai absorption line before (dashed) and after (solid) broadening. The Nai-D2 line from Keles et al. (2020) is scaled for this purpose. The translucent atmospheric circle is set to ($R_{pl} < R_{Atmo} < 1.1 \times R_{pl}$) (first line) and ($R_{pl} < R_{Atmo} < 1.5 \times R_{pl}$) (second line). The second column shows a Jupiter type planet with $V_{rot} = 3$ km/s and the third with $V_{rot} = 6$ km/s. The first column illustrates the science cases. The third row shows the difference between the broadened line profiles from the panels above and the forth column shows the difference between the broadened line profile from the different rotating planets (each for the same line strength). Each column shares the x-axis and the second and third column share the same y-axis.

The computational time of the different wind structure in this work is cheap requiring only a few seconds each on a laptop computer with Intel Core i7 -10510U CPU. But note, that 1D modeling procedures may underestimate physical effects of particular importance considered in 3D modelling approaches (Kempton et al., 2014). The interplay between atmospheric dynamics and rotation is a complex issue and the atmospheric Doppler signature a combination of multidimensional wind fields and rotation rate (Flowers et al., 2019). Also other effects such as high-altitude clouds, atmospheric metallicities and atmospheric temperature inversion can affect the heat redistribution in those atmospheres (Zhang et al., 2018), making the application of advanced general circulation modells necessary. Several caveats are discussed in Section 6.6.

6.5 Results

6.5.1 Rotational broadening of weaker and stronger Nai- lines in an extended and unextended atmosphere

Exoplanet atmospheres of Jupiter type planets can show big diversity e.g. in gravity, temperature and sodium- abundance. The atmospheres can have small and large scale heights with weaker and stronger absorption lines, making the fingerprints of these rotating atmospheres diverse in transmission spectra.

To account for such diversities, Figure 6.2 shows a Jupiter type planet with $V_{rot} = 3$ km/s and $V_{rot} = 6$ km/s with an extened and unextended atmosphere showing a weak and a strong Nai-absorption line (see Figure caption for further information). Inspecting the

first row with the unextended atmosphere, the rotating atmospheres show broadened line profiles for both V_{rot} cases where the weaker and stronger line profiles become shallower and broader compared to the non-broadened ones as expected. This effect is stronger for the faster rotating planet due to the stronger Doppler-shift of the line profiles and significantly stronger visible for the stronger line profiles compared to the weaker ones in sense of absolute flux values, also suggested by the difference plot in the fourth column.

Inspecting the second row with an extended atmosphere, the line deformations look quite similar to that is demonstrated for the unextended atmosphere. Comparing the difference in line profiles for an extended and unextended atmosphere, hence the panels in the third row, the difference is small for the slower rotating planet and increases for the faster rotating one, again the effect being stronger for the stronger absorption line profiles. The positive peak at the line core region shows that the line profiles from the extended atmosphere are deeper, thus showing less broadening, compared to the unextended atmospheres. This is due to the enhanced contribution to the line core region from Nai-lines which are less shifted in velocity arising from the wider transparent atmospheric circle. Thus, assuming that the rotational velocity is the same on the trailing and leading limb, the contribution of absorption lines which are less shifted in velocity is larger for unextended atmospheres than for extended, as the line of sight contribution decreases with longitude.

In conclusion, line broadening (or deformation) is stronger for faster rotating planets, whereas the width of the translucent atmospheric ring is of relatively less importance compared if one has in mind that the extended atmosphere is four times wider in our scenario (note, that the line strength is assumed to be the same varying R_{atmo} in the model used, so that the extension only affects the contribution of different Doppler-shifts). For large rotational velocities, weak absorption lines can become very shallow (e.g. see third column) and could be hidden within the noise level of transmission spectra. However, note that the equivalent width of the lines is conserved in case of rotational broadening. Due to this, the absorption signature may be inferred with the so called "excess method" where the flux is integrated within passbands and normalized thereafter showing the atmospheric absorption in excess light curves (see e.g. Keles et al. (2019)). The atmospheric extension will be fixed to ($R_{pl} < R_{Atmo} < 1.3 \times R_{pl}$) for the upcoming scenarios and not varied, as the variation has a negligible effect on the qualitative outcome of the results.

6.5.2 Effect of an eastward streaming zonal jet reaching latitudes of ±20° and ±40° on the Nai- absorption line

This scenario investigates the effect of an zonal jet stream on a Jupiter type planet with $V_{rot} = \pm 3$ km/s (second column) and $V_{rot} = \pm 6$ km/s (third column). Such a jet stream can extend from the equator to latitudes around 20°-60°, thus dominating the surface of such a giant planet (Showman & Polvani, 2011; Showman et al., 2012). The width of such a jet stream is controlled by the Rossby deformation radius, which increases for larger atmospheric scale height and slower planetary rotation rates (Showman et al., 2008; Heng & Showman, 2015). The existence of such jet streams on a planet depend on the one side on the stellar irradiation and so the radiative time constant and on the other side on the frictional drag within the atmosphere (Heng & Showman, 2015). For strongly irradiated planets with weak atmospheric frictional drag, day-to-nightside winds at low pressure level dominate but also zonal jet streams at higher pressure level can originate. Decreasing the stellar insolation, zonal jet streams dominates at lower altitudes, which become unable to form increasing the strength of the frictional drag within the atmosphere (Showman et al., 2012). Thus, planets can posses day-to-nightside winds, zonal jet streams or even both. Note, that the jet streams here are assumed to be zonally present, but magnetic fields can

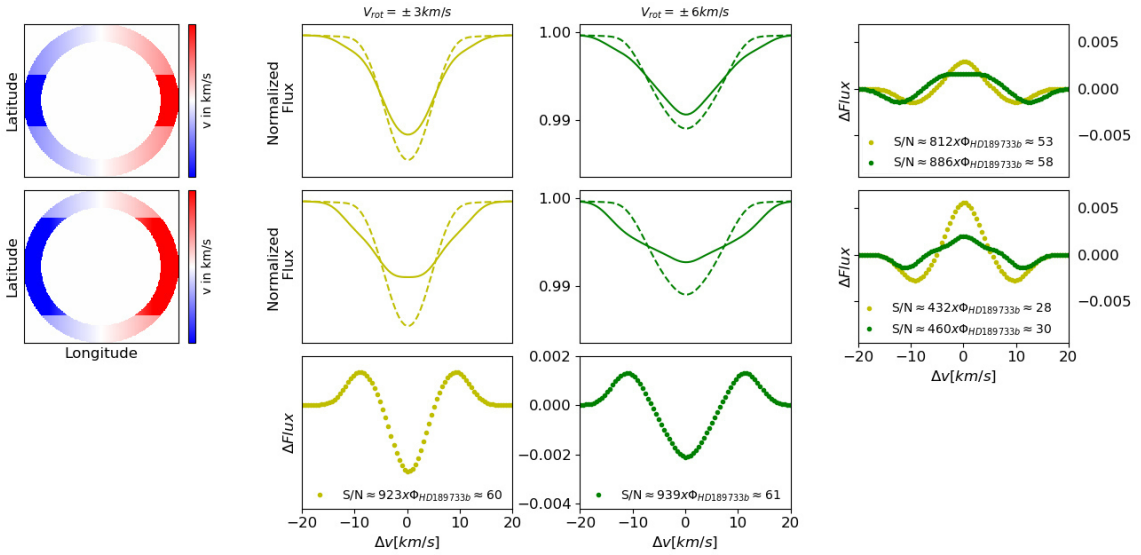

Figure 6.3: The effect of an eastward streaming jet with $V_{Jet} = \mp 6$ km/s $\times \sin\theta$ reaching latitudes of $\pm 20°$ (first row) and $\pm 40°$ (second row) on Nai-absorption lines (solid) on a planet with $V_{rot} = 3$ km/s (second column) and $V_{rot} = 6$ km/s (third column). The dashed lines consider only the planetary rotation for comparison. The atmospheric extension is fixed to ($R_{pl} < R_{Atmo} < 1.3 \times R_{pl}$). The first column illustrates the science cases. The fourth column show the difference between the broadened and unbroadened line profiles and the third row show the difference for the broadened line profiles with different jet streams. The label shows the 3σ spectral mean S/N value with $\Phi_{HD189733b} \approx 0.066$. Each column shares the x-axis and the second and third column share the same y-axis.

also perturb the circulation in ionized hot Jupiter atmospheres leading to circulation pattern not being anymore zonal (see e.g. Figure 3 in Batygin & Stanley (2014)). Moreover, atmospheric variability due to magnetohydrodynamic as well as hydrodynamic variability can lead to variable conditions on hot Jupiter atmospheres such as reversing the direction of the equatorial jet or shifting these in latitude (Komacek & Showman, 2019).

Figure 6.3 shows the effect of an eastward zonal jet stream reaching latitudes of $\pm 20°$ and $\pm 40°$ with a $V_{jet} = \mp$ 6 km/s $\times \sin\theta$ (see Figure caption for further information). Note, that the velocities are dealt additive, thus the maximum velocity at the trailing and leading limb is $V_{LOS} = \mp V_{rot} + \mp V_{jet}$, decreasing with $\sim\sin\theta$. Investigating the first row, the Nai- absorption line profiles become broadened similar to that is presented in Section 6.5.1, but are deformed more strongly. For the slower rotating planet, the zonal jet stream lead to deformations in the line core (which become flatter) and line wings (which become broader) due to the contribution of the Nai- lines which are stronger Doppler-shifted by the zonal jet stream. In comparison, for the faster rotating planet, the effect is less pronounced especially in the line core region. This is not surprising, as the combined maximum line of sight velocity is three times larger than the planetary rotation for the slower rotator, but only two times larger for the faster rotator, affecting stronger the line profiles from slower rotating planetary atmosphere. This is also suggested from the flux differences shown in the fourth column. Investigating the second row where the zonal jet stream reaches higher latitudes, the difference increases for both cases (also suggested by the difference plots in the third row), as the contribution from the Doppler-shifted Nai-lines from the polar regions (arising from the planetary rotation) decreases. For both

cases, the line cores flatten even more, the reason being the same as mentioned above.

The required spectral S/N values show that wider jet streams are easier to detect than narrower ones. The differentiation if a jet stream reaches either ±20° or ±40° is similarly difficult for both types of rotating planets.

In conclusion, the main difference between a streaming zonal jet reaching latitudes of ±20° and ±40° is the missing contribution of Doppler-shifted absorption lines arising from the planetary rotation at the line core region, but the enhanced contribution of Doppler-shifted absorption lines arising from the zonal jet stream at the region where the line wings arise. This leads the lines becoming shallower and broader with increasing the width of the streaming jet. In case of unextended atmospheres and large Doppler-shifts, the missing contribution from low velocity shifted absorption lines may introduce a w-shaped feature at the line core region (not shown here), which decreases with increasing contribution from less Doppler-shifted absorption lines. Wide zonal jet streams will be easier to detect on slower rotating Jupiter type planets compared to faster rotating ones as the line deformation show a larger contrast compared to the line broadening induced by planetary rotation.

6.5.3 Effect of an eastward streaming zonal jet with different velocities on the trailing and leading limb reaching latitudes of ±20° and ±40° on the Nai- absorption line

Due to tidal locking of close-in planets, the substellar point on the planetary dayside becomes the hottest region, the so called "hot spot". Equatorial streaming zonal jets can shift this "hot spot" into the direction of the planetary rotation (Miller-Ricci Kempton & Rauscher, 2012). This "hot spot" can have a large influence on the atmospheric wind pattern, leading to an asymmetric velocity pattern (see e.g. Figure 4 in Miller-Ricci Kempton & Rauscher (2012) or Figure 6, 7 and 8 in Showman et al. (2012)). One example for such a influence could be a shifted "hot spot" which triggers day-to-nightside winds with different strengths on the atmospheric transparent circle, which combine with the planetary rotation and streaming zonal jet to asymmetric wind pattern on the both hemispheres. Furthermore, asymmetric wind pattern could be also arise if the planets rotational axis is not perpendicular to the orbital plane (Cauley et al., 2020). Non-uniform wind patterns within the atmosphere can lead to asymmetric Doppler-shifts of the Nai- absorption lines on the translucent atmospheric ring resulting in asymmetric absorption line profiles (Kempton et al., 2014; Flowers et al., 2019).

To investigate on such a scenario, Figure 6.4 shows the same wind pattern as shown in Section 6.5.2 but with different line of sight velocities on the eastern and western hemispheres (i.e. $V_{\text{E-LOS}} = (V_{\text{rot}} + V_{\text{JET}}) \times \sin\theta$ on the eastern hemisphere and $V_{\text{W-LOS}} = 0.33 \times (V_{\text{rot}} + V_{\text{JET}}) \times \sin\theta$ on the western hemisphere, thus a third in velocity amplitude).

Investigating the first row, the line profiles become highly asymmetric compared to the line profiles shown in Section 6.5.2, where the absolute streaming jet velocity is the same on both hemispheres. This is explained by the difference in Doppler-shift from both hemispheres, where at the western hemisphere the Nai- absorption lines are stronger blueshifted than redshifted on the eastern hemisphere. Due to this difference in Doppler-shifts, the line profile is not anymore symmetrical with respect to the line center. For the slower rotating planet, the maximum line of sight velocity at the leading limb becomes $V_{\text{LOS}} = 3$ km/s and thus the same to V_{rot} so that the line wings overlap with the dashed line profile which considers only the planetary rotation. For the faster rotating planet the maximum line of sight velocity becomes $V_{\text{LOS}} = 4$ km/s and thus 50% smaller than the planetary rotation velocity, leading to a slight difference in the line wings. However, at

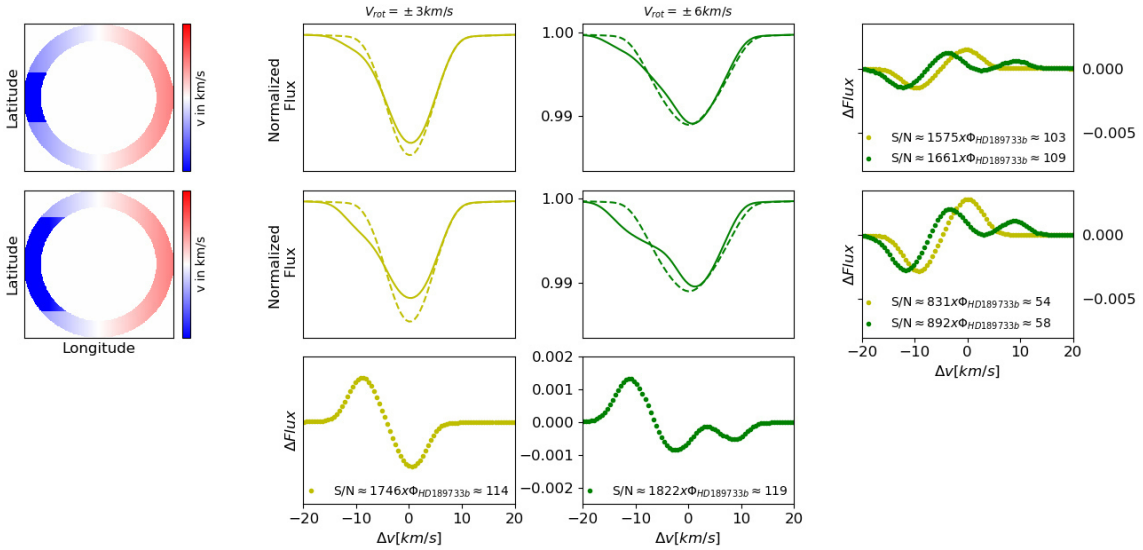

Figure 6.4: The effect of an eastward streaming jet with with $V_{JET} = \mp$ 6 km/s and line of sight velocity of $V_{E\text{-}LOS} = (V_{rot} + V_{JET}) \times \sin\theta$ on the eastern hemisphere and $V_{W\text{-}LOS} = 0.33 \times (V_{rot} + V_{JET}) \times \sin\theta$ on the western hemisphere reaching latitudes of $\pm 20°$ (first row) and $\pm 40°$ (second row) on Nai- absorption lines (solid) on a planet with $V_{rot} = 3$ km/s (second column) and $V_{rot} = 6$ km/s (third column). The dashed lines consider only the planetary rotation for comparison. The atmospheric extension is fixed to ($R_{pl} < R_{Atmo} < 1.3 \times R_{pl}$). The first column illustrates the science cases. The fourth column show the difference between the broadened and unbroadened line profiles and the third row show the difference for the broadened line profiles with different jet streams. The label shows the 3σ spectral mean S/N value with $\Phi_{HD189733b} \approx 0.066$. Each column shares the x-axis and the second and third column share the y-axis.

the trailing limb, the line profiles are more strongly deformed similar to that is shown in Section 6.5.2, with the difference that the line cores are deeper in this scenario due to the larger contribution from the lower velocity Doppler-shifted Nai- absorption lines from the eastern hemisphere.

Increasing the width of the streaming jet (second row), the effects become stronger leading to stronger line deformation, especially blueward the line core due to the increase in Nai- absorption lines which are Doppler-shifted for a wider jet stream whereas the difference is again small redward the line core, the reason being the same as mentioned above. The panel in the third column and fourth row showing the flux differences illustrate the mentioned deviations in the line profiles.

Similar to Scenario 6.5.2, the wider jet streams are easier to detect and the differentiation of the jet stream width is similarly difficult for both type of rotating Jupiter type planets, with the difference that the required spectral S/N values are around a factor of two higher compared to the wind pattern without asymmetric velocities on the hemispheres.

In conclusion, the missing high velocity contribution at the eastern hemisphere has two main effects on the line profiles: First, the line profile becomes more asymmetric due to the difference in blueshifted and redshifted absorption lines from the eastern and western hemisphere, which increases with increasing width of the zonal jet stream. Second, as line properties of resolved line profiles are usually derived by Gaussian fits assuming symmetric lines, the asymmetric Doppler-shifted line profiles would mimic a blueshift of the line core.

Thus asymmetric wind patterns can mimic blueshifts of resolved line profiles especially for planets with lower V_{rot} and strong asymmetric velocities on the two planetary hemispheres.

6.5.4 Effect of an eastward streaming zonal jet reaching latitudes of ±20° with additional westward streaming jets at the poles on the Nai-absorption line

In the solar system, the gas giants show a wide equatorial eastward streaming jet and additionally large number of smaller zonal jets streaming from east to west, whereas the ice giants have a small number of eastward streaming jets at high latitudes additional to a sub-rotating equatorial westward streaming jet. A explanation for the differences is shown in Lian & Showman (2010), where the water abundance (which is way different for the ice giants and gas giants) and the corresponding large scale latent heating of the atmosphere due to the condensation of water vapor seems to play a major role. For Jupiter type exoplanets, westward streaming jets with lower velocity amplitudes, which are triggered from the hot dayside, can also arise additional to an eastward streaming equatorial jet (see e.g. Showman et al. (2008)).

Figure 6.5 investigates a scenario on a Jupiter type planet with V_{rot} = 3 km/s and V_{rot} = 6 km/s with a eastward streaming jet reaching ±20° with $V_{Jet} = \mp$ 6 km/s and two westward streaming jets at the poles with $V_{WJET} = \pm$ 2 km/s (first row) and with $V_{WJET} = \pm$ 6 km/s (second row). Note, that the velocity amplitude decreases with $\sim\sin\theta$ (thus the atmospheric velocities at the polar regions are $< V_{WJET}$). The planetary rotation slows down the wind velocities from the westward streaming jet at the poles (i.e. the absolute V_{LOS} decreases) and increases the wind velocities for the eastward streaming jet (i.e. the absolute V_{LOS} increases). See caption in Figure 6.5 for further information.

Investigating the first row, the line profile for the slower rotating planet looks very similar to the line profiles presented in Section 6.5.2, where only a eastward streaming jet is considered. This is not surprising, as the Nai-lines from the polar regions are only weakly Doppler-shifted by velocities $< V_{LOS} = \pm$ 1 km/s, being in the same order to that would be caused by the planetary rotation at such latitudes. In case of the faster rotating planet, the weak Doppler-shift of the absorption lines introduce a stronger contribution at the line core region and less on the line wings, leading to a deeper line core but shallower line wings compared to the profiles shown in Section 6.5.2, where westward streaming jets are absent.

Investigating westward streaming jets with larger velocity amplitude (second row), the line profile for the slower rotating planet does not show a significant difference compared to the weaker westward streaming jet case (see flux difference in the third row). The line profile becomes the same as shown in the first row Section 6.5.2, as the line of sight velocity becomes $< V_{LOS} = \pm$ 3 km/s, which is the same absolute velocity amplitude compared to a planet with V_{rot} = 3 km/s, but only streaming to the opposite direction. Due to the symmetry, this results in a scenario where westward streaming jets can not be distinguished from the effect of planetary rotation without time dependent line profile analysis. For the faster rotating planet, even more interesting, the line of sight velocity at the poles becomes $V_{LOS} = V_{WJET} + V_{rot} = 0$, thus leads to zero Doppler-shift of the absorption lines, so that a stagnant atmosphere is mimicked at the polar regions. The absorption lines from these regions increase the contribution in the line core, so that the line profiles look deeper and narrower compared a planet with the same planetary rotation but absence of such streaming jets.

The required spectral S/N values show that the faster V_{WJET} cases are slightly easier to detect than the slower ones for both type of rotating Jupiter type planets, but the differentiation of the profiles with different V_{WJET} requires way more S/N, especially for

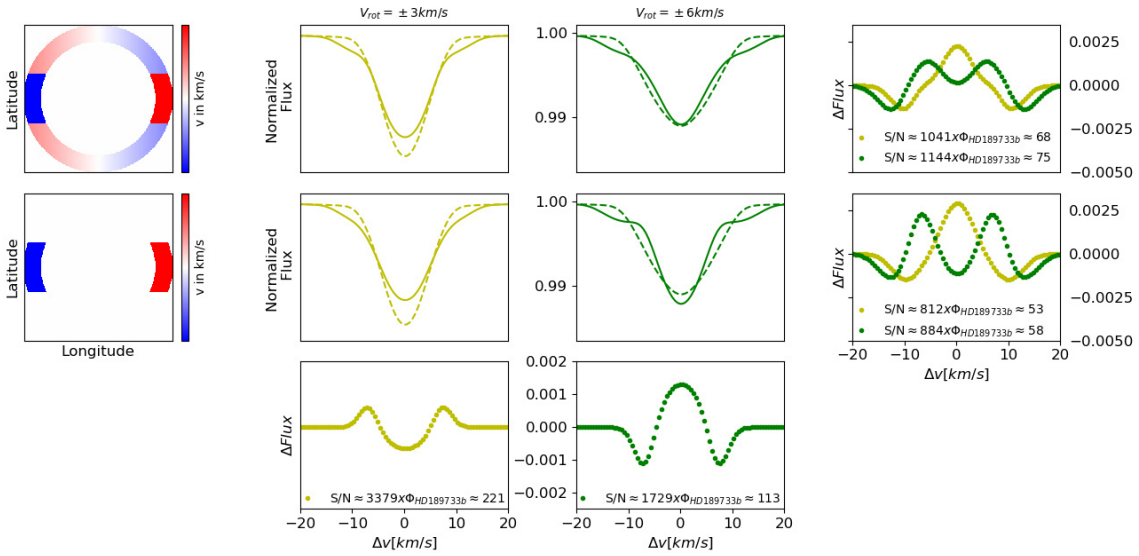

Figure 6.5: The effect of an eastward streaming jet with $V_{Jet} = \mp 6$ km/s reaching latitudes of ±20° and two westward streaming jets at the poles with $V_{WJET} = \pm 2$ km/s (first row) and $V_{WJET} = \pm 6$ km/s (second row) on Nai-absorption lines (solid) on a planet with $V_{rot} = 3$ km/s (second column) and $V_{rot} = 6$ km/s (third column). The dashed lines consider only the planetary rotation for comparison. The atmospheric extension is fixed to ($R_{pl} < R_{Atmo} < 1.3 \times R_{pl}$). The first column illustrates the science cases for the faster rotating planet. The fourth column show the difference between the broadened and unbroadened line profiles and the third row show the difference for the broadened line profiles with different westward streaming jet velocities. The label shows the 3σ spectral mean S/N value with $\Phi_{HD189733b} \approx 0.066$. Each column shares the x-axis and the second and third column share the same y-axis.

the slower rotating planet.

In conclusion, the combination of eastward and westward streaming zonal jets can show line profiles which are deeper and narrower compared to line profiles broadened only by planetary rotation. This effect increases on the one side for decreasing width of the eastward streaming jet and on the other side increasing the contribution from Nai- lines with little Doppler-shift from the polar regions. Note, that increasing the westward streaming jet velocity, larger Doppler-shifts will be the case vanishing out this effect, making this result very case dependent and only arising for $V_{LOS} = V_{WJET} + V_{rot} \approx 0$.

6.5.5 Time dependent line profile variation during ingress and egress

The previous scenarios were focused on the resolved absorption signature during the second and third contact. But different broadening mechanisms (e.g. expansion, hydrodynamic, thermal and the ones presented in this work) can be degenerated and thus not possible to discern them in this case (Cauley et al., 2020). As the line profiles can look very similar for different wind patterns only accounting for the in-transit phase (as demonstrated), line profiles inferred during ingress and egress can be used with the aim to distinguish between the different wind patterns on the exoplanets (Cauley et al., 2020). For instance, Louden & Wheatley (2015) resolved spatially winds on HD189733b investigating the Nai- lines during ingress and egress showing different excess velocities on the trailing and leading limb.

To investigate on timely resolved profiles, Figure 6.6 shows a Jupiter type planet ro-

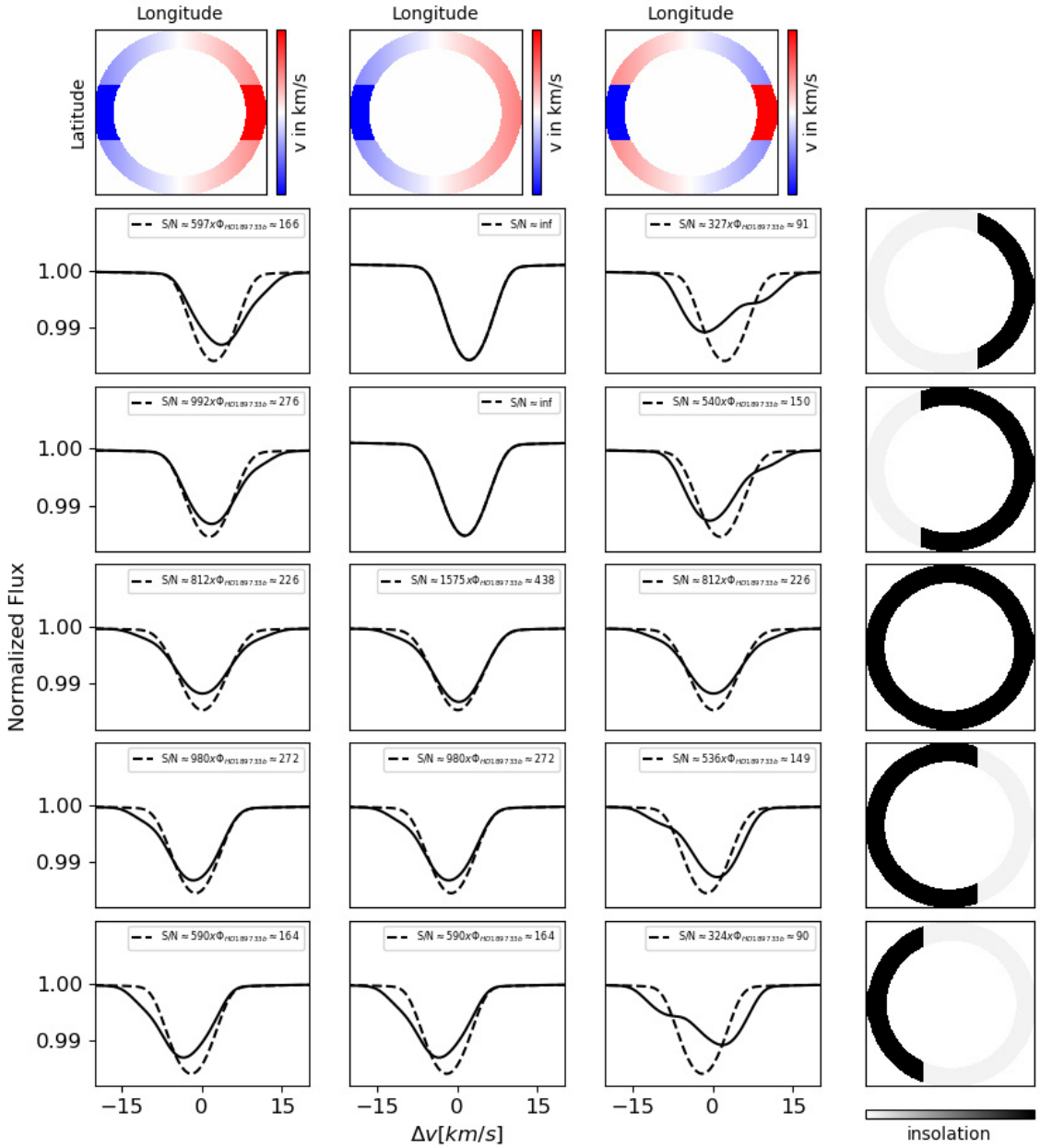

Figure 6.6: Time dependent line profiles for different snapshots during ingress and egress for a Jupiter type planet with V_{rot} = 3 km/s. Column 1, 2 and 3 show the same scenarios as presented in Section 6.5.2, Section 6.5.3 and Section 6.5.4, respectively. The dashed lines consider only the planetary rotation for comparison. The fourth column shows the different snap shots during ingress and egress, whereas the black shaded region illustrates the illuminated atmospheric region. The label shows the 3σ spectral mean S/N value with $\Phi_{\mathrm{HD189733b}} \approx 0.279$. Each column shares the x-axis and the panel with the line profiles share the y-axis.

tating with V_{rot} = 3 km/s and an eastward streaming jet into the same direction with $V_{Jet} = \mp 6$ km/s reaching a latitude of 20° (first column, see also Section 6.5.2), the same scenario with a third line of sight velocity on the leading limb (second column, see also Section 6.5.3) and an eastward streaming jet reaching a latitude of 20° with westward streaming jets on the poles with $V_{WJet} = \pm$ 6 km/s (third column, see also Section 6.5.4). The fourth column shows the illuminated part of the planet at which the line profiles are investigated.

Investigating the first column with an eastward streaming jet, the line deformation over time is symmetric. The line profile shows a redshift induced from the leading limb during ingress and a blueshift induced from the trailing limb during egress. Furthermore, the streaming jet affects the line wings due to the enhanced contribution from Doppler-shifted Nai- absorption at ingress and egress. This is evident through the comparison to the dashed line profile, where only the planetary rotation is considered.
Adding an asymmetry to the wind pattern by decreasing the line of sight velocity on the leading limb by a factor of three (second column), the line profile also becomes redshifted during ingress. This profile is not distinguishable from a planet which only shows planetary rotation, as the line of sight velocities for both cases become very similar. On the other side, the line profile on the trailing limb during egress is identical with the line profile in the first column, thus showing a blueshift with affected line wings. However, since the line profiles are different at the leading limb for the symmetric and asymmetric wind pattern scenarios, the scenarios can be still distinguished.
The strongest line profile deformation is observed when eastern and western streaming jets within the planetary atmosphere are included (third column). In this case, the line profiles arising from poles and equatorial region are shifted to opposite directions for the same snapshot, showing much broader and shallower lines, which are not symmetrical due to the different velocity contributions. The line deformation is symmetric over time for the ingress and egress phase, but opposite to the other scenarios, a blueshift is suggested on the leading limb during ingress which becomes a redshift on the trailing limb during egress. Interestingly, this scenario is not distinguishable from the scenario shown in the first column, if one accounts only for the line deformation during the second and third contact (see also Section 6.5.4), showing the importance of accounting for line deformation during the ingress and egress phase.
The required spectral S/N values for ingress and egress investigations are larger compared to the previous Scenarios, as only snapshots can be used and not several co-added spectra during the second and third contact. Note, that also the S/N for the fourth row is calculated as a snapshot for better comparison, although here in-transit spectra could be co-added. The westward polar jet stream scenario required the lowest S/N values during ingress and egress, followed by the conventional zonal jet stream reaching latitudes of ±20°. For the asymmetric jet stream velocity case, only the egress snapshots deviate from the dashed line profiles.
Note, that including day-to-nightside winds would introduce additional blueshift to all line profiles shown here. This would increase the blueshift and decrease the redshift of the line profiles shown during ingress and egress phase.

6.6 Discussion

6.6.1 Detectability of atmospheric wind pattern

The investigation of different wind patterns in Section 6.5 showed that S/N values in the order of few dozens to few hundreds per resolved spectral resolution element in the stellar spectrum are needed to detect the wind pattern significantly. Current high-resolution

spectrographs at large telescopes such as PEPSI (Potsdam Echelle Polarimetric and Spectroscopic Instrument, see e.g. Strassmeier et al. (2018a))) or ESPRESSO (Echelle SPectrograph for Rocky Exoplanets and Stable Spectroscopic Observations, see e.g. Pepe et al. (2010)) might be able to reach such values within few transit observations. For comparison, the star HD189733 was observed with PEPSI (14.10.2017) at a exposure time of 30 min and a spectral resolution of R ≈130 000. Extrapolating the S/N per spectral resolution element for an exposure time of 4 min results in an S/N value of ∼160 at ingress/egress and around ∼130 to ∼40 within the second and third contact inspecting the stellar Nai- line (not shown here). The S/N values for the different orbital phases are different as during the transit the atmospheric absorption becomes Doppler-shift due to the orbital motion of the planet around the stellar Nai- line core. The values show that such wind patterns are detectable with current high-resolution spectrographs within few transits. But although high-resolution spectrographs could be able to differentiate between the different wind patterns, there is a degeneracy especially with other effects which could introduce line broadening e.g. vertical upward winds (Seidel et al., 2020) and atmospheric turbulences (Keles et al., 2020), which is discussed in Section 6.6.3.

6.6.2 Investigating the resolved Nai-D2 lines on different exoplanets

The study of gaseous exoplanet atmospheres revealed the strong absorption of Nai- lines. To investigate if those lines show line broadening, which could be induced by winds, Nai-D2 lines inferred from high resolution transit observations of different exoplanets will be analyzed. Table 6.1 shows a list of resolved Nai-D2 lines where a line contrast (LC) and FWHM from a Gaussian fit is stated (see the caption for the corresponding authors). The planets are ordered by their equilibrium temperature inferred from the [2]TEPCat database (Southworth, 2011). There is a tendency that the FWHM is decreasing for planets with a larger equilibrium temperature. However, these planets have different properties which could lead to different absorption profiles, which need to be accounted for.

To investigate on this, the *petitRADTRANS* code (Mollière et al., 2019, 2020) is employed to calculate synthetic high resolution transmission spectra for all planets shown in Table 6.1. For this, an isothermal temperature profile and different reference pressure level but the same solar sodium abundance and a mean molecular atmospheric weight of 2.33 is assumed. The synthetic spectra are converted via $(1\text{-}(R_{pl}/R_{star})^2)$ and normalized making them comparable to the observational spectra. The stellar and planetary parameters are taken from the TEPCat database.

It is important to recall that transit observations probe the ∼mbar pressure regimes at the terminator, where the temperature profile may not be isothermal, but appropriate for a first order approximation. As the temperature at the terminator is not precisely known and differs from the equilibrium temperature, synthetic lines with different isothermal temperatures were computed in steps of 200 K ranging from 1000K to 9000K and their corresponding FWHM determined. Assuming that a possible line broadening is due to a superrotating zonal jet stream where one can consider flux conservation, the equivalent width of the Gaussian profiles in Table 6.1 is calculated and used to determine the LC of a Gaussian profile which has the same FWHM as the synthetic line profile. This procedure is applied to enable a more appropriate comparison of the line profiles as the alkali lines show wide Lorentzian line wings compared to the Gaussian line profiles. Due to this, the normalization of such spectra is usually a crucial step affecting the line depth. But as the Lorentzian lines have very sharp line cores, the determined FWHM do not change for slight changes of the line depth. Applying a sanity check by introducing 30% larger line depths showed no significant effects on the results.

[2]https://www.astro.keele.ac.uk/jkt/tepcat/

Table 6.1: Na-D2 line properties found for different exoplanets.

Exoplanet	HD189733b	WASP-52b	WASP-49b	WASP-127b	WASP-17b	WASP-76b	KELT-20b
$T_{equilibrium}$ [K]	1191	1315	1399	1400	1755	2228	2261
FWHM [Å]	[1]0.52 ± 0.08	[2]0.424 ± 0.036	[3]0.42 ± 0.1	[4]0.367 ± 0.097	[5]0.20 ± 0.08	[6]0.619 ± 0.174	[7]0.17 ± 0.04
	[8]0.64 ± 0.04					[4]0.400 ± 0.065	
Line contrast [%]	[1]0.64 ± 0.07	[2]1.31 ± 0.13	[3]1.99 ± 0.49	[4]1.144 ± 0.270	[5]1.3 ± 0.6	[6]0.373 ± 0.091	[7]0.32 ± 0.05
	[8]0.72 ± 0.05					[4]0.57 ± 0.08	

Note: ,[1]Wyttenbach et al. (2015), [2]Chen et al. (2020), [3]Wyttenbach et al. (2017), [4]Žák et al. (2019), [5]Khalafinejad et al. (2018), [6]Seidel et al. (2019), [7]Casasayas-Barris et al. (2019), [8]Casasayas-Barris et al. (2017). As for WASP-17b only the Gaussian width was shown, the FWHM here is derived via FWHM = $\sigma \times 2.355$. For KELT-20b, the LC and FWHM is the mean value from the HARPS-N and CARMENES data shown. The FWHM were shown in velocity units and is transformed here to Å.

The line profile is broadened (using the model presented in Section 6.3, assuming ($R_{pl} < R_{Atmo} < 1.3 \times R_{pl}$)) in steps of 0.2 km/s and compared (±FWHM around the line core) with the observational profiles from Table 6.1, until a minimum χ^2-value is determined. This approach yield very similar broadening values for the different synthetic profiles with different isothermal temperature, showing that the change in FWHM of the spectral lines for the different temperature is small compared to the broadening value required to match the observations. The error bars are calculated using the uncertainties stated for the line properties in Table 6.1 by determining the broadening for the Gaussian profiles varied by ± 1-σ in LC and FWHM. Figure 6.8 (appendix) shows the comparison between the observational line profiles from Table 6.1 and the line profiles inferred in this work.

Figure 6.7 shows the broadening values V_{bro} for the Nai-D2 lines subtracted from their expected planetary rotational velocity V_{rot}. The excess velocity which is left over is attributed here to a superrotating atmosphere, which is assumed to arise from a zonal jet stream (i.e. $V_{Jet} = V_{bro} - V_{rot}$). For HD189733b and WASP-76b the mean V_{Jet} values are shown inferred for the different investigations. There is a indication that the exoplanets with lower equilibrium temperature tend to show less broadening of their atmospheric Nai-D2 lines.

As demonstrated, such line broadening can be explained by zonal jet streams on the planetary surface. If the broadening is induced by such a streaming jet, the correlation would imply that HJ type planets favor more the existence of zonal jet streams compared to UHJ type planets. One explanation for this could be that the thermal ionization of alkali lines may induce drag to winds by Lorentz forces (Perna et al., 2010; Batygin & Stevenson, 2010; Zhang et al., 2018), which is stronger on UHJ. Increasing the amount of ionized particles, the Lorentz drag and the inflation of Jupiter type planets due to ohmic dissipation (where kinetic energy is converted into heat which becomes deposit in the interior) increases (Zhang et al., 2018). Thorngren & Fortney (2018) showed that this inflation of the giant planet atmospheres peaks at $T_{eq} = 1500$K, decreasing for larger temperature. The result shown here strengthens this idea that magnetic drag of ionized particles is more efficient for planets with $T_{eq} > 1500$K, decreasing the efficiency of atmospheric circulation and thus jet stream velocities. Except for WASP-76b, all planets with $T_{eq} > 1500$K show jet-velocities which are consistent with zero within their error bar, matching well into the big picture. Note, that WASP-76b has quite large error bar and that quite different Nai-D2 line properties were measured for this exoplanet. Atmospheres with moderate temperature and high alkali amounts may favor the existence of strong zonal streaming jets which can yield stronger broadened absorption lines, whereas hotter planets may experience thermal ionization of those alkalis reducing the wind strengths of zonal jets, leading to less broadened line profiles.

A result strengthening this picture is shown by Zhang et al. (2018), where the authors showed that the phase offset of the "hot spot" which is shifted by winds is stronger for giant planets with lower irradiation temperature (therefore hinting on stronger jet streams), however, increasing again for irradiation temperatures > ∼3400 K (see their

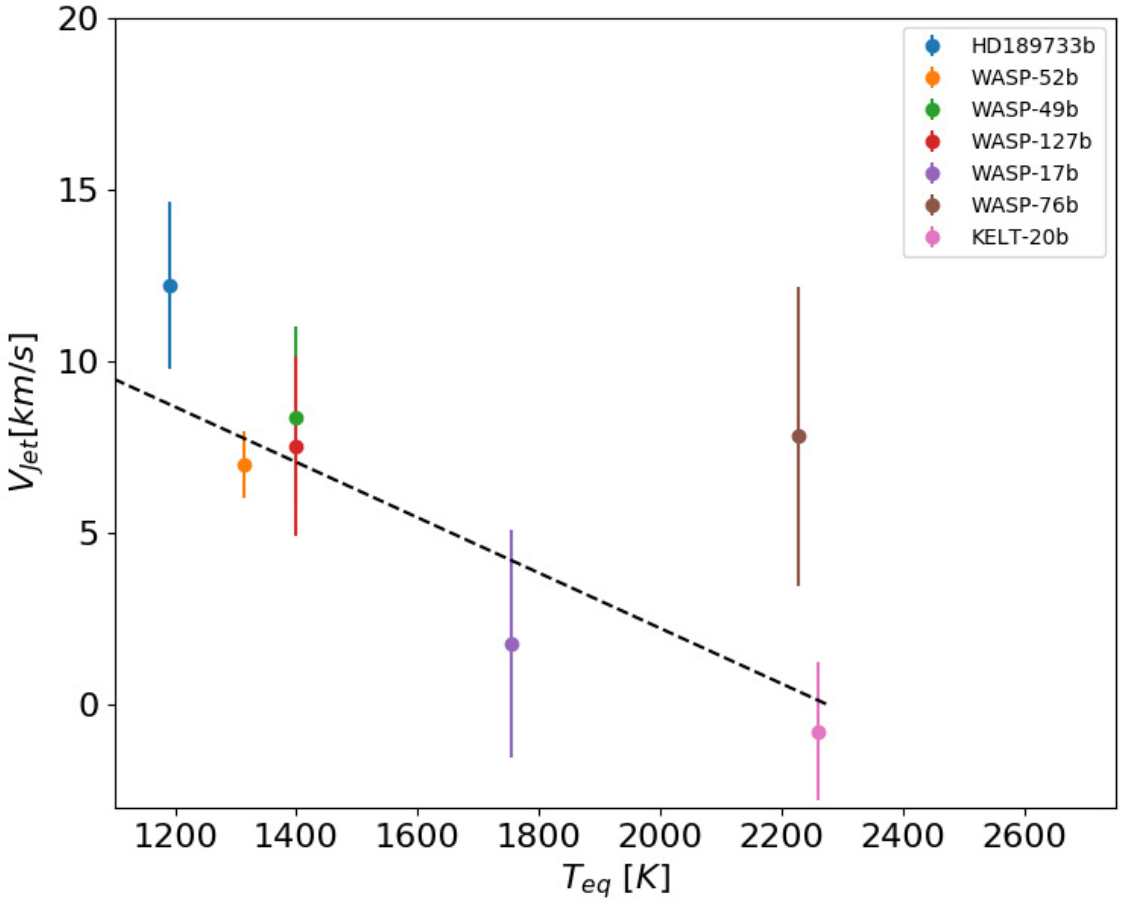

Figure 6.7: Inferred broadening values for the Nai-D2 lines detected on different exoplanets presented in Table 6.1. The y-axis shows the excess velocity i.e. $V_{Jet} = V_{bro} - V_{rot}$.

Figure 14). Note that the heat recirculation efficiency can increase on UHJ type planets with very high T_{eq} due to the dissociation and recombination of H_2 (Bell & Cowan, 2018), as shown for instance for KELT-9b (Wong et al., 2020). Another way around, such drags lead to inefficient heat redistribution within the atmospheres. This increases the day- and nightside temperature contrast and triggers stronger day-to-nightside winds on UHJ type planets, which result in stronger blueshifts of spectral lines in transmission spectra (Ehrenreich et al., 2020).

Applying a linear fit to the data (black dashed line) in Figure 6.7 using the Python package *scipy.optimize.curvefit* (Jones et al., 01), the following correlation between the equilibrium temperature and excess velocity is inferred:

$$V_{Jet} = -0.0081^{\pm 0.0021} \times T[eq] + 18.33^{\pm 3.17} \quad (6.2)$$

The errors correspond to the 1-σ standard deviation error, showing a $\sim$3.9-σ deviation compared to a straight line, indicating that the correlation is significant.

Although the existence of zonal jet streams is an established theory, where the findings in Figure 6.7 match into the big picture, the velocity amplitudes are quite large and very strong wind speeds should be considered cautiously (see also Section 6.6.3). The approach demonstrated has large error sources to consider. The employed model yields the broadening values under the assumption that the planetary rotational axis is perpendicular to the orbital plane. For the exoplanets where this is not the case, the velocity amplitudes will

be underestimated. Although all targets are observed using high resolution instruments, the difference in the instrumental setup and data reduction technique could introduce significant deviations in the stated line profile properties in Table 6.1, even for absorption signature detected on the same exoplanets (Wyttenbach et al., 2020). This is also suggested in Table 6.1, where different authors find different line properties for the Nai- lines resolved for the same exoplanet. Moreover, using high resolution observations in which one mainly probes the line cores of these absorption lines, where Gaussian approximation may a valid assumption, the Gaussian profiles do not fit perfectly to the observational Nai- lines and will introduce large errors. For instance, Keles et al. (2020) inferred broadening values around ∼10-12 km/s for the Nai-D2 line for the exoplanet HD189733b (see their Figure 5), which would lead to $V_{Jet} \approx$ 7-9 km/s, a lower value than the broadening value inferred here using the Gaussian line properties. Therefore, the inferred broadening values from this work should be considered cautiously, as the error bars are most probably underestimated. However, this work shows only a first order approximation for the correlation between the broadening of the Nai-D2 lines for higher equilibrium temperature (which is also suggested only by inspecting Table 6.1) and it does not aim to determine the atmospheric wind pattern, which would be out of the scope of this work.

The line broadening of the Nai-D2 lines could be explained also by another mechanism instead of a jet stream. For example, such a strong line broadening was not inferred for the water lines (Brogi et al., 2016) or the potassium line (Keles et al., 2020) on the exoplanet HD189733b, which one may expect. However, these lines probably probe lower altitudes compared to the sodium lines, which may explain the difference in line broadening. Contradicting to this, with decreasing pressure, the day-to-night temperature contrast increases (Zhang et al., 2018), thus probably slowing down wind velocities. More advanced modelling effort would be needed to prove this, which is out-of-the scope of this work. Future observations resolving the Nai- lines on different exoplanets will help to prove this prediction.

6.6.3 Caveats

The results presented in this work depend strongly on the assumptions made, which are discussed here.

This work considers only the broadening of spectral lines due to velocity broadening, assuming uniform wind pattern for the different scenarios i.e. that the wind velocities only change with the line of sight contribution. But winds can vary also strongly as a function of speed and height (Brown, 2001) leading to non-uniform wind pattern e.g. depending on the frictional drag within the atmosphere (see Figure 4 in Miller-Ricci Kempton & Rauscher (2012)), resulting possibly in more bimodal line profiles (Showman et al., 2012). Furthermore, the assumption of flux conservation i.e. that the equivalent width of the absorption lines is conserved, is only valid if wind velocities vary only with latitude and longitude, but not valid for wind variations within the line of sight chord (Brown, 2001), which would affect the wind velocities inferred in this work. A more accurate way of introducing broadening to the line profiles could be to introduce the broadening to the height dependent opacity contributions instead of assuming equal opacity at each depth (see e.g. Brown (2001)) and using 2D (see e.g. Cauley et al. (2020)) or even 3D modelling approaches (see e.g. Flowers et al. (2019)).

Another assumption made in this work is that the day-to-nightside wind acts the same everywhere on the terminator region, leading to a net blueshift of the spectral lines without affecting the line widths. However, day-to-nightside winds are expected to stream at a lower pressure level compared to where zonal jet streams arise (see e.g. Showman et al. (2008)), where both winds could combine and show a more complex non-uniform

wind pattern. Comparing Figure 6 from Showman et al. (2012), day-to-nightside winds may differ also for different latitudes and longitudes on the terminator region, which would affect the line profile deformation even more. However, the investigation of this phenomenon considering both effects and including the pressure dependence is out of the scope of this work.

Note, that also other kinds of atmospheric motions could introduce a large velocity signature into line profiles, such as evaporative winds caused by the absorption of high energetic radiation (Debrecht et al., 2020) or planetary magnetic fields which may propel ions to high velocities at higher altitudes where they recombine at the same speed (Seidel et al., 2020). Moreover, vertical upward winds are of special interest, which are not considered in this work. Seidel et al. (2020) investigated the effect of different kind of winds on the Nai- line profiles on HD189733b, including superrotating atmospheres, vertical upward winds as well as the combination of both. Such vertical upward winds are perpendicular to the planetary surface and result in a small line of sight contribution within transmission spectra, leading to large wind velocities, which would be required for enhanced line broadening. But winds in form of zonal jet streams can combine with such vertical wind components, introducing a degeneracy, complicating the determination of zonal jet streams and their properties. In conclusion, line broadening by winds may not be attributed only to zonal jet streams.

The combined velocities at the photospheres of exoplanets can reach 100% or larger velocity values than the equatorial rotational velocities (Spiegel et al., 2007). The largest velocities in the scenarios presented in Section 6.5 can reach ∼12 km/s, being similar to the velocities inferred from the investigation of the observational Nai-D2 lines (see Figure 6.7). From the observational point of view, velocities close to those values are inferred published in different investigations. As mentioned, Keles et al. (2020) showed that the Nai- lines on HD189733b need to be broaden around 10 km/s to match the observational line profiles. Recently, Ehrenreich et al. (2020) investigated the nightside condensation of iron on the UHJ WASP-76b inferring the absorption of atmospheric iron on the trailing limb, which shows a blueshift of -11 ± 0.7 km/s. Even more recently, Cauley et al. (2020) investigated the Balmer-lines and broadening by day-to-nightside winds, jet streams, thermal and rotation broadening on WASP-33b inferring a rotational velocity of around 10.1 ± ∼0.9 km/s.

From the theoretical point of view, although drag-free simulations provide wind velocities up to ∼15 km/s (Miller-Ricci Kempton & Rauscher, 2012), super-sonic winds below the exobase are not possible and introducing drag (which is a more realistic assumption) can decrease significantly the maximum possible wind velocities, showing a slight tension with the observational results. The sound speed of non-degenerate molecular hydrogen is approximately V = 2.4 x $(T/1000\ K)^{0.5}$ km/s (Goodman, 2009). For moderate temperatures, this velocity should be around 3-4 km/s in the upper atmospheric layers (Snellen et al., 2008). Thus, the inferred large wind speeds may be overestimated in this work. However, note that stellar gravity and magnetic field could move the sonic point to lower altitudes, enabling larger wind velocities at higher altitudes (Wyttenbach et al., 2020). But the purpose of this work is to show the qualitative effect of super-rotating streaming jets on spectral line profiles. Modeling approaches accounting for non-uniform wind patterns as well as frictional drag within the atmosphere is out of the scope and purpose of this work.

6.7 Summary

Close-in exoplanets experience strong stellar insolation. As these planets are expected to be tidally locked, the constant energetic bombardment on the dayside builds up a

so called "hot spot" and triggers atmospheric winds due to the uneven heating of the hemispheres and planetary rotation (Brown, 2001). Such winds are mainly categorized into either day-to-nightside winds at higher altitudes which push the atmosphere into the line of sight of the observer during transit or zonal jet streams at lower altitudes which rotate into the direction of planetary rotation (Miller-Ricci Kempton & Rauscher, 2012; Showman et al., 2012). The main effect of day-to-nightside winds are blueshifts of absorption signature within the planetary atmosphere, whereas zonal jet streams tend to broaden these absorption lines.

This work shows the effect of zonal jet streams in high resolution transmission spectra on Jupiter type planets rotating with V_{rot} = 3 km/s and V_{rot} = 6 km/s by introducing rotational broadening to synthetic line profiles. Different scenarios were presented showing different wind patterns with eastward and westward streaming zonal jet streams which reach different latitudes and introduce deformation to absorption lines. This work shows that especially during the ingress and egress phase the line deformation can help to distinguish different wind patterns within the atmospheres.

In different exoplanet atmospheres, the Nai- lines were resolved showing large differences in line widths in comparison to what would be expected only by accounting for planetary rotation. Comparing the observational findings with modeled line profiles, this work demonstrates that planets with larger equilibrium temperatures show less broadened Nai-D2 absorption lines. This shows that strong zonal jets arise more efficiently on HJ compared to UHJ consistent with theoretical expectations (Showman et al., 2012), if the broadening is attributed to zonal jets. One explanation could be that the ionization of alkali atoms introduces drag into these winds in atmospheres of UHJ (Perna et al., 2010), leading to inefficient heat redistribution and slowing down the wind velocities. Note, that the recirculation efficiency can increase for very large atmospheric temperature due to the dissociation and recombination of H_2 (Bell & Cowan, 2018), leading to zonal jet streams also on UHJ. However, one should note that the explanations given in this work should be adopted cautiously due to the large error sources that were discussed.

Atmospheric dynamics can induce further to planetary rotation line broadening and shifts on the absorption lines, depending on the wind profiles of the probed atmospheric region (Flowers et al., 2019). Evidently, especially the alkali lines can be a good tracer for such winds on exoplanets.

6.8 Appendix

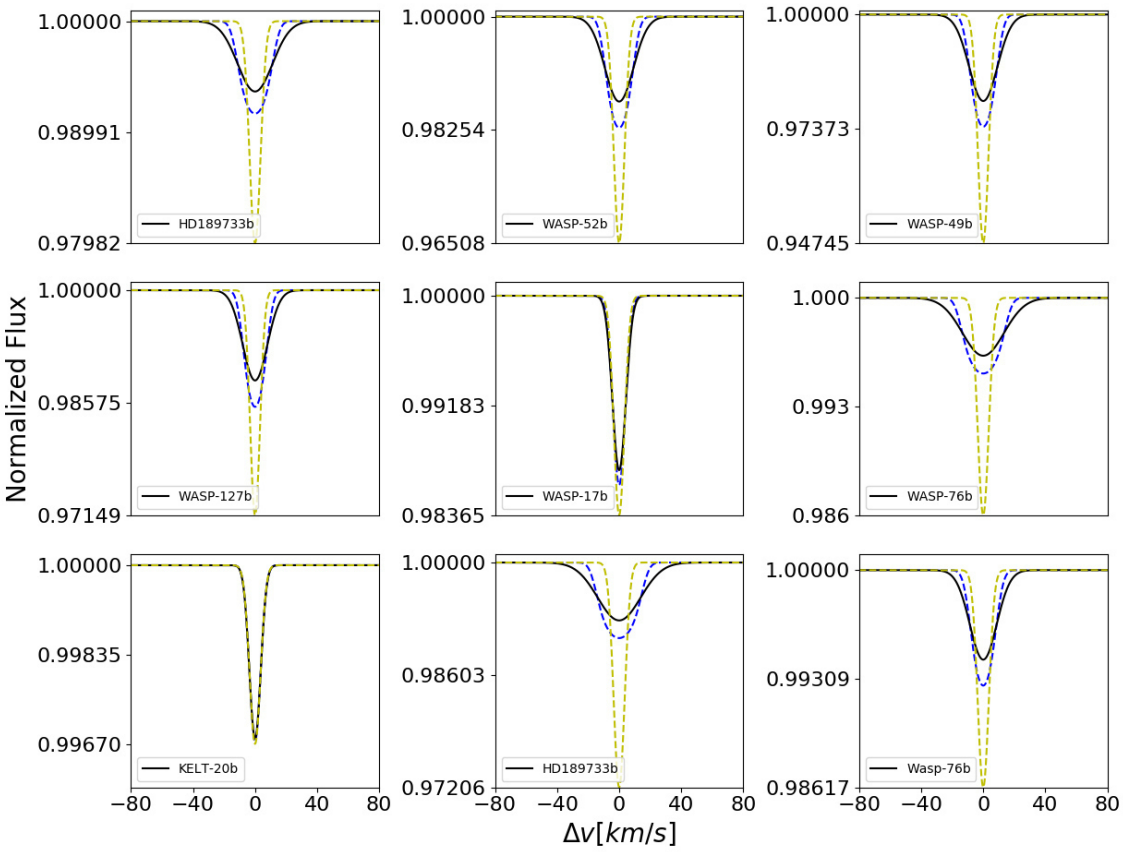

Figure 6.8: Shown are the best matching line profiles between the observational (see also Table 6.1 for comparison) Gaussian line profiles (black solid) and the broadened line profiles inferred from the equivalent width comparison (blue dashed). The dashed yellow line shows the unbroadened line profile. The different columns share the x-axis.

7 Discussion

The comparison of the presence and absence of atmospheric constituents on different planets can give clues about atmospheric processes to understand the trigger of those. As shown in the Manuscripts I-III, especially the alkali lines are well suitable for this. However, different aspects of the investigations need to be discussed (where I refer to the Section 2 for the caveats belonging to the methods used).

7.1 Investigating exoplanets with the alkali lines: The Potassium Detection

The alkali lines have a strong absorption cross-section and sodium is detected previously on HD209458b and HD189733b, hinting that potassium should also be present on both planets as both alkalis have similar ionization and condensation properties. The detection of potassium on HD189733b applying high-resolution observation and its absence on HD209458b enabled us to speculate about clouds and depletion processes on the latter planet. As such clouds can hide spectral features, there is a degeneracy between clouds and depletion processes of elements in exoplanet atmospheres. However, the non-detection of sodium in a later study on HD209458b (Casasayas-Barris et al., 2020), would rather hint at high altitude clouds (Helling et al., 2016) hiding both features rather than depletion of potassium, showing that the degeneracy of clouds and depletion processes can be overcome by comparing different absorption signature to each other.
Although the detection of potassium is not surprising as also sodium is detected on HD189733b, it is in tension with the non-detection of potassium in a previous study by Jensen et al. (2011). Using the HRS instrument at the Hobby-Eberly Telescope, the authors could not detect potassium, where this may have different reasons: First, the authors applied the observation using a twice smaller instrumental resolution making it more challenging to detect the thin Ki absorption compared to the investigation by Keles et al. (2019). Furthermore, the authors did not account for the RM- effect in their transmission spectra which is known to introduce spurious signature in high-resolution investigations (Casasayas-Barris et al., 2020). However, their "excess absorption" level at an integration band of 8Å is different than what is found by Keles et al. (2019), which is not expected as the CLV- effect plays no significant role fur such large bandwidths, similar to the ínstrumental resolution. Of course, the developed CLV-model depends on 1D- stellar spectra and could therefore underestimate this effect. However, as this effect is decreasing for larger bandwidths, this effect should be negligible at such large integration bandwidths for any deviation in stellar spectral profiles. Most probably, the difference may arise due to a difference in data reduction techniques or may be induced by the stellar activity of HD189733, which is known to introduce spurious signature into high-resolution observations (Cauley et al., 2018). However, another high-resolution observation of HD189733b to confirm the presence of potassium is desirable.
Comparing the high-resolution detection of potassium on HD189733b to other works, Chen et al. (2020) were able to detect potassium on the exoplanet WASP-52b observed with the high-resolution spectrograph ESPRESSO (Echelle SPectrograph for Rocky Exoplanets and Stable Spectroscopic Observations) at the Very-Large-Telescope, confirming further to Keles et al. (2019) observational the existence of potassium in giant planet atmospheres.

The reason for the late detection of potassium compared to sodium in high-resolution observations is most probably induced by the availability of instruments on very large telescopes which are able to observe the potassium line at 7699Å. The resonant potassium line absorption around 7664Å is challenging to investigate, as this line arises around strong telluric oxygen lines.

7.2 Tracing atmospheric chemistry and properties with the alkali lines

The high-resolution detection of potassium on HD189733b shown in Manuscript I further to previously detected sodium (Wyttenbach et al., 2015; Casasayas-Barris et al., 2017) opened new opportunities to trace the atmospheric chemistry and dynamics on this planet with high-resolution observations. Observing a single absorption line on a planet can give clues about the presence of an atmospheric constituent, where the next step would be to compare atmospheric properties such as abundances to the host star and to other exoplanets of the same type. The comparison of the exoplanet metallicities with the solar system ones (Welbanks et al., 2019) is a key aim to understand the differences and similarities in the formation and evolution of planets.
But the absorption signature can not be compared directly between planets or even between different absorption signatures on the same planet to estimate absolute abundances or abundance ratios as ground-based high-resolution observations remove the atmospheric continuum information during the renormalization process of the observed spectra. Hence, there arises a degeneracy between the atmospheric reference radius, pressure, and the mixing ratio of atmospheric species hindering the exact abundance determination which can be overcome only under circumstances (Benneke & Seager, 2012; Fisher & Heng, 2018; Brogi & Line, 2019; Welbanks & Madhusudhan, 2019; Keles et al., 2020) e.g. by combining multi-resolution as well as multi-wavelength observations (Brogi et al., 2017; Pino et al., 2018a). Making use of this, we parameterized the haze continuum of HD189733b which was determined in a previous low-resolution observation by Pino et al. (2018a) and used the alkali line absorption profiles to probe the atmosphere of HD189733b. For this, the potassium absorption line was resolved. Due to stellar activity, an emission feature arose in the line core region additional to the residual RM- effect. To account for these effects, we modeled the RM-effect and combined it with the fitted emission feature to reveal the planetary absorption. Of course, this approach could have introduced a spurious signature into the potassium line profile. But tracing the atmospheric absorption over the planetary motion during transit, we confirmed the potassium absorption, in agreement with the absorption inferred by the "excess method". Being able to compare for the first time both sodium and potassium in high-resolution observations with synthetic transmission spectra, the investigation hints either on a very large sodium to potassium ratio on HD189733b so that potassium may be depleted on this planet or on alkali lines which probe different altitudes on this planet in contrast to that is expected. Different aspects hint at the latter scenario: The significant depletion of potassium in contrast to sodium is not expected (Lavvas et al., 2014; Lavvas & Koskinen, 2017), similar to a primordial difference in the alkali element abundances. Moreover, investigating different sodium to potassium ratios on exoplanets with low-resolution data, (Welbanks et al., 2019) inferred sodium to potassium ratio similar to the stellar one. A reason why the alkalis probe different altitudes could be due to their different masses, as potassium is heavier, and thus may be settled down easier on the planet at lower altitudes with lower temperature.
The investigation showed also that the sodium lines are way broader compared to the potassium lines, hinting at upper atmospheric winds, which are also inferred in other in-

vestigations (Louden & Wheatley, 2015; Gebek & Oza, 2020; Seidel et al., 2020). The results suggest wind velocities in the order of 8-10 km/s which manifest themselves in the broadening of the sodium lines. Comparing the wind velocities to other works which investigated winds on HD189733b, Seidel et al. (2020) inferred line-of-sight wind velocities which are 2-3 times larger, similar to Gebek & Oza (2020). However, the kind of winds and method applied to infer the wind velocities are different, making a forward comparison difficult. The potassium line does not show such a strong broadening, which favor their existence in lower altitudes, where the winds seem to play a less significant role. This is also implied by the investigation of the water lines which probe also low altitudes and show no significant broadening (Brogi et al., 2016), similar to the potassium line. The combined investigation of HD189733b with both alkali lines in a high-resolution observation inferred its atmospheric properties as well as allowed us to speculate about the winds on this planet, where especially the sodium lines arising at high altitudes seems to play an important role.

7.3 Tracing atmospheric dynamics with the alkali lines

These findings within Manuscript II arose the question, if absorption lines observed in high-resolution observations during transit can trace winds also on other hot- and ultra hot Jupiter-type planets with different properties, which can give more detailed clues about the dynamics of those atmospheres. Comparing the winds on the solar system giant planets, there is a large diversity e.g. several narrow zonal jets streaming eastward on Jupiter and Saturn, but wide zonal jets on Uranus and Neptune streaming westward at the equatorial region and eastward at the poles (Lian & Showman, 2010). Of course, hot Jupiter-type planets are way diverse than the planets in the solar system, but investigations showed that also polar westward streaming jets can exist here triggered by the large day-to-nightside temperature contrasts (Showman et al., 2008). The investigation of the dynamics for different kinds of planets is important to understand the mechanisms of planetary evolution.

Comparing the sodium lines detected in different exoplanet atmospheres with synthetic spectra with the aim to investigate winds in form of zonal jet streams, there is a hint that the sodium lines are stronger broadened for Jupiter type planets with lower equilibrium temperature, hinting at stronger winds. The decrease of the wind strengths for hotter planets is in agreement with theoretical expectations, where the ionization of alkali lines introduce drag to those winds decreasing their strength (Perna et al., 2010). However, the investigation is not applied to the data themselves but the inferred Gaussian line properties, introducing large errors to the resulting velocity amplitudes. Although the inferred velocity amplitudes are theoretically possible (Miller-Ricci Kempton & Rauscher, 2012) and also inferred for other gaseous planets (Ehrenreich et al., 2020; Cauley et al., 2020), such fast winds seem to be unreasonable and arise the question if other kinds of atmospheric processes could have introduced the observed line broadening. Atmospheric dynamics can have different forms and affect absorption signatures. For instance, magnetic fields could accelerate ions to high speeds which recombine at high altitudes resulting in large velocities, which could also introduce large broadening (Seidel et al., 2020). However, the next step would be to resolve such winds on planets spatially and timely to map the surface of these planets (Keles, 2021). Such a mapping could provide different properties of the winds such as size, strength and asymmetry and enable us to compare these to what we see in the solar system planets. Especially high-resolution spectrographs such as PEPSI (Strassmeier et al., 2018a) at large telescopes could be able for this observing a few transits e.g. of HD189733b to distinguish between the different wind pattern.

The main task will be the handling of systematic effects either from the instrument or

from the observations. Here, effects such as stellar activity, residual RM-effect, residual velocities or telluric contamination can have a large impact on the absorption line profiles (Wyttenbach et al., 2020) and needs to be accounted with high precision. Another main difficulty will arise to determine the main kind of winds acting on the line profiles due to the degeneracy of different wind patterns. Vertical upward winds (Seidel et al., 2020), atmospheric turbulences (Keles et al., 2020) and inhomogeneous absorption on the line of sight direction can broaden the line profiles in a similar way to zonal jet streams, showing that the line broadening of the sodium lines may not be attributed only to zonal jet streams. For instance, Seidel et al. (2020) showed that the Nai-line broadening on HD189733b requires the additional effect of vertical upward winds because zonal winds alone are not able to reproduce their derived Nai-line profiles. These effects will make it challenging to disentangle the inferred properties for the different wind mechanisms. To solve the degeneracy between those, more suitable models than presented in Manuscript III are necessary, for instance, 3D general circulation models, which can account for a variety of these factors.

7.4 Closing words

The detection of atmospheric signature and investigation of exoplanet atmospheres enables us to infer atmospheric processes which will increase our understanding of the formation and evolution of exoplanets and increase our understanding of our Solar system. This will enable us one day also to do so with Earth-like habitable planets, which may have different conditions than Earth, but are still habitable (Keles et al., 2018). This key prospect combined with high-resolution spectroscopy at larger telescopes is the first step to reach this aim. Within this thesis, it has been shown that strong absorption signature by alkali lines probed by high-resolution observations can be unique indicators to trace atmospheric properties and dynamics of gaseous exoplanets, enabling us to reveal the similarities and diversities of planetary atmospheres.

Bibliography

Allard N. F., Spiegelman F., Kielkopf J. F., 2016, http://dx.doi.org/10.1051/0004-6361/201628270 , http://adsabs.harvard.edu/abs/2016A

Allart R., Lovis C., Pino L., Wyttenbach A., Ehrenreich D., Pepe F., 2017, http://dx.doi.org/10.1051/0004-6361/201730814 , https://ui.adsabs.harvard.edu/abs/2017AA...606A.144A 606, A144

Asplund M., Grevesse N., Sauval A. J., Scott P., 2009, http://dx.doi.org/10.1146/annurev.astro.46.060407.145222 , http://adsabs.harvard.edu/abs/2009ARA

Barman T., 2007, http://dx.doi.org/10.1086/518736 , http://adsabs.harvard.edu/abs/2007ApJ...661L.191B 661, L191

Barnes J. R., Haswell C. A., Staab D., Anglada-Escudé G., 2016, http://dx.doi.org/10.1093/mnras/stw1713 , http://adsabs.harvard.edu/abs/2016MNRAS.462.1012B 462, 1012

Batalha N. M., 2014, http://dx.doi.org/10.1073/pnas.1304196111 Proceedings of the National Academy of Sciences, 111, 12647–12654

Batygin K., Stanley S., 2014, http://dx.doi.org/10.1088/0004-637X/794/1/10 , https://ui.adsabs.harvard.edu/abs/2014ApJ...794...10B 794, 10

Batygin K., Stevenson D. J., 2010, http://dx.doi.org/10.1088/2041-8205/714/2/l238 The Astrophysical Journal, 714, L238–L243

Baudino J.-L., Bézard B., Boccaletti A., Bonnefoy M., Lagrange A.-M., Galicher R., 2015, http://dx.doi.org/10.1051/0004-6361/201526332 , http://adsabs.harvard.edu/abs/2015A

Bell T. J., Cowan N. B., 2018, http://dx.doi.org/10.3847/2041-8213/aabcc8 The Astrophysical Journal, 857, L20

Benneke B., Seager S., 2012, http://dx.doi.org/10.1088/0004-637X/753/2/100 , http://adsabs.harvard.edu/abs/2012ApJ...753..100B 753, 100

Birkby J. L., 2018, Exoplanet Atmospheres at High Spectral Resolution (http://arxiv.org/abs/1806.04617 `arXiv:1806.04617`)

Borsa F., Zannoni A., 2018, http://dx.doi.org/10.1051/0004-6361/201833415 , https://ui.adsabs.harvard.edu/abs/2018AA...617A.134B 617, A134

Borucki W. J., et al., 2010, http://dx.doi.org/10.1126/science.1185402 Science, https://ui.adsabs.harvard.edu/abs/2010Sci...327..977B 327, 977

Bourrier V., et al., 2018, http://dx.doi.org/10.1038/nature24677 , https://ui.adsabs.harvard.edu/abs/2018Natur.553..477B 553, 477

Bower D. J., Kitzmann D., Wolf A. S., Sanan P., Dorn C., Oza A. V., 2019a, http://dx.doi.org/10.1051/0004-6361/201935710 , https://ui.adsabs.harvard.edu/abs/2019AA...631A.103B 631, A103

Bower D. J., Kitzmann D., Wolf A. S., Sanan P., Dorn C., Oza A. V., 2019b, http://dx.doi.org/10.1051/0004-6361/201935710 , https://ui.adsabs.harvard.edu/abs/2019AA...631A.103B 631, A103

Boyajian T., et al., 2015, http://dx.doi.org/10.1093/mnras/stu2502 , http://adsabs.harvard.edu/abs/2015MNRAS.447..846B 447, 846

Brogi M., Line M. R., 2019, http://dx.doi.org/10.3847/1538-3881/aaffd3 , 157, 114

Brogi M., Kok R. J. d., Albrecht S., Snellen I. A. G., Birkby J. L., Schwarz H., 2016, http://dx.doi.org/10.3847/0004-637x/817/2/106 , 817, 106

Brogi M., Line M., Bean J., Désert J.-M., Schwarz H., 2017, http://dx.doi.org/10.3847/2041-8213/aa6933 The Astrophysical Journal, 839, L2

Brown T. M., 2001, http://dx.doi.org/10.1086/320950 The Astrophysical Journal, 553, 1006–1026

Burrows A. S., 2014, http://dx.doi.org/10.1073/pnas.1304208111 Proceedings of the National Academy of Sciences, 111, 12601–12609

Burrows A. S., Marcy G. W., 2014, http://dx.doi.org/10.1073/pnas.1409934111 Proceedings of the National Academy of Sciences, 111, 12599

Burrows A., Volobuyev M., 2003, http://dx.doi.org/10.1086/345412 , http://adsabs.harvard.edu/abs/2003ApJ...583..985B 583, 985

Cameron A. C., Bruce V. A., Miller G. R. M., Triaud A. H. M. J., Queloz D., 2010, http://dx.doi.org/10.1111/j.1365-2966.2009.16131.x , 403, 151

Casasayas-Barris N., Palle E., Nowak G., Yan F., Nortmann L., Murgas F., 2017, http://dx.doi.org/10.1051/0004-6361/201731956 , http://adsabs.harvard.edu/abs/2017A

Casasayas-Barris N., et al., 2019, http://dx.doi.org/10.1051/0004-6361/201935623 , 628, A9

Casasayas-Barris N., et al., 2020, http://dx.doi.org/10.1051/0004-6361/201937221 , 635, A206

Castelli F., Kurucz R. L., 2004, arXiv Astrophysics e-prints, http://adsabs.harvard.edu/abs/2004astro.ph..5087C

Cauley P. W., Redfield S., Jensen A. G., Barman T., 2016, http://dx.doi.org/10.3847/0004-6256/152/1/20 , 152, 20

Cauley P. W., Redfield S., Jensen A. G., 2017, http://dx.doi.org/10.3847/1538-3881/aa6a15 , http://adsabs.harvard.edu/abs/2017AJ....153..217C 153, 217

Cauley P. W., Kuckein C., Redfield S., Shkolnik E. L., Denker C., Llama J., Verma M., 2018, http://dx.doi.org/10.3847/1538-3881/aaddf9 , http://adsabs.harvard.edu/abs/2018AJ....156..189C 156, 189

Cauley P. W., Shkolnik E. L., Ilyin I., Strassmeier K. G., Redfield S., Jensen A., 2019, http://dx.doi.org/10.3847/1538-3881/aaf725 , 157, 69

Cauley P. W., Wang J., Shkolnik E. L., Ilyin I., Strassmeier K. G., Redfield S., Cauley et al. A. J., 2020

Cegla H. M., Lovis C., Bourrier V., Beeck B., Watson C. A., Pepe F., 2016, http://dx.doi.org/10.1051/0004-6361/201527794 , 588, A127

Charbonneau D., Brown T. M., Noyes R. W., Gilliland R. L., 2002, http://dx.doi.org/10.1086/338770 , http://adsabs.harvard.edu/abs/2002ApJ...568..377C 568, 377

Chen G., Casasayas-Barris N., Pallé E., Yan F., Stangret M., Cegla H. M., Allart R., Lovis C., 2020, http://dx.doi.org/10.1051/0004-6361/201936986 , 635, A171

Czesla S., Klocová T., Khalafinejad S., Wolter U., Schmitt J. H. M. M., 2015, http://dx.doi.org/10.1051/0004-6361/201526386 , http://adsabs.harvard.edu/abs/2015A

Debrecht A., Carroll-Nellenback J., Frank A., Blackman E. G., Fossati L., McCann J., Murray-Clay R., 2020, http://dx.doi.org/10.1093/mnras/staa351 Monthly Notices of the Royal Astronomical Society, 493, 1292–1305

Deming D., et al., 2009, http://dx.doi.org/10.1086/605913 , https://ui.adsabs.harvard.edu/abs/2009PASP..121..952D 121, 952

Dobbs-Dixon I., Cumming A., Lin D. N. C., 2010, http://dx.doi.org/10.1088/0004-637x/710/2/1395 The Astrophysical Journal, 710, 1395–1407

Draine B. T., 2011, Physics of the Interstellar and Intergalactic Medium

Dravins D., Gustavsson M., Ludwig H.-G., 2018, http://dx.doi.org/10.1051/0004-6361/201833013 , http://adsabs.harvard.edu/abs/2018A

Ehrenreich D., et al., 2020, http://dx.doi.org/10.1038/s41586-020-2107-1 Nature, 580, 597–601

Esteves L. J., de Mooij E. J. W., Jayawardhana R., Watson C., de Kok R., 2017, http://dx.doi.org/10.3847/1538-3881/aa7133 , https://ui.adsabs.harvard.edu/abs/2017AJ....153..268E 153, 268

Fisher C., Heng K., 2018, http://dx.doi.org/10.1093/mnras/sty2550 , 481, 4698

Flowers E., Brogi M., Rauscher E., Kempton E. M.-R., Chiavassa A., 2019, http://dx.doi.org/10.3847/1538-3881/ab164c The Astronomical Journal, 157, 209

Ford E. B., 2014, http://dx.doi.org/10.1073/pnas.1304219111 Proceedings of the National Academy of Sciences, 111, 12616

Fortney J. J., Sudarsky D., Hubeny I., Cooper C. S., Hubbard W. B., Burrows A., Lunine J. I., 2003, http://dx.doi.org/10.1086/374387 , http://adsabs.harvard.edu/abs/2003ApJ...589..615F 589, 615

Fortney J., Lodders K., Marley M., Freedman R., 2008, http://dx.doi.org/10.1086/528370 The Astrophysical Journal, 678, 1419–1435

Fortney J. J., Shabram M., Showman A. P., Lian Y., Freedman R. S., Marley M. S., Lewis N. K., 2010, http://dx.doi.org/10.1088/0004-637X/709/2/1396 , http://adsabs.harvard.edu/abs/2010ApJ...709.1396F 709, 1396

Fossati L., Koskinen T., Lothringer J. D., France K., Young M. E., Sreejith A. G., 2018, http://dx.doi.org/10.3847/2041-8213/aaf0a5 , 868, L30

Gaidos E., Kitzmann D., Heng K., 2017a, http://dx.doi.org/10.1093/mnras/stx615 , http://adsabs.harvard.edu/abs/2017MNRAS.468.3418G 468, 3418

Gaidos E., Kitzmann D., Heng K., 2017b, http://dx.doi.org/10.1093/mnras/stx615 , https://ui.adsabs.harvard.edu/abs/2017MNRAS.468.3418G 468, 3418

Gebek A., Oza A. V., 2020, Alkaline Exospheres of Exoplanet Systems: Evaporative Transmission Spectra (http://arxiv.org/abs/2005.02536 `arXiv:2005.02536`)

Gibson N. P., de Mooij E. J. W., Evans T. M., Merritt S., Nikolov N., Sing D. K., Watson C., 2019, http://dx.doi.org/10.1093/mnras/sty2722 , http://adsabs.harvard.edu/abs/2019MNRAS.482..606G 482, 606

Gibson N. P., et al., 2020, http://dx.doi.org/10.1093/mnras/staa228 , 493, 2215–2228

Goodman J., 2009, http://dx.doi.org/10.1088/0004-637x/693/2/1645 The Astrophysical Journal, 693, 1645–1649

Gordon I. E., et al., 2017a, http://dx.doi.org/10.1016/j.jqsrt.2017.06.038 , https://ui.adsabs.harvard.edu/abs/2017JQSRT.203....3G 203, 3

Gordon I. E., et al., 2017b, http://dx.doi.org/10.1016/j.jqsrt.2017.06.038 , http://adsabs.harvard.edu/abs/2017JQSRT.203....3G 203, 3

Gray R. O., Corbally C. J., 1994, http://dx.doi.org/10.1086/116893 , http://adsabs.harvard.edu/abs/1994AJ....107..742G 107, 742

Gustafsson B., Edvardsson B., Eriksson K., Jørgensen U. G., Nordlund Å., Plez B., 2008, http://dx.doi.org/10.1051/0004-6361:200809724 , https://ui.adsabs.harvard.edu/abs/2008AA...486..951G 486, 951

Helling C., et al., 2016, http://dx.doi.org/10.1093/mnras/stw662 , http://adsabs.harvard.edu/abs/2016MNRAS.460..855H 460, 855

Heng K., Kitzmann D., 2017, http://dx.doi.org/10.1093/mnras/stx1453 , http://adsabs.harvard.edu/abs/2017MNRAS.470.2972H 470, 2972

Heng K., Showman A. P., 2015, http://dx.doi.org/10.1146/annurev-earth-060614-105146 Annual Review of Earth and Planetary Sciences, 43, 509–540

Hoeijmakers H. J., et al., 2018, http://dx.doi.org/10.1038/s41586-018-0401-y , http://adsabs.harvard.edu/abs/2018Natur.560..453H 560, 453

Hoeijmakers H. J., et al., 2019, http://dx.doi.org/10.1051/0004-6361/201935089 , 627, A165

Huang C., Arras P., Christie D., Li Z.-Y., 2017, http://dx.doi.org/10.3847/1538-4357/aa9b32 , 851, 150

Huitson C. M., et al., 2013, http://dx.doi.org/10.1093/mnras/stt1243 Monthly Notices of the Royal Astronomical Society, 434, 3252–3274

Jensen A. G., Redfield S., Endl M., Cochran W. D., Koesterke L., Barman T. S., 2011, http://dx.doi.org/10.1088/0004-637X/743/2/203 , http://adsabs.harvard.edu/abs/2011ApJ...743..203J 743, 203

Jensen A. G., Cauley P. W., Redfield S., Cochran W. D., Endl M., 2018, http://dx.doi.org/10.3847/1538-3881/aadca7 The Astronomical Journal, 156, 154

Jones E., Oliphant T., Peterson P., et al., 2001–, SciPy: Open source scientific tools for Python, http://www.scipy.org/

Kasting J. F., Kopparapu R., Ramirez R. M., Harman C. E., 2014, http://dx.doi.org/10.1073/pnas.1309107110 Proceedings of the National Academy of Sciences, 111, 12641

Keles E., 2021, http://dx.doi.org/10.1093/mnras/stab099 , https://ui.adsabs.harvard.edu/abs/2021MNRAS.tmp..126K

Keles E., Grenfell J. L., Godolt M., Stracke B., Rauer H., 2018, http://dx.doi.org/10.1089/ast.2016.1632 Astrobiology, http://adsabs.harvard.edu/abs/2018AsBio..18..116K 18, 116

Keles E., et al., 2019, http://dx.doi.org/10.1093/mnrasl/slz123 : Letters, 489, L37

Keles E., et al., 2020, http://dx.doi.org/10.1093/mnras/staa2435 Monthly Notices of the Royal Astronomical Society, 498, 1023–1033

Kempton E. M.-R., Perna R., Heng K., 2014, http://dx.doi.org/10.1088/0004-637x/795/1/24 The Astrophysical Journal, 795, 24

Khalafinejad S., et al., 2017, http://dx.doi.org/10.1051/0004-6361/201629473 , 598, A131

Khalafinejad S., et al., 2018, http://dx.doi.org/10.1051/0004-6361/201732029 Astronomy & Astrophysics, 618, A98

Klocová T., Czesla S., Khalafinejad S., Wolter U., Schmitt J. H. M. M., 2017, http://dx.doi.org/10.1051/0004-6361/201630068 , http://adsabs.harvard.edu/abs/2017A

Knutson H. A., et al., 2008, http://dx.doi.org/10.1088/0004-637x/690/1/822 The Astrophysical Journal, 690, 822–836

Kochanov R. V., Gordon I. E., Rothman L. S., Wcisło P., Hill C., Wilzewski J. S., 2016, http://dx.doi.org/10.1016/j.jqsrt.2016.03.005 , https://ui.adsabs.harvard.edu/abs/2016JQSRT.177...15K 177, 15

Komacek T. D., Showman A. P., 2019, http://dx.doi.org/10.3847/1538-4357/ab5b0b The Astrophysical Journal, 888, 2

Kreidberg L., 2018, http://dx.doi.org/10.1007/978-3-319-55333-7˙100 Handbook of Exoplanets, p. 2083–2105

Kurucz R. L., 1970, SAO Special Report, http://adsabs.harvard.edu/abs/1970SAOSR.309.....K 309

Lavvas P., Koskinen T., 2017, http://dx.doi.org/10.3847/1538-4357/aa88ce , https://ui.adsabs.harvard.edu/abs/2017ApJ...847...32L 847, 32

Lavvas P., Koskinen T., Yelle R. V., 2014, http://dx.doi.org/10.1088/0004-637X/796/1/15 , https://ui.adsabs.harvard.edu/abs/2014ApJ...796...15L 796, 15

Lecavelier des Etangs A., Vidal-Madjar A., Désert J.-M., Sing D., 2008, http://dx.doi.org/10.1051/0004-6361:200809704 Astronomy & Astrophysics, 485, 865–869

Lecavelier des Etangs A., et al., 2012, http://dx.doi.org/10.1051/0004-6361/201219363 , https://ui.adsabs.harvard.edu/abs/2012AA...543L...4L 543, L4

Lian Y., Showman A. P., 2010, http://dx.doi.org/10.1016/j.icarus.2009.10.006 Icarus, 207, 373–393

Lines S., et al., 2018, http://dx.doi.org/10.1051/0004-6361/201732278 , http://adsabs.harvard.edu/abs/2018A

Lithwick Y., Wu Y., 2013, http://dx.doi.org/10.1073/pnas.1308261110 Proceedings of the National Academy of Sciences, 111, 12610–12615

Lodders K., 1999, http://dx.doi.org/10.1086/307387 , http://adsabs.harvard.edu/abs/1999ApJ...519..793L 519, 793

Louden T., Wheatley P. J., 2015, http://dx.doi.org/10.1088/2041-8205/814/2/l24 , 814, L24

Macintosh B., et al., 2014, http://dx.doi.org/10.1073/pnas.1304215111 Proceedings of the National Academy of Sciences, 111, 12661

Madhusudhan N., 2012, http://dx.doi.org/10.1088/0004-637x/758/1/36 The Astrophysical Journal, 758, 36

Madhusudhan N., 2018, http://dx.doi.org/10.1007/978-3-319-55333-7˙104 Handbook of Exoplanets, p. 2153–2182

Madhusudhan N., 2019, http://dx.doi.org/10.1146/annurev-astro-081817-051846 Annual Review of Astronomy and Astrophysics, 57, 617–663

Mallonn M., Strassmeier K. G., 2016, http://dx.doi.org/10.1051/0004-6361/201527898 , http://adsabs.harvard.edu/abs/2016A

Marley M. S., Ackerman A. S., Cuzzi J. N., Kitzmann D., 2013, http://dx.doi.org/10.2458/azu˙uapress˙9780816530595-ch15 Comparative Climatology of Terrestrial Planets

Mayor M., Queloz D., 1995, http://dx.doi.org/10.1038/378355a0 , https://ui.adsabs.harvard.edu/abs/1995Natur.378..355M 378, 355

Mayor M., et al., 2003, The Messenger, https://ui.adsabs.harvard.edu/abs/2003Msngr.114...20M 114, 20

McKay C. P., 2014, http://dx.doi.org/10.1073/pnas.1304212111 Proceedings of the National Academy of Sciences, 111, 12628

McLaughlin D. B., 1924, http://dx.doi.org/10.1086/142826 , https://ui.adsabs.harvard.edu/abs/1924ApJ....60...22M 60, 22

Miller-Ricci Kempton E., Rauscher E., 2012, http://dx.doi.org/10.1088/0004-637x/751/2/117 The Astrophysical Journal, 751, 117

Mollière P., Wardenier J. P., van Boekel R., Henning T., Molaverdikhani K., Snellen I. A. G., 2019, http://dx.doi.org/10.1051/0004-6361/201935470 Astronomy & Astrophysics, 627, A67

Mollière P., et al., 2020, http://dx.doi.org/10.1051/0004-6361/202038325 Astronomy & Astrophysics, 640, A131

Montes D., et al., 2018, http://dx.doi.org/10.1093/mnras/sty1295 , https://ui.adsabs.harvard.edu/abs/2018MNRAS.479.1332M 479, 1332

Moses J. I., 2014, http://dx.doi.org/10.1098/rsta.2013.0073 Philosophical Transactions of the Royal Society A: Mathematical, Physical and Engineering Sciences, 372, 20130073

Muñoz A. G., Schneider P. C., 2019, http://dx.doi.org/10.3847/2041-8213/ab498d , 884, L43

Nikolov N., et al., 2018, http://dx.doi.org/10.1038/s41586-018-0101-7 , http://adsabs.harvard.edu/abs/2018Natur.557..526N 557, 526

Nortmann L., et al., 2018, http://dx.doi.org/10.1126/science.aat5348 Science, 362, 1388–1391

Nugroho S. K., Kawahara H., Masuda K., Hirano T., Kotani T., Tajitsu A., 2017, http://dx.doi.org/10.3847/1538-3881/aa9433 The Astronomical Journal, 154, 221

Patil A., Huard D., Fonnesbeck C., 2010, http://dx.doi.org/10.18637/jss.v035.i04 Journal of Statistical Software, Articles, 35, 1

Pepe F. A., et al., 2010, in McLean I. S., Ramsay S. K., Takami H., eds, Society of Photo-Optical Instrumentation Engineers (SPIE) Conference Series Vol. 7735, Ground-based and Airborne Instrumentation for Astronomy III. p. 77350F, http://dx.doi.org/10.1117/12.857122 doi:10.1117/12.857122

Pepper J., et al., 2007, http://dx.doi.org/10.1086/521836 , https://ui.adsabs.harvard.edu/abs/2007PASP..119..923P 119, 923

Perna R., Menou K., Rauscher E., 2010, http://dx.doi.org/10.1088/0004-637x/719/2/1421 The Astrophysical Journal, 719, 1421–1426

Pino L., et al., 2018a, http://dx.doi.org/10.1051/0004-6361/201731244 , http://adsabs.harvard.edu/abs/2018A

Pino L., et al., 2018b, http://dx.doi.org/10.1051/0004-6361/201832986 , https://ui.adsabs.harvard.edu/abs/2018AA...619A...3P 619, A3

Pino L., et al., 2020, http://dx.doi.org/10.3847/2041-8213/ab8c44 The Astrophysical Journal, 894, L27

Plez B., 2012, Turbospectrum: Code for spectral synthesis (ascl:1205.004)

Pollacco D. L., et al., 2006, http://dx.doi.org/10.1086/508556 , https://ui.adsabs.harvard.edu/abs/2006PASP..118.1407P 118, 1407

Pont F., Sing D. K., Gibson N. P., Aigrain S., Henry G., Husnoo N., 2013, http://dx.doi.org/10.1093/mnras/stt651 , http://adsabs.harvard.edu/abs/2013MNRAS.432.2917P 432, 2917

Redfield S., Endl M., Cochran W. D., Koesterke L., 2008, http://dx.doi.org/10.1086/527475 , http://adsabs.harvard.edu/abs/2008ApJ...673L..87R 673, L87

Ribas I., et al., 2018, http://dx.doi.org/10.1038/s41586-018-0677-y Nature, 563, 365–368

Ricker G. R., et al., 2015, http://dx.doi.org/10.1117/1.JATIS.1.1.014003 Journal of Astronomical Telescopes, Instruments, and Systems, https://ui.adsabs.harvard.edu/abs/2015JATIS...1a4003R 1, 014003

Ridden-Harper A. R., et al., 2016, http://dx.doi.org/10.1051/0004-6361/201628448 , https://ui.adsabs.harvard.edu/abs/2016AA...593A.129R 593, A129

Rossiter R. A., 1924, http://dx.doi.org/10.1086/142825 , https://ui.adsabs.harvard.edu/abs/1924ApJ....60...15R 60, 15

Rothman L., et al., 2010, http://dx.doi.org/https://doi.org/10.1016/j.jqsrt.2010.05.001 Journal of Quantitative Spectroscopy and Radiative Transfer, 111, 2139

Ryabchikova T., Piskunov N., Kurucz R. L., Stempels H. C., Heiter U., Pakhomov Y., Barklem P. S., 2015, http://dx.doi.org/10.1088/0031-8949/90/5/054005 , https://ui.adsabs.harvard.edu/abs/2015PhyS...90e4005R 90, 054005

Salz M., Czesla S., Schneider P. C., Schmitt J. H. M. M., 2016, http://dx.doi.org/10.1051/0004-6361/201526109 Astronomy & Astrophysics, 586, A75

Salz M., et al., 2018, http://dx.doi.org/10.1051/0004-6361/201833694 , 620, A97

Seager S., 2014, http://dx.doi.org/10.1073/pnas.1304213111 Proceedings of the National Academy of Sciences, 111, 12634

Seager S., Sasselov D. D., 2000, http://dx.doi.org/10.1086/309088 , http://adsabs.harvard.edu/abs/2000ApJ...537..916S 537, 916

Sedaghati E., et al., 2017, http://dx.doi.org/10.1038/nature23651 Nature, 549, 238–241

Seidel J. V., et al., 2019, http://dx.doi.org/10.1051/0004-6361/201834776 , https://ui.adsabs.harvard.edu/abs/2019AA...623A.166S 623, A166

Seidel J. V., Ehrenreich D., Pino L., Bourrier V., Lavie B., Allart R., Wyttenbach A., Lovis C., 2020, http://dx.doi.org/10.1051/0004-6361/201936892 , 633, A86

Showman A. P., Polvani L. M., 2011, http://dx.doi.org/10.1088/0004-637x/738/1/71 The Astrophysical Journal, 738, 71

Showman A. P., Cooper C. S., Fortney J. J., Marley M. S., 2008, http://dx.doi.org/10.1086/589325 The Astrophysical Journal, 682, 559–576

Showman A. P., Fortney J. J., Lewis N. K., Shabram M., 2012, http://dx.doi.org/10.1088/0004-637x/762/1/24 The Astrophysical Journal, 762, 24

Sing D. K., Vidal-Madjar A., Désert J.-M., Lecavelier des Etangs A., Ballester G., 2008a, http://dx.doi.org/10.1086/590075 , http://adsabs.harvard.edu/abs/2008ApJ...686..658S 686, 658

Sing D. K., Vidal-Madjar A., Lecavelier des Etangs A., Désert J.-M., Ballester G., Ehrenreich D., 2008b, http://dx.doi.org/10.1086/590076 , http://adsabs.harvard.edu/abs/2008ApJ...686..667S 686, 667

Sing D. K., et al., 2011, http://dx.doi.org/10.1051/0004-6361/201015579 , http://adsabs.harvard.edu/abs/2011A

Sing D. K., et al., 2016, http://dx.doi.org/10.1038/nature16068 , http://adsabs.harvard.edu/abs/2016Natur.529...59S 529, 59

Snellen I. A. G., Albrecht S., de Mooij E. J. W., Le Poole R. S., 2008, http://dx.doi.org/10.1051/0004-6361:200809762 , http://adsabs.harvard.edu/abs/2008A

Snellen I., de Kok R., de Mooij E., Brogi M., Nefs B., Albrecht S., 2010a, http://dx.doi.org/10.1017/s1743921311020199 Proceedings of the International Astronomical Union, 6, 208–211

Snellen I. A. G., de Kok R. J., de Mooij E. J. W., Albrecht S., 2010b, http://dx.doi.org/10.1038/nature09111 , http://adsabs.harvard.edu/abs/2010Natur.465.1049S 465, 1049

Southworth J., 2010, http://dx.doi.org/10.1111/j.1365-2966.2010.17231.x , https://ui.adsabs.harvard.edu/abs/2010MNRAS.408.1689S 408, 1689

Southworth J., 2011, http://dx.doi.org/10.1111/j.1365-2966.2011.19399.x , https://ui.adsabs.harvard.edu/abs/2011MNRAS.417.2166S 417, 2166

Spiegel D. S., Haiman Z., Gaudi B. S., 2007, http://dx.doi.org/10.1086/521921 The Astrophysical Journal, 669, 1324–1335

Steinrueck M. E., Parmentier V., Showman A. P., Lothringer J. D., Lupu R. E., 2019, http://dx.doi.org/10.3847/1538-4357/ab2598 The Astrophysical Journal, 880, 14

Strassmeier K. G., et al., 2015, http://dx.doi.org/10.1002/asna.201512172 Astronomische Nachrichten, http://adsabs.harvard.edu/abs/2015AN....336..324S 336, 324

Strassmeier K. G., Ilyin I., Steffen M., 2018a, http://dx.doi.org/10.1051/0004-6361/201731631 , http://adsabs.harvard.edu/abs/2018A

Strassmeier K. G., Ilyin I., Weber M., 2018b, http://dx.doi.org/10.1051/0004-6361/201731633 , http://adsabs.harvard.edu/abs/2018A

Thorngren D. P., Fortney J. J., 2018, http://dx.doi.org/10.3847/1538-3881/aaba13 The Astronomical Journal, 155, 214

Tsapras Y., 2018, http://dx.doi.org/10.3390/geosciences8100365 Geosciences, 8, 365

Turner J. D., et al., 2020, http://dx.doi.org/10.3847/2041-8213/ab60a9 , 888, L13

Vidal-Madjar A., Etangs A., Désert J.-M., Ballester G., Ferlet R., Hébrard G., Mayor M., 2003, http://dx.doi.org/10.1038/nature01448 Nature, 422, 143

Vidal-Madjar A., et al., 2011, http://dx.doi.org/10.1051/0004-6361/201015698 , http://adsabs.harvard.edu/abs/2011A

Welbanks L., Madhusudhan N., 2019, http://dx.doi.org/10.3847/1538-3881/ab14de , 157, 206

Welbanks L., Madhusudhan N., Allard N. F., Hubeny I., Spiegelman F., Leininger T., 2019, http://dx.doi.org/10.3847/2041-8213/ab5a89 , 887, L20

Winn J. N., 2008, http://dx.doi.org/10.1017/s174392130802629x Proceedings of the International Astronomical Union, 4, 99–109

Wong I., et al., 2020, http://dx.doi.org/10.3847/1538-3881/aba2cb The Astronomical Journal, 160, 88

Wyttenbach A., Ehrenreich D., Lovis C., Udry S., Pepe F., 2015, http://dx.doi.org/10.1051/0004-6361/201525729 , http://adsabs.harvard.edu/abs/2015A

Wyttenbach A., et al., 2017, http://dx.doi.org/10.1051/0004-6361/201630063 , https://ui.adsabs.harvard.edu/abs/2017AA...602A..36W 602, A36

Wyttenbach A., et al., 2020, http://dx.doi.org/10.1051/0004-6361/201937316 Astronomy & Astrophysics, 638, A87

Yan F., Henning T., 2018, http://dx.doi.org/10.1038/s41550-018-0503-3 Nature Astronomy, http://adsabs.harvard.edu/abs/2018NatAs...2..714Y 2, 714

Yan F., Pallé E., Fosbury R. A. E., Petr-Gotzens M. G., Henning T., 2017, http://dx.doi.org/10.1051/0004-6361/201630144 , http://adsabs.harvard.edu/abs/2017A

Yan F., et al., 2019, http://dx.doi.org/10.1051/0004-6361/201936396 , 632, A69

Yan F., et al., 2020, http://dx.doi.org/10.1051/0004-6361/202038294 Astronomy & Astrophysics, 640, L5

Zhang J., Kempton E. M.-R., Rauscher E., 2017, http://dx.doi.org/10.3847/1538-4357/aa9891 The Astrophysical Journal, 851, 84

Zhang M., et al., 2018, http://dx.doi.org/10.3847/1538-3881/aaa458 The Astronomical Journal, 155, 83

de Kok R., Brogi M., Snellen I., Birkby J., Albrecht S., de Mooij E., 2013, http://dx.doi.org/10.1051/0004-6361/201321381 Astronomy & Astrophysics, 554, A82

von Essen C., Mallonn M., Welbanks L., Madhusudhan N., Pinhas A., Bouy H., Weis Hansen P., 2019, http://dx.doi.org/10.1051/0004-6361/201833837 Astronomy & Astrophysics, 622, A71

Žák J., Kabáth P., Boffin H. M. J., Ivanov V. D., Skarka M., 2019, http://dx.doi.org/10.3847/1538-3881/ab32ec The Astronomical Journal, 158, 120

Acknowledgment

Seit meiner Kindheit habe ich mich für Leben außerhalb der Erde interessiert. Vor allem Science-Fiction weckte meine Faszination für Astronomie und Astrophysik und ließ mich Physik studieren. Nach der Master Arbeit musste ich lange warten, bis ich die Stelle gefunden hatte, die es mir erlaubt hat, weiter an Exoplaneten zu forschen. Mein größter Dank gilt Klaus Strassmeier. Er gab mir die Chance, mich mit einer eigenen Idee auf eine PhD Stellen zu bewerben und die letzten 4 Jahre meine Forschungen durchzuführen. Ohne ihn, wäre ich heute nicht vor einem Abschluss einer Arbeit, der ich mit großer Freude und Leidenschaft nachgehe. Dafür danke ich dir vom ganzen Herzen Klaus!
Es war ein heikler Weg, denn am Anfang musste ich vieles erlernen und verstehen in Bezug auf die Untersuchung von Exoplaneten mit PEPSI. Und da erschien Matthias Mallonn, der mir an meinem ersten Tag sagte: “Ich bin nicht dein Betreuer, wir sind Kollaborateure”. Er ermutigte mich selbstständig zu agieren, war mir aber immer zur Stelle, wenn ich seine fachliche Betreuung wie auch persönlichen Rat brauchte. Ich habe viel von ihm gelernt. Ohne sein Zutun wäre die Kalium-Detektion nicht möglich gewesen, denn diese Idee ist ihm zuzuschreiben. Ich danke ihm für die letzten 4 Jahre, denn nicht nur als Kollege, auch als Freund stand er mir immer zur Seite. Natürlich darf in dem Sinne auch nicht Thorsten Carroll fehlen, der für mich neben Matthias die erste Anlaufstelle in Bezug auf komplexe Diskussionen war. Er hatte immer ein offenes Ohr für mich, unterbrach immer seine Arbeit und half mir. Ich habe viel von ihm gelernt und danke ihm für die wissenschaftlichen, sozial-politischen und auch ”Gott und die Welt” Gespräche, die den Alltag aufgelockert haben. Wenn es darum geht den Alltag aufzulockern, darf eine Miss Alexoudi (alias Vada) nicht fehlen. Mit Vada gab es eine Arbeitsatmosphäre, die man jedem wünscht: Angefangen von den ersten ”Prokastinationsmeetings” bis hinzu freundschaftlichem Rat und Tat und ”turkish food vs. greek food” Gespräche, vielen dank Vada. Diese Konstellation mit Matthias, Thorsten und Vada würde ich gegen keine andere tauschen wollen, danke für die gemeinsame Zeit.
Ich danke auch Ilya Ilyin für die spannenden wissenschaftlichen Gespräche, sein Spruch ”Man read textbooks” wird mir immer erhalten bleiben. Natürlich danke ich auch allen Mitgliedern der Stellar Activity Gruppe für die gemeinsame Zeit, in der man gemeinsam beim Mittagessen, Kinoabenden oder auch beim Gruppentreffen über wissenschaftliche und Alltagsthemen debattieren konnte. In diesem Zusammenhang will ich auch Katja Poppenhäger danken, die immer eine offene Tür und Lösungsansätze für Probleme hatte. Vor allem ermöglichte sie mir, eigene Gedanken und Vorstellungen verwirklichen zu können, wofür ich ihr sehr dankbar bin. Ich danke auch meinem Zweitbetreuer Frank Spahn, der mich bei unserem ersten Treffen mit seiner Gitarre empfangen hat und bei späteren Treffen immer sehr interessiert an meiner Arbeit und meinem Wohlergehen war.
Als letztes möchte ich den allergrößten Dank meiner Frau aussprechen, denn ohne sie wäre mein Leben nicht annähernd so erfüllt. Sie hat mich immer ermutigt, meinen Ambitionen zu folgen und in der Wissenschaft zu bleiben. Sie war immer verständnisvoll, auch wenn sehr lange Arbeitstage vor der Tür standen oder auch wenn es darum ging, die wissenschaftliche Karriere nach dem PhD fortzusetzen. Vom ersten Tag an hat sie sich mit mir über jeden Fortschritt gefreut und war in den schwierigen Zeiten mit mir besorgt. Danke Lieblingsmensch, dass du immer für mich da warst. Diese Arbeit widme ich meiner Mutter, die immer schon den Wunsch hegte mich als Absolvent zu sehen.